Optimisation of light collection in inorganic scintillators for rare event searches

David Wahl
St Catherine's College, Oxford

Thesis submitted in fulfilment of the requirements for the degree of
Doctor of Philosophy at the University of Oxford

Trinity Term, 2005

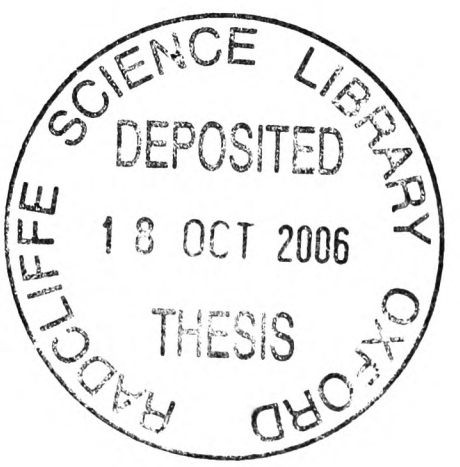

Abstract

Inorganic scintillators are playing an ever increasing role in the search for rare events. Progress in the use of cryogenic phonon-scintillation detectors (CPSD) has allowed for a rapid increase in sensitivity and resolution of experiments using this technique. It is likely that CPSD will be used in future dark matter searches with multiple scintillator materials. Further improvements in the performance of CPSD can be expected if the amount of light collected is increased. In this thesis, two approaches are used to look at ways of maximising the amount of light collected in CPSD modules. The first approach is to obtain a detailed understanding of the spectroscopic properties in the crystal to identify ways of increasing their scintillation intensity. The second is to simulate the light collection properties using a Monte-Carlo simulation program. This requires a detailed understanding of the optical properties of inorganic scintillators and obtaining this information is the focus of the current work. Two new methods have been developed to evaluate the scintillation decay time and the intrinsic light yield of scintillators. These methods are tested on CRESST $CaWO_4$ crystals so that all the input parameters necessary for the simulation of CRESST modules is available. These input parameters are used to successfully explain features of the light collection in CRESST CPSD modules and to suggest possible improvements to the design of the modules. In summary, the current work has contributed to the development of a standardised method to maximise the light yield that can be obtained from CPSD for application to rare event searches.

To my grandfathers, both physicists in their own way.

Acknowledgements

I would firstly like to thank Vitalii Mikhailik without who this thesis would not be. His counsel, availability and friendship helped in all stages of this work and for that I am deeply grateful. Duzhe dyakuyu.

I would equally like to thank Dr Hans Kraus for his guidance and help in approaching the scientific issues involved. His patience and supervision were key in ensuring that I complete this work.

Thank you to all my Oxford colleagues Sam Henry, Barnaby Tolhurst, Richard McGowan and Ujjual Divakar for their companionship over the past few years. Thanks also to Yorck Ramachers, Bela Majorovits, Cristina Cozzini and Stefan Rutzinger who have since left Oxford. Special thanks go to Yorck and Bela for the long conversations which helped to orient me at the start of my thesis.

In Munich I would like to thank Jelena Ninković for the numerous discussions on light yield measurements and the company during the first night shifts in Hasylab. I am also grateful to Klemens Rottler for his valuable insight into CRESST.

The support team in Oxford also deserve much recognition, Chris Goodwin for the long hours helping perform the transmissivity measurements, Pete Gronbech for his help on computing issues, Pete Clack for his meticulous work on polishing the many of the crystals and everyone in the mechanical workshop for their help at various stages. I would also like to thank the secretarial team and in particular Beverly Roger for putting up with my incompetence at filling out administrative forms. Though I cannot list everyone here, many more deserve thanks.

A large part of this work could not have been possible without the Litrani program. I am deeply grateful to Dr François-Xavier Gentit for having written the program and for his kind advice and help on matters relating to light transport in scintillators.

To finish the physics related acknowledgements, I would like to thank Mariya Mykhaylyk for her kindness and joyfulness during all the synchrotron luminescence measurements. I would also like express my gratitude to Dr John Cobb for the year I worked with him on the ADLER project.

My research work has been mostly supported by the Particle Physics Department and I would like to thank Prof Susan Cooper for having offered me the studentship which made my thesis possible. I would like to extend my thanks to the Leathersellers' Company for providing me with a graduate scholarship which completed the departmental funding.

Much of what I have learnt in Oxford has come from my friends. You are too many to list here but you have all brought very much to my stay here. In particular I would like to thank Tiago my partner in the perfect crime, Charles for being a great office companion, Olly who is from here and Toni for bringing Spain with him to Oxford.

I am extremely fortunate that my brother was able to come and study in Oxford and I have very much enjoyed spending these years in his company. To all my family, thank you for your patience and support. Special thanks to my father who planted the grain of physics in my brain.

The biggest thanks of all is for my mother who has been the greatest believer in my studies. From the very start to the very end she has been my main source of encouragement and inspiration and I am more grateful than I know how to express.

Finally, thank you Ursula for all your support, motivation, keeping me on track and putting up with my long working hours.

Contents

List of Figures

List of Tables

Glossary

APD Avalanche Photo-Diode

B Ratio of scattering to absorption coefficients

CCD Charged Couple Device

CCDM Collisionless Cold Dark Matter

CDMS Cryogenic Dark Matter Search

CMB Cosmic Microwave Background

CMS CERN Compact Muon Solenoid

CP Charge-Parity

CPSD Cryogenic Phonon Scintillation Detector

CRESST Cryogenic Rare Event Search with Superconducting Thermometers

DAMA The Dark Matter collaboration

DC-SPC Delayed Coincidence Single Photon Counting Technique

EDELWEISS Experience pour Détécter les WIMPS en Site Souterrain

EURECA European Underground Rare Event Search with Calorimeter Array

FWHM Full Width Half Maximum

HIS Heavy Inorganic Scintillator

keVee keV electron equivalent

LY Light Yield

LSP Lightest Supersymmetric Particle

MACHO Massive Compact Halo Object

MC Monte Carlo

MCRIM Monte Carlo Refractive Index Matching

MoLeS Mobile Luminescence End Station

MOND Modified Newtonian Dynamics

MPCC Multi-Photon Coincidence Counting

MSSM Minimal Supersymmetric Standard Model

$\mathbf{N_0}$ Intrinsic Light Yield

NBDM Non-Baryonic Dark Matter

$\mathbf{n_e}$ Extraordinary refractive index

$\mathbf{n_o}$ Ordinary refractive index

P_*min* Non-homogeneous Poisson cut variable

PMT Photo-Multiplier Tube

SCA Single Channel Analyser

SPT Superconducting Phase-Transition Thermometer

SuperLumi Synchrotron radiation facility at DESY

SQUID Superconducting Quantum Interference Device

TR Transient Recorder

UKDMC United Kingdom Dark Matter Collaboration

VUV Vacuum Ultraviolet

W Shapiro-Wilk's cut variable (when referring to MPCC technique)

WIMP Weakly Interacting Massive Particle

WMAP Wilkinson Microwave Astronomy Probe

ZEPLIN Zoned Proportional Scintillation in Liquid Noble Gases

ZIP Z(depth)-Sensitive Ionisation and Phonon Detectors

α_{att} Attenuation coefficient

α_{abs} Absorption coefficient

α_{scat} Scattering coefficient

η Light collection efficiency

$\mathbf{0\nu\beta\beta}$ Neutrinoless double beta decay

Introduction

The CRESST experiment uses cryogenic detectors to search for dark matter, elusive particles that cosmologists believe could make up the majority of matter in the universe. The favourite dark matter candidate is called the WIMP, an acronym of weakly interacting massive particle. WIMPs are predicted in most supersymmetric extensions of the standard model and hence are doubly desired by particle physicists and cosmologists. WIMPs have yet to be detected and to do this a number of dark matter experiments have upgraded their detectors and have entered the second phase of data taking. Among these experiments is CRESST, the cryogenic rare event search with superconducting thermometers. The second phase of CRESST uses $CaWO_4$ scintillating crystals as targets for WIMP interactions. The simultaneous detection of light and heat permits CRESST to distinguish between electron recoils (background, high light intensity) and nuclear recoils (signal, low light intensity). This gives a unique tool for the active rejection of background events. CRESST can also be upgraded to run with other scintillation materials, making it an ideal experiment for the confirmation of a positive WIMP signal.

WIMP interactions are by definition rare (rate is smaller than 1 event/kg/day) with a typical energy deposition expected in the range 1-100keV. To detect a direct signal, dark matter experiments need to be very sensitive and have virtually no background. To eliminate background due to cosmic rays and natural radioactivity, the CRESST experiment is located deep underground and the detectors are heavily shielded. A high energy resolution

is provided by the phonon detector whilst the light detector is used to eliminate a large part of the remaining electron-recoil background. The current discrimination threshold for nuclear and electron recoils is 12keV (electron equivalent). This limit is imposed by the energy at which the resolution on the light signal is too low to distinguish between the two types of recoils. The loss of resolution is simply due to the fact that not enough light is detected at such low energies. The discrimination threshold could therefore be lowered if more light is detected. Increasing the amount of light collected is the focus of the current work and one of the highest priorities for CRESST.

The goal of improving the light collection from crystals is also highly relevant for the future of rare events searches. The use of cryogenic phonon-scintillation detectors (CPSD) is already being considered for experiments such as EURECA, a project for the next generation of large dark matter experiments. The emphasis of the current work is on the development of a general method for the improvement of the light collection properties that can be used for all CPSD experiments. There are two ways of proceeding in order to optimise the light collection properties of a CPSD. The first consists of performing numerous experiments with combinations of crystals, reflectors, detectors and any other elements which are part of a typical setup. This method is costly, laborious and most often reveals only an incomplete picture of the light collection properties. The second option is to perform Monte-Carlo (MC) simulations of the light collection. This method is also tricky as it requires a complete understanding of all the properties of the scintillator. In view of using a range of scintillators as CPSD in the next generation of experiments, the second approach was chosen and this work presents the results of methods developed to further the accuracy of MC simulations of heavy inorganic scintillators (HIS).

The first two chapters present the dark matter problem and the CRESST experiment. The subsequent chapters go through the steps necessary to perform MC simulations of light transport in HIS. Fig. 1 shows the logical flow of the thesis and how each of the sections fit in with the general aim. The first step is to select the MC program and the

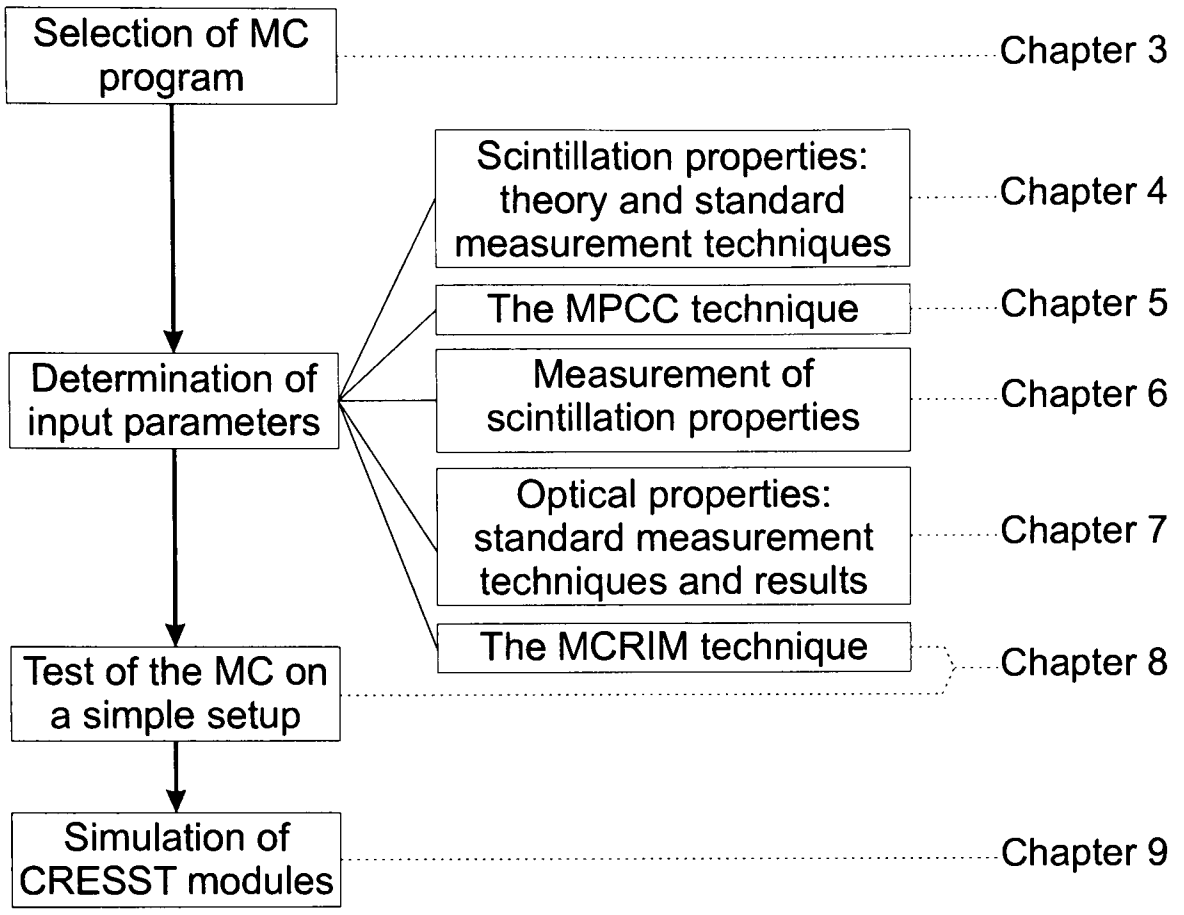

Figure 1: *Logical flow chart of the chapters of this work*

third chapter reviews the physics behind the choice of the program. The second step is to determine the input parameters, i.e. the parameters with which to construct the simulation. The determination of the input parameters was one of the main challenges of this work. The methods and results are presented in five sections, three concentrating on scintillations properties, and two on optical properties. In chapter 8, a MC-experiment combination for determining the intrinsic light yield and scattering properties of inorganic scintillators is put forward. The experiment used in this section also serves as a test of the performance of the MC. Chapter 9 is the final chapter of this thesis and presents results of various studies on the light yield of crystals in the CRESST setup.

Chapter 1

Dark matter searches

CRESST stands for Cryogenic Rare Event Search using Superconducting Thermometers. Rare events searches is a general term to describe all interactions hidden by a dominating natural background. The CRESST experiment focuses on trying to detect interactions of WIMP dark matter in cryogenic crystals. This chapter reviews the evidence for dark matter and the theories put forward to explain it. Experimental techniques that can be used for WIMP detection are presented, with particular emphasis on the direct detection of dark matter

1.1 The Dark Matter Problem

1.1.1 Cosmological evidence for dark matter

The current understanding of the universe is that at large scales it is homogeneous and isotropic. The predominant force is gravity which is best described using the framework of general relativity. The metric appropriate for the description of our universe is known as the Friedmann-Robertson-Walker (FRW) [1] metric shown in equation 1.1.

$$ds^2 = -dt^2 + R^2(t)\Big(\frac{dr^2}{(1-kr^2)} + r^2(d\theta^2 + sin^2(\theta)d\phi^2)\Big) \tag{1.1}$$

Two quantities are of particular interest in this equation, the scale factor $R(t)$ which is related to the size of the universe, and the constant k which characterises the curvature

of the universe. The FRW metric can be rescaled to ensure that the curvature constant k has integer values -1, 0 or 1; k=-1 is an open universe, k=1 is a closed universe and k=0 is a flat universe. The shape and expansion rate of the universe are related by the Hubble equation:

$$\frac{k}{R^2} = H(\Omega_{tot} - 1) \tag{1.2}$$

H is known as the Hubble constant and is a measure of the rate of expansion of the universe. H_0, which is the notation for H measured at the present day, is shown in equation (1.3) and has been calculated by measuring the red-shift of distant objects in the universe (h=0.65±0.15 [2]).

$$H_0 = h \times 100 kms^{-1}Mpc^{-1} \tag{1.3}$$

In equation (1.2), Ω_{tot} is the cosmological density parameter and is defined as the ratio of the density of the universe (ρ) to the critical density ρ_c:

$$\Omega_{tot} = \frac{\rho}{\rho_c} \tag{1.4}$$

$$\rho_c = \frac{3H_0^2}{8\pi G_N} \tag{1.5}$$

where G_N is Newton's gravitational constant. Recent measurements of Ω_{tot} provide us with the clearest indication of the existence of dark matter to date.

1.1.2 Measuring the cosmological density parameter

The Wilkinson Microwave Astronomy Probe (WMAP) is an 840kg satellite designed to measure the cosmic microwave background (CMB) of the universe [3]. In 2003, the WMAP collaboration published results which show that the universe is flat (k=0) and that therefore Ω_{tot} is very close to unity. The WMAP results also place limits on the composition

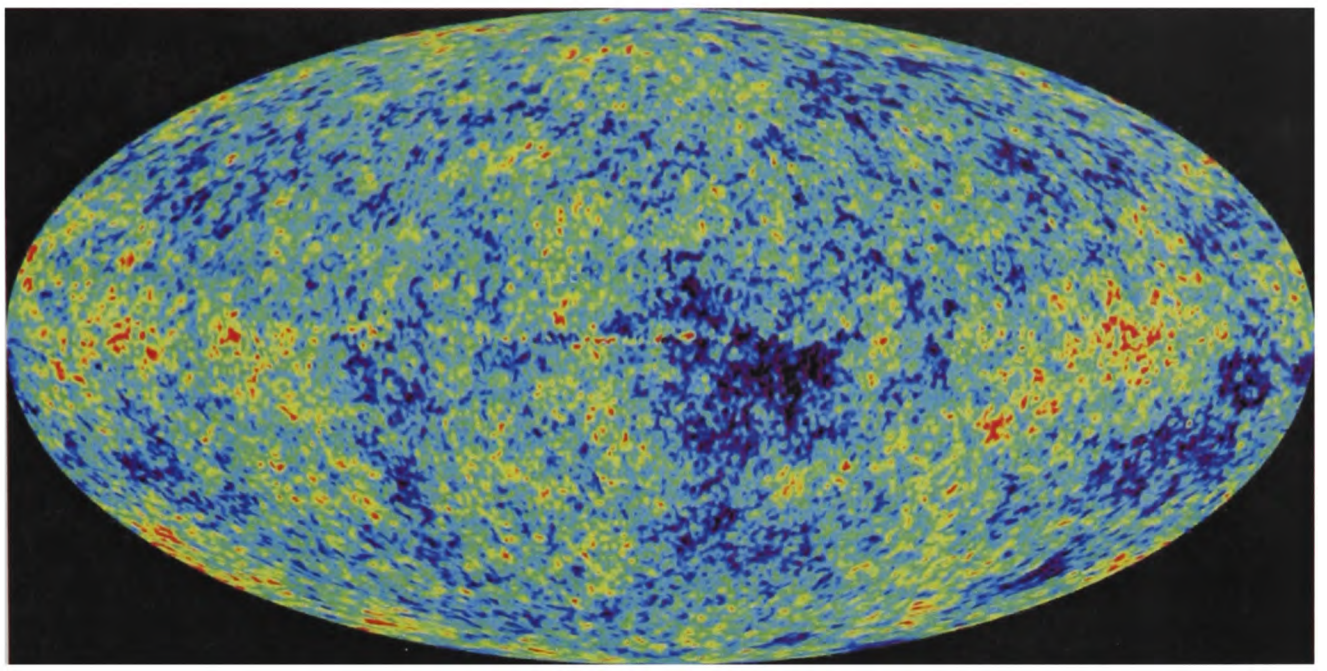

Figure 1.1: *CMB map of the universe. Analysis of maps like this one were used to demonstrate the "flat" nature of the universe [3].*

of matter which makes up the universe.

$$\Omega_{tot} = \Omega_\Lambda + \Omega_B + \Omega_{NBDM} \tag{1.6}$$

Ω_Λ is the cosmological density parameter corresponding to dark energy, a quantity predicted to exist by the Einstein equations of general relativity. The WMAP collaboration estimate that Ω_Λ=0.73±0.04. Ω_B is the proportion of Ω_{tot} which can be attributed to baryonic matter (matter which interacts via the strong force). The measured value for Ω_B is 0.044±0.004. The last element of equation (1.6) is the density of non-baryonic dark matter (NBDM), and was measured by the WMAP collaboration as $\Omega_{NBDM} = 0.23 \pm 0.04$.

Cosmology distinguishes two forms of NBDM, referred to as hot and cold dark matter. Cold dark matter (CDM) particles must have been non-relativistic at the time when enough matter was present within the universe to form a galaxy. The cutoff between the two forms can be broadly defined in terms of a minimum mass for CDM, $M_{CDM} \gtrsim$ 1 keV [1]. Results from observations of large scale structures indicate that the NBDM

content of the universe must be mostly made up of CDM [4]. A further narrowing of the properties of the dark matter has been obtained from simulations of the formation of structures in the universe. The majority of simulations require that the CDM be collisionless in order to agree with observations [5]. Collisionless means that the cross-section for interactions between CDM particles, or CDM and baryonic matter must be small enough to be negligible at the present temperature of the universe. As a consequence of this, the main interactions of collisionless cold dark matter (CCDM) are gravitational, and CCDM particles are thought to become gravitationally bound to large structures to form a sort of halo.

1.1.3 Galactic rotation curves

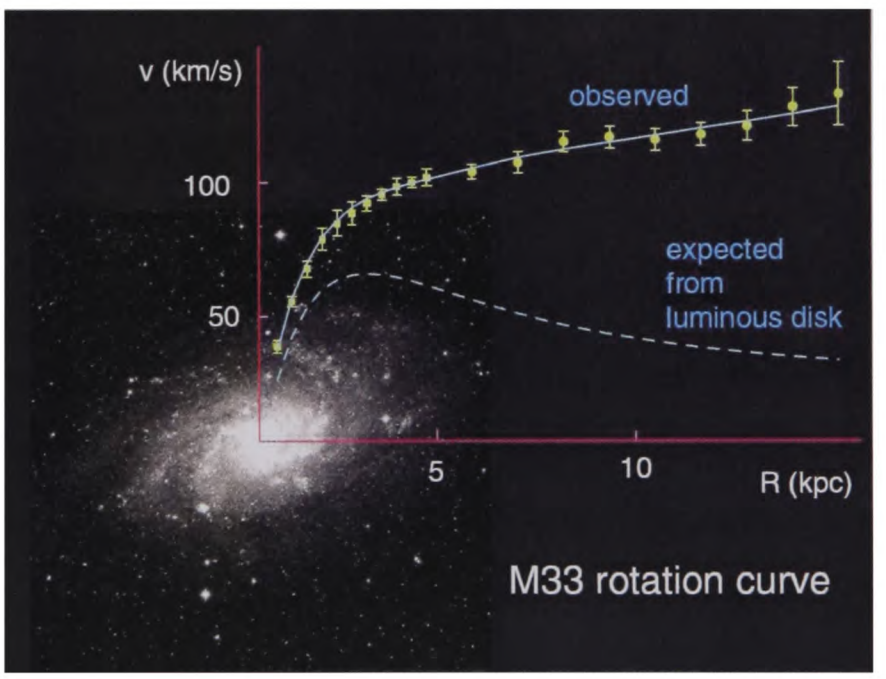

Figure 1.2: *Rotation curve of the galaxy M33 taken from [2]. At large R, the velocity of rotation is higher than would be expected from the distribution of luminous matter.*

Cosmology is just one of the clues which points to the existence of dark matter. The oldest and most straightforward evidence comes from the rotation curves of galaxies [6]. Using Newton's laws, the rotational velocity of an object at distance R from the centre

of rotation of a galaxy is given by:

$$v_{\perp}^2 = \frac{G_N M(R)}{R} \tag{1.7}$$

where M(R) is the mass of the galaxy contained within radius R. If galaxies are only constituted of luminous matter, M(R) can be obtained by looking at the distribution of stars. Fig. 1.2 shows the measured rotation curve for galaxy M33, as well as the rotation curve that would have been expected from observations of its luminous matter. It shows that the rotational velocity continues to increase with radius past the luminous matter "edge", indicating the presence of a halo of matter extending way beyond the luminous sphere. The same feature has been observed for a large number of galaxies using radiation from radio waves to visible light [7]. A simple explanation for this apparent paradox would be to have the galaxy embedded in a vast halo of dark matter [8] which fits in very nicely with the CCDM model from cosmology. Though the combination of evidence makes the existence of dark matter seem certain, there are so far few clues as to what exactly this dark matter could be.

1.2 Dark matter candidates

1.2.1 Dark matter which is not CCDM

Massive compact halo objects

Massive compact halo objects (MACHOs) is a general term to refer to any compact object with a significant mass. They include baryonic dark matter such as planets, brown dwarfs, neutron stars and black holes which will contribute to the dark matter mass of galaxies. The designation of MACHO also includes possible compact objects made from NBDM. A common technique for the detection of MACHOs is by observing gravitational lensing effects. The MACHO project which monitors stars in the Large Magellanic Cloud

has calculated that approximately 20% of the mass of the galactic halo is constituted of MACHOs [9] and that therefore MACHOs cannot be the only source of dark matter.

Axions

Candidates that can also be used to solve other physics problems are naturally favoured solutions to the dark matter problem. One such candidate is the axion, which was introduced as a hypothetical particle to solve the strong CP (charge-parity) problem. Experiments measuring the electric dipole moment of neutrons have shown that the strong force conserves CP symmetry to a very high degree of accuracy, even though the standard model predicts second order CP violating terms in the Lagrangian [10]. The axion was postulated to cancel the effect of the CP violating term in the quantum chromo-dynamics (QCD) Lagrangian [11]. There are no theoretical limits on the axion mass, though experimental searches and astrophysics constraints place a limit of $m_A < 0.02$ eV [12]. If the number of axions is very large, they could represent a significant contribution to the density of NBDM. Searches for axions aim to detect the conversion of axions to microwave photons when the former pass through a magnetic field [13].

Modified Newton Dynamics

Instead of looking for new particles to explain the dark matter density, a solution was proposed which questions the physics laws which lead to the conclusion that dark matter exists. A theory called modified Newton dynamics (MOND) suggests that Newton's laws of gravity need to be slightly modified on a galactic scale [14]. The idea is that the classical gravitational force is different for very small accelerations. MOND calculations are reasonably successful in explaining observed rotation curves [15], however they fail to explain galaxy clusters and other large scale effects.

Neutrinos

Recent results from neutrino oscillation experiments have shown that there is exists a hierarchy in neutrino masses, implying a non-zero neutrino mass [16, 17]. One of the parameters that was extracted from these measurements is that the density parameter from neutrinos is $\Omega_\nu \approx 0.001$, meaning that the contributions from neutrinos is negligible on a cosmological scale [18].

1.2.2 CCDM and Weakly Interacting Massive Particles

In the early universe, all particles were in thermal equilibrium, including weakly interacting massive particles (WIMPs). As the universe expanded and cooled, the interactions between particles were no longer energetic enough to repopulate massive particles which decayed through other processes. Massive unstable particles gradually disappeared in favour of lighter ones. If WIMPs are a stable massive particle, the universe could contain a relic massive particle population. WIMPs are by definition CCDM particles. As they only interact via the weak force and gravity, they are non-baryonic. Their weak interaction makes them collisionless, and their high mass makes them cold, meaning they can form halos of matter around the large scale structure of the universe. The "standard" WIMP halo model is an isothermal cloud of particles with no net angular momentum. The velocity distribution of the particles inside the cloud is give by a Maxwellian distribution:

$$f(v) = \frac{4v^2}{\bar{v}^3\sqrt{\pi}} exp(\frac{-v^2}{\bar{v}^2}) \tag{1.8}$$

where $\bar{v}$ is the velocity dispersion and is related to the asymptotic flat rotation velocity by $v_\infty = \sqrt{2/3}\bar{v}$ [19]. The distribution is cut off at $\sim$600 km s^{-1} which corresponds to the escape velocity of the WIMPs from the galactic gravitational field. Models of the

distribution of WIMPs provide an estimate for their density contribution:

$$\Omega_\chi h^2 = \frac{3 \times 10^{-27} cm^3 s^{-1}}{< \sigma_A \bar{v} >} \tag{1.9}$$

where σ_A is the cross section for annihilation. If σ_A is typical of weak force interactions, Ω_χ will be of the order of 1, a fairly good match to the amount of dark matter thought to be present in the universe! A stable massive weakly interacting relic of the early universe could therefore solve the dark matter problem. Further models predict the local density ρ_0 of dark matter in the galaxy. The predicted value of ρ_0 depends on the WIMP model used and is usually cited as ρ_0=0.3 GeV cm^{-3} [20].

Supersymmetric WIMP candidates

A prime WIMP candidate comes from the minimum supersymmetric extension of the standard model (MSSM). Supersymmetry was introduced to explain the "hierarchy problem", i.e. the large difference observed between the W boson mass and the Planck mass. It predicts that every known particle will have a supersymmetric equivalent with spin difference $\frac{1}{2}$, i.e. every fermion has a supersymmetric partner boson and vice-versa. In the MSSM, supersymmetric and standard model particles are distinguished by the R-parity quantum number. The R parity of a particle is given by:

$$R = (-1)^{3(B-L)+2S} \tag{1.10}$$

where B is the baryon number, L is the lepton number and S is the spin. Standard model particles have parity of R=+1 whilst supersymmetric particles have R=-1. If R-parity is a conserved symmetry, there will be a stable supersymmetric particle called the lightest supersymmetric particle (LSP). In the MSSM, this particle is the neutralino (χ), which is a linear combination of the supersymmetric partners of the Higgs, the Z^0 and the photon. The neutralino has no electric charge and no colour. Theoretical calculations and results

from the LEP (CERN Large Electron Positron Collider) place the mass of the MSSM WIMP roughly in the range 50-500GeV [21].

Calculating the WIMP interaction rate

In the non-relativistic limit for CDM, there are two possible types of WIMP-nucleon interactions, spin-dependent (axial) and spin-independent (scalar) interactions. This means that the total cross section for WIMP-nucleus interactions is composed of two parts:

$$\sigma_0 = \sigma_{axial} + \sigma_{scalar} \tag{1.11}$$

An expression for the cross section of spin dependent and independent interactions is given in equation (1.13).

$$\sigma_{scalar} \propto \mu^2 A^2 \tag{1.12}$$

$$\sigma_{axial} \propto \mu^2 \lambda^2 J(J+1) \tag{1.13}$$

where $\lambda^2 J(J+1)$ is related to the spin of the nucleus and μ is the reduced mass of the WIMP-nucleus system:

$$\mu = \frac{m_\chi m_N}{m_\chi + m_N} \tag{1.14}$$

It can be shown that for heavy nuclei (A>30), the spin independent term dominates the cross section [19]. In the simplest model, the scalar cross-section scales as A^2 which explains why elements with high atomic mass such as tungsten are used in the search for dark matter. For the spin dependent interactions ^{7}Li and ^{19}F are expected to have a high interaction cross section as they have a high value of $\lambda^2 J(J+1)$ [22]. For interactions with a high momentum transfer (q), the de Broglie wavelength becomes comparable to the typical size of the nucleus and the cross-section must be corrected for the substructure

of the nucleus using a form factor.

$$\sigma_0(q) = \sigma_0 F^2(q) \tag{1.15}$$

The form factor is given by the Fourier transform of the distribution of nucleons inside the nucleus [19]. Given the cross section, it is possible to calculate the expected rate of energy deposition on each nucleus. The recoil energy of a nucleus of mass m_N due to a collision with a WIMP of mass m_χ can be calculated using classical mechanics:

$$E_r = \frac{4E_\chi \mu^2}{m_N m_\chi}\frac{1}{2}(1 - cos\theta) \tag{1.16}$$

where θ is the scattering angle and $E_\chi = \frac{1}{2}m_\chi v_\chi^2$ is the kinetic energy of the incoming WIMP. Combining equation (1.16) and the WIMP velocity distribution leads to a prediction of the differential recoil energy (E_r) spectrum expected from WIMP-nucleus interactions:

$$\frac{dR}{dE_r} = \frac{\rho_0 \sigma_0}{2m_N \mu^2} F^2(E_r) \int_{v_{min}}^{v_{max}} \frac{f(v)}{v} dv \tag{1.17}$$

$$v_{min} = \sqrt{\frac{E_r m_N}{2\mu^2}} \tag{1.18}$$

The function $f(v)$ is the distribution of WIMP velocities in the rest frame of the detector. The upper limit v_{max} is the escape velocity of WIMPs from the galactic gravitational field. By integrating over the recoil energies, one obtains the expected recoil rate in the detector:

$$R = \frac{\rho_0 \sigma_0}{2m_N m_\chi}\frac{2}{\sqrt{\pi}} v_0 exp(-\frac{E_{th} m_N}{2\mu^2 v_0^2}) \tag{1.19}$$

where E_{th} is the detection threshold of the experiment and v_0 $\approx$220km s^{-1} is the local rotational velocity around the galactic centre. The total rate of interactions in a detector containing N_{det} atoms is given by the sum of the rates from the individual atoms as shown

in equation (1.20).

$$\frac{dR_{det}}{dE_r} = N_{det} \sum_i f_i R_i \tag{1.20}$$

where f_i is the fraction of N_{det} that is composed from nuclei i. Equation (1.19) contains two quantities which depend on the experimental conditions and determine the WIMP detection rate. E_{th}, which needs to be as low as possible and σ_0, which was shown to depend on the choice of materials (nuclei) that make up the detector. Equation (1.19) forms the basis of how the recoil spectra obtained from the direct detection experiments are used to place limits on m_χ and σ_0. The WIMP velocity distribution, the form factor and the WIMP density are all parameters which need careful consideration to derive accurate limits [23].

1.3 WIMP detection experiments

Given the wealth of solutions that have been proposed to the dark matter problem, and the possibility of revealing the first supersymmetric particles, it is no surprise that WIMP detection is of high interest to the particle physics community. The following section provides a short review of some of the detection techniques used in the search for dark matter. Two approaches are discussed, the direct approach which looks to measure the signal of a WIMP collision in a bolometer, and the indirect approach which aims to detect the particles produced from the annihilation of two WIMPs.

1.3.1 Indirect WIMP detection

When two WIMPs collide, they can annihilate to from a particle-antiparticle pair, for example high energy neutrinos or photons. Indirect WIMP searches look for highly energetic particles coming from the centre of dense objects such as the sun. It is thought that

WIMPs may become gravitationally bound to these objects which will accumulate a high density of dark matter. By "pointing" high energy particle telescopes in the direction of the dense objects, one could detect a WIMP annihilation signal. Telescopes that may be able to detect such dark matter annihilations include large neutrino telescopes such as AMANDA, ANTARES and ICECUBE [24]. Another promising alternative is the use of satellite detectors such as GLAST [25].

1.3.2 Annual Modulation and DAMA

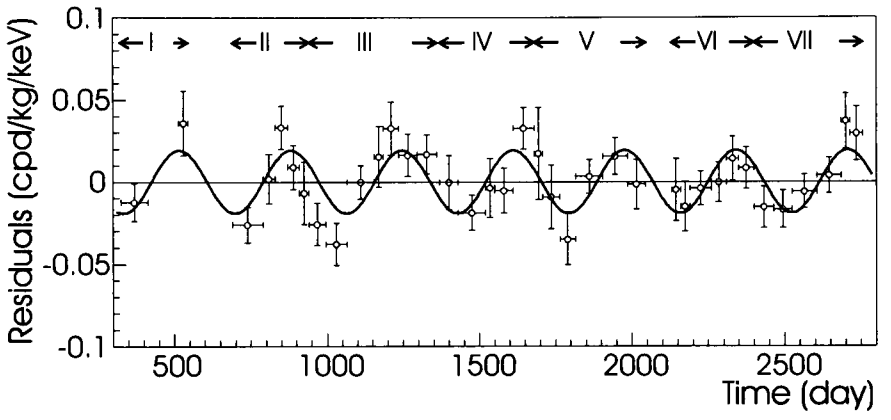

Figure 1.3: *The DAMA annual modulation signal for recoils in the range 2-6keV [26]*

The main method for the direct detection of WIMPs is to try and eliminate all other interactions and be left with a pure WIMP recoil spectrum. An alternative method is to look for annual modulation signals associated with the movement of the earth relative to the WIMP wind. The motion of the earth through the WIMP halo is a sum of the rotational velocity of the galaxy, the motion of the sun and the velocity of the earth around the sun [27]. Equation 1.21 shows the velocity of the earth as calculated from observations of our position in the galaxy.

$$v_E = (232 + 15sin(2\pi y))kms^{-1} \tag{1.21}$$

where y is the fraction of the year that has passed since the 2^{nd} of March. As shown in section 1.2.2, the detection rate depends on the average velocity of WIMPs with respect

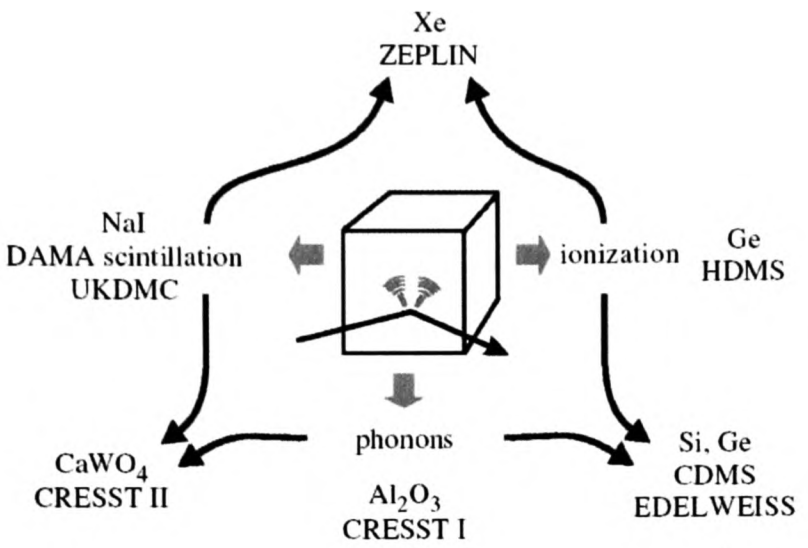

Figure 1.4: *Pictograph of the different techniques used in dark matter searches. (Taken from [28])*

to the detector. The detection rate of a dark matter experiment should therefore vary with the direction of travel of the earth relative to the WIMP halo. Annual modulation is considered as one of the signatures of dark matter. In 2003, the DAMA collaboration reported a positive WIMP signal based on the detection of an annual modulation in their signal [26] shown in Fig. 1.3. They operated 100kg of NaI(Tl) scintillators for 7 years in the Gran Sasso underground laboratory in Italy and base their positive report on the annual modulation signal. As we will see in the next section, other direct detection experiments have obtained results which conflict with the DAMA claim.

1.3.3 Direct Detection Experiments

Fig. 1.4 shows some of the different techniques used by direct detection experiments. The experiments which are setting the most competitive limits often use a combination of two detection techniques to enable discrimination between signal and background. Currently the best limits are being set by the CDMS group that use Z(depth)-sensitive ionisation and phonon detectors (ZIP) [29]. The CDMS measure a normalised ionisation to phonon energy yield of 0.3 for nuclear recoils (signal) compared to 1 for electron recoils (background). This allows them to reject a significant portion of the background by the active

discrimination of events. Another group using the cryogenic ionisation-phonon technique is the EDELWEISS group who operate in the Frejus tunnel [30]. The ZEPLIN I detectors operated by the UK dark matter collaboration (UKDMC) measure the scintillation light from interactions in liquid xenon [31] and are able to estimate the number of nuclear recoils by statistical analysis of scintillation time constants. The ZEPLIN II/III detectors will be able to actively reject electron recoil background using a combination of scintillation signals from liquid and gaseous xenon [32]. Particle interactions in the liquid xenon produce scintillation light and ionisation electrons which transfer to the gaseous xenon. The electrons in the gas are submitted to an electric field which causes electroluminescence. Nuclear and electron recoils produce a different relative intensity of scintillation in the liquid and gaseous phases allowing the rejection of background interactions [33]. The CRESST experiment will be described in detail in the following chapter.

1.3.4 Summary

Fig. 1.5 shows the exclusion limits published by some of the leading direct dark matter experiments. Apart from the DAMA results which seem incompatible with the other experiments, WIMP searches (and general dark matter) have yet to produce a positive signal. That means that bigger and better detectors will have to be constructed in the future to look for dark matter. The current exclusion limits are just starting to cut into the phase space of WIMPs predicted by the various supersymmetric theories such as those proposed by Bottino et al [35]. It is an exciting time to be in dark matter research and the development and improvement of detection techniques could soon lead to the first identification of a positive WIMP signal.

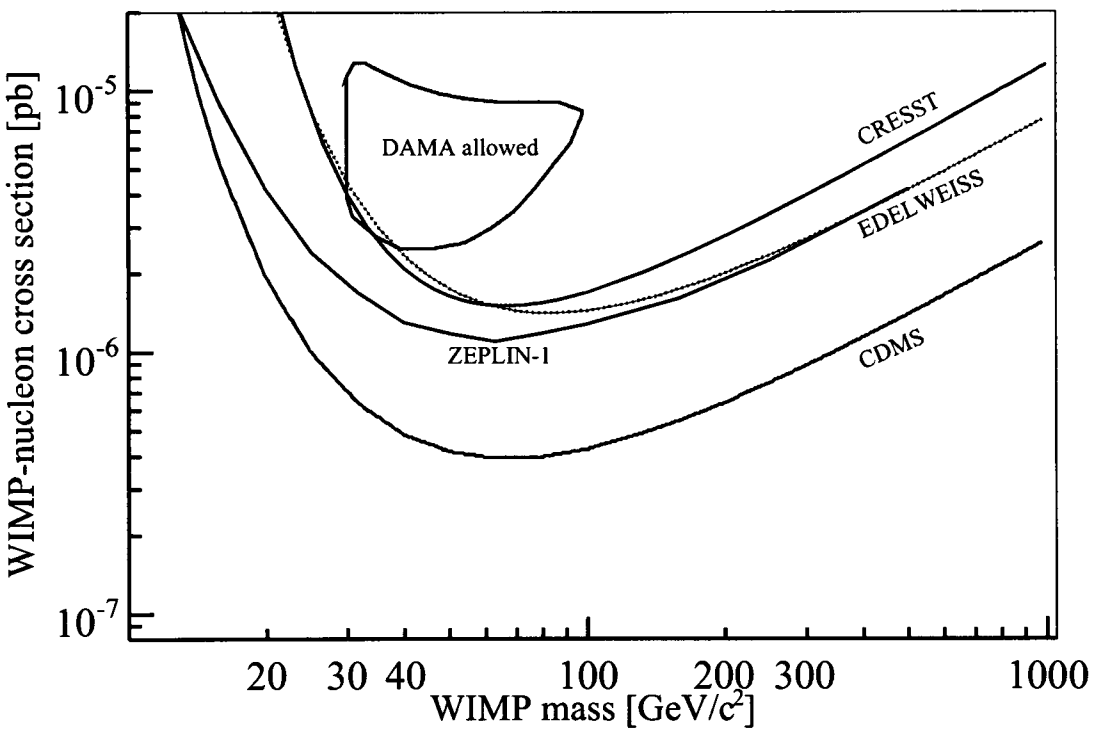

Figure 1.5: *Current limits from some of the principle direct detection experiments: DAMA [26], CRESST II [34], CDMS [29], Edelweiss I [30], ZEPLIN I [31]*

Chapter 2

Cryogenic phonon-scintillation detectors and CRESST

A promising technique for the search of dark matter is the use of cryogenic phonon-scintillation detectors (CPSD). This technique was pioneered by CRESST and has led to competitive exclusion limits on WIMP cross-sections. The detection of phonon signals at millikelvin temperatures provides the main tool for the sensitivity of the CRESST detectors. The scintillation signal from the target crystals allows for the active rejection of background events by comparing the ratio of light to phonon signals. This section presents the details of the CRESST experiment as well as the principles of the CPSD technique. Special emphasis is placed on the future of CPSD based searches which are expected to make use of a range of materials including $CaWO_4$ and $ZnWO_4$.

2.1 Cryogenic phonon-scintillation detectors

2.1.1 Low temperature calorimeters

During the 1980's, new radiation detectors that combine a high detection efficiency with a high resolution were developed. Millikelvin calorimeters were proposed to exploit low temperature properties such as superconduction and the very low specific heat of materials at cryogenic temperatures. Fig. 2.1 shows a simple diagram of a cryogenic calorimeter.

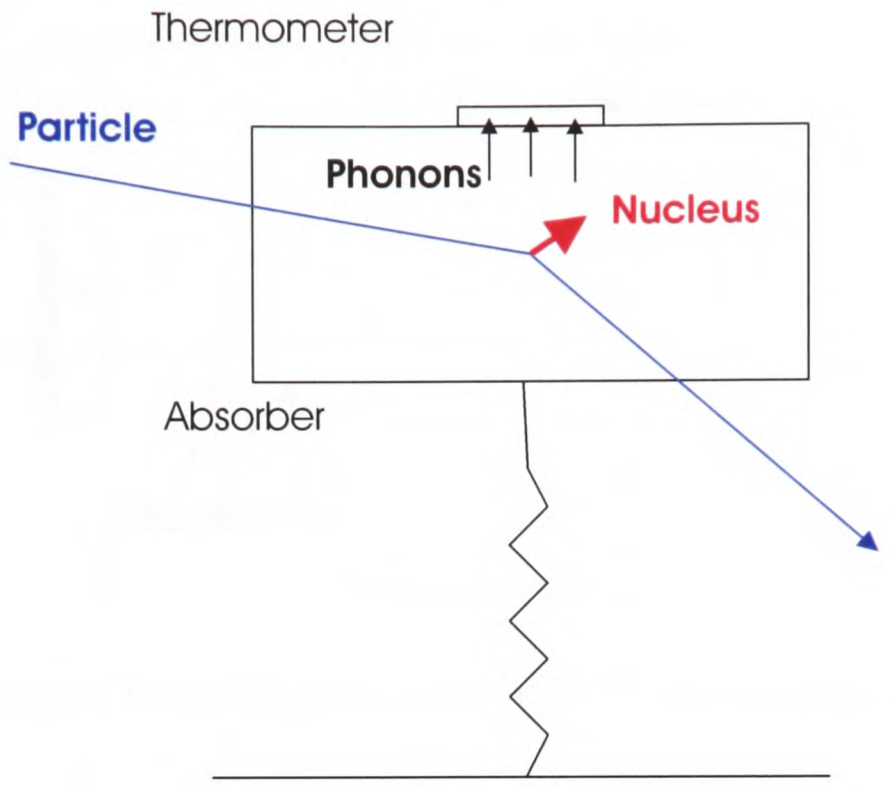

Figure 2.1: *Diagram of a simplified cryogenic calorimeter from [36]*

The absorber crystal is placed in a surrounding heat sink which cools the crystal. The thermometer film is grown directly on the absorber so that they are in thermal contact. When a particle deposits energy in the absorber (E_{dep}), it causes a rise of temperature of the absorber (and therefore the thermometer) which is determined by its heat capacity (C) [37].

$$\Delta T = \frac{E_{dep}}{C} exp(\frac{-t}{\tau_a}) \tag{2.1}$$

Equation (2.1) shows the importance of reducing the heat capacity in order to maximise the increase of temperature in the absorber and thermometer. Since C scales as T^3, the best way to have a low heat capacity is by operating the detector at very low temperatures. Another reason for operating the detector in the millikelvin range is the possibility to exploit the superconducting properties of the thermometer film. In the region of the critical temperature (T_c) of a superconductor, a small rise in temperature ΔT causes a large rise in the resistance ΔR as shown in Fig. 2.2 [38]. The thermometer is operated as part of a readout circuit for which any changes in resistance are measured by a supercon-

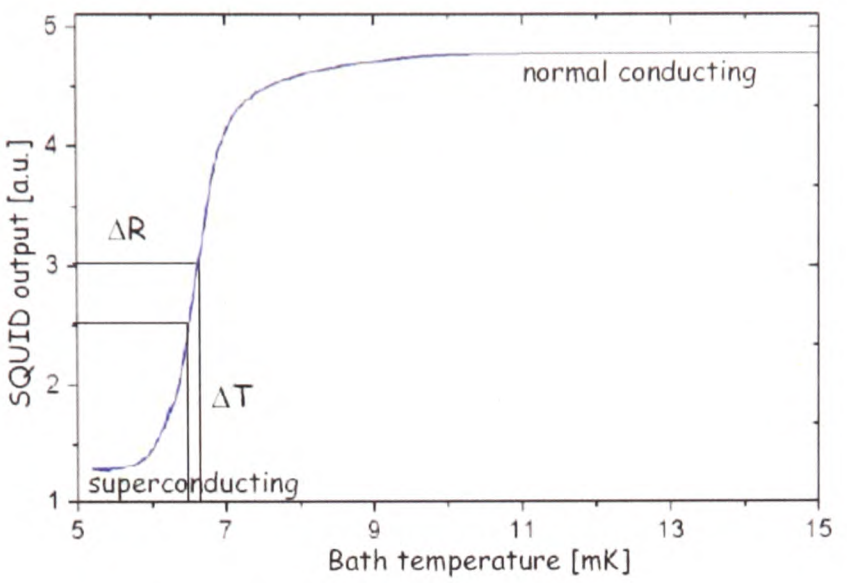

Figure 2.2: *Measured transition curve for a CRESST superconducting thermometer*

ducting quantum interference device, or SQUID [36].

The cryogenic calorimetric technique can be used for many different absorber materials, as long as it has a low heat capacity and good phonon properties. The first phase of CRESST used Al_2O_3 crystals with a mass of 262g. A tungsten film with a superconducting transition at around 15mK was deposited on each crystal. CRESST I set competitive limits on the cross-section of WIMP-nucleus interactions, especially for low mass WIMPs [39]. In order to further improve the performance of the detector, the purely calorimetric approach was abandoned in favour of a hybrid scintillation-phonon detector concept.

2.1.2 Cryogenic phonon-scintillation detectors

Cryogenic phonon-scintillation detectors (CPSD) exploit the difference in scintillation intensity between signal (nuclear recoils) and background (electron recoils) events. Scintillators have a higher light yield/MeV for β and γ interactions (which cause electron recoils) than for WIMPs (which cause nuclear recoils). The key to having a good CPSD detector lies in the choice of the scintillator crystal. The crystals are fully enclosed in

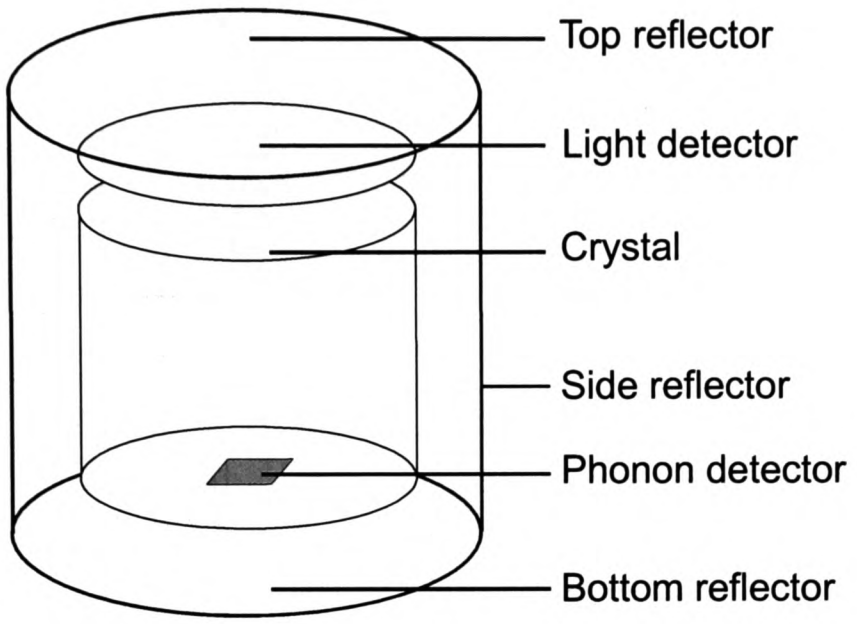

Figure 2.3: *Schematic diagram of a CPSD module.*

reflecting foil which is not in contact with the crystal faces. A schematic diagram of a CRESST CPSD module is shown in Fig. 2.3. The detection of phonons provides a high sensitivity and resolution whilst the light channel allows the active rejection of background events. Fig. 2.4 shows a scatter plot of the signal amplitude measured in the light and phonon channels for each event. Two bands are formed, one for nuclear recoils and one for electron recoils. For E_{dep} <12keVee, the two bands can no longer be resolved [40] as the low intensity detected in the light channel results in a statistical degradation of the signal. Maximising the amount of light detected is therefore essential to lower the discrimination threshold of the CPSD. The optimisation of the light properties of CPSD modules is the main focus of this work and can be divided into two approaches. The first is to optimise the scintillation yield of the crystals by understanding their spectroscopic properties and the effects of growth processes on the intensity of luminescence (chapters 4, 5 and 6). The second is to optimise the light collection properties via MC (chapters 7, 8 and 9).

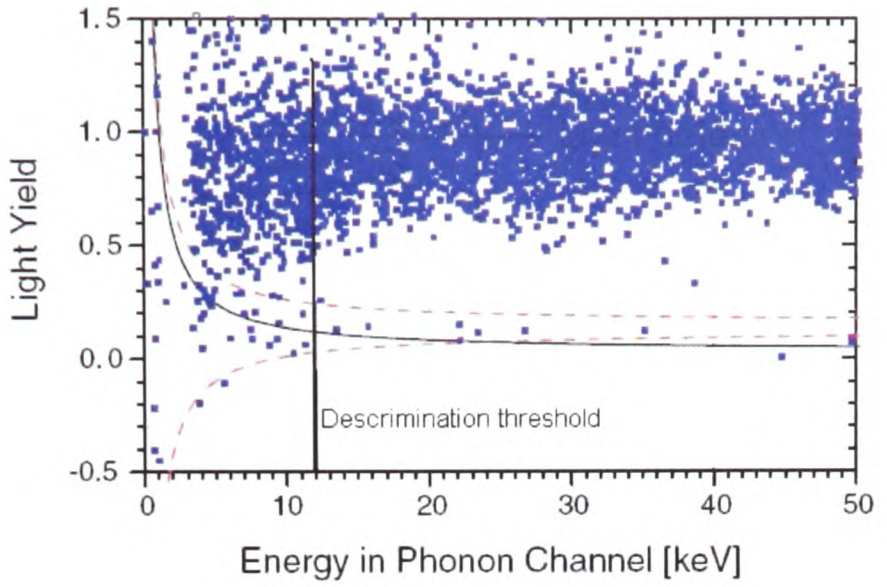

Figure 2.4: *Light yield (measured relative to phonon signal) versus deposited energy in the phonon channel in a CRESST detector. The dashed lines show the neutron recoil band. The discrimination threshold is defined as the phonon channel energy below which the neutron recoil band is indistinguishable from electron recoils (higher band) at 12keV electron equivalent (keVee) [40]*

2.2 The CRESST experiment

The CRESST detector is located deep underground at the Gran Sasso laboratory in Italy under 3700m.w.e. (meters water equivalent) of rock. This reduces the muon flux to $\sim$ 1 m^{-2} h^{-1}, approximately 10^6 times lower than at the earth's surface. The main source of background comes from the natural radioactivity in the surrounding rock and can be divided into two categories, gamma background and neutron background. The integral flux of γ background, calculated by taking into account the relative abundance of isotopes in the Gran Sasso rock is approximately 1 cm^{-2} s^{-1} [41]. Estimates and measurements yield a neutron flux of about $10^{-6}cm^{-2}s^{-1}$ [42]. The background activity requires that the CRESST detectors be heavily shielded. Fig. 2.5 shows the CRESST dilution refrigerator and the position CPSD inside the setup. The refrigerator is enclosed in a Faraday cage hut and has been upgraded to include neutron shielding and muon vetoes to further reduce the background. The upgraded experiment is due to start taking data in the near future and will host up to 10kg of $CaWO_4$ corresponding to 33 $CaWO_4$ crystals of mass $\sim$300g and dimensions $\oslash$4.0cmx4.0cm. The crystals each form part of a CPSD

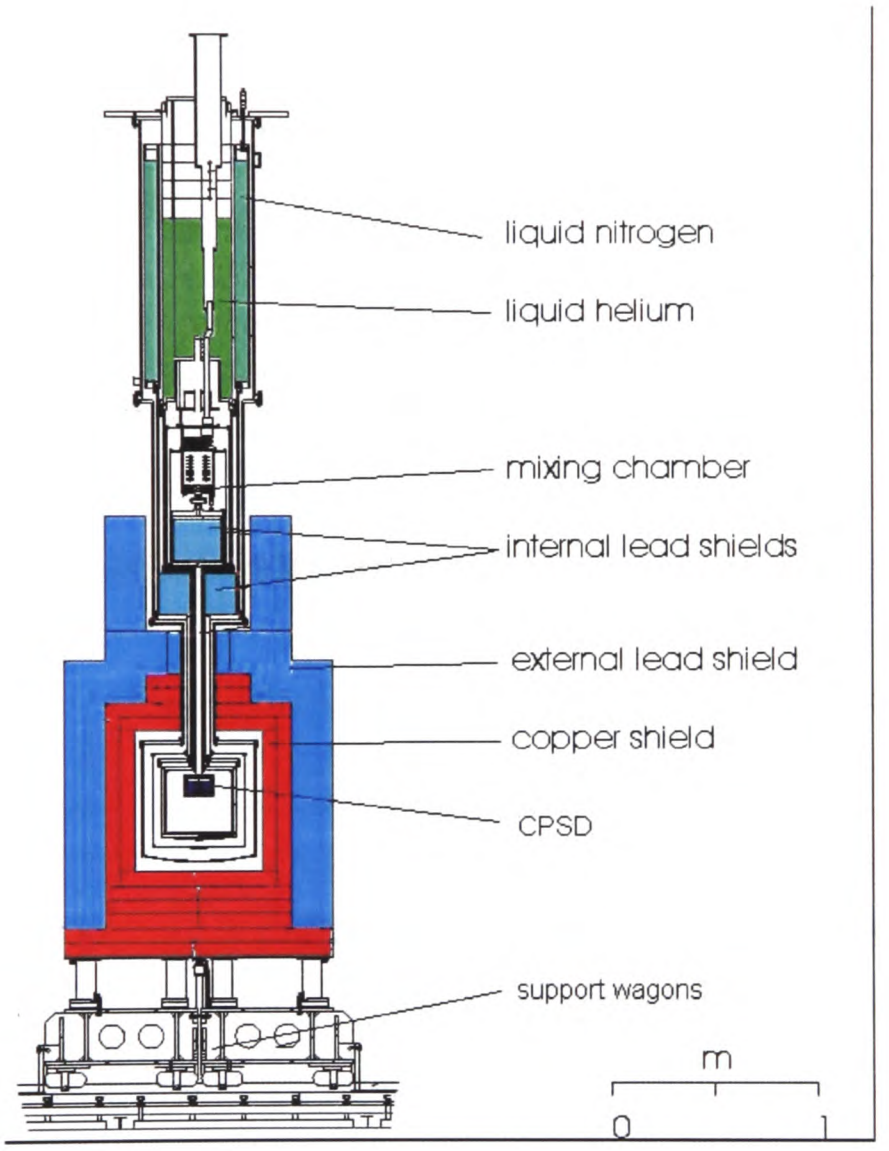

Figure 2.5: *Schematics diagram of the CRESST experiment.*

module, i.e. they are enclosed in a reflective foil and have a light and phonon detector. A tungsten superconducting phase transition (SPT) thermometer film is deposited on one of the flat surfaces of each crystal to act as the phonon absorber. The light detector is placed approximately 5mm from the face opposite to the phonon detector. The light detector is a silicon absorber on which a phonon detector has been deposited, and the readout electronics were tuned to match the decay time of $CaWO_4$ [43]. The silicon absorbs incident light that has escaped the crystal, converting it into phonons which are then read out by the SPT. The CRESST collaboration has already published some very good limits using two $CaWO_4$ crystals [34].

2.3 The future of dark matter and CPSD detectors

2.3.1 Projected sensitivity of CRESST phase II

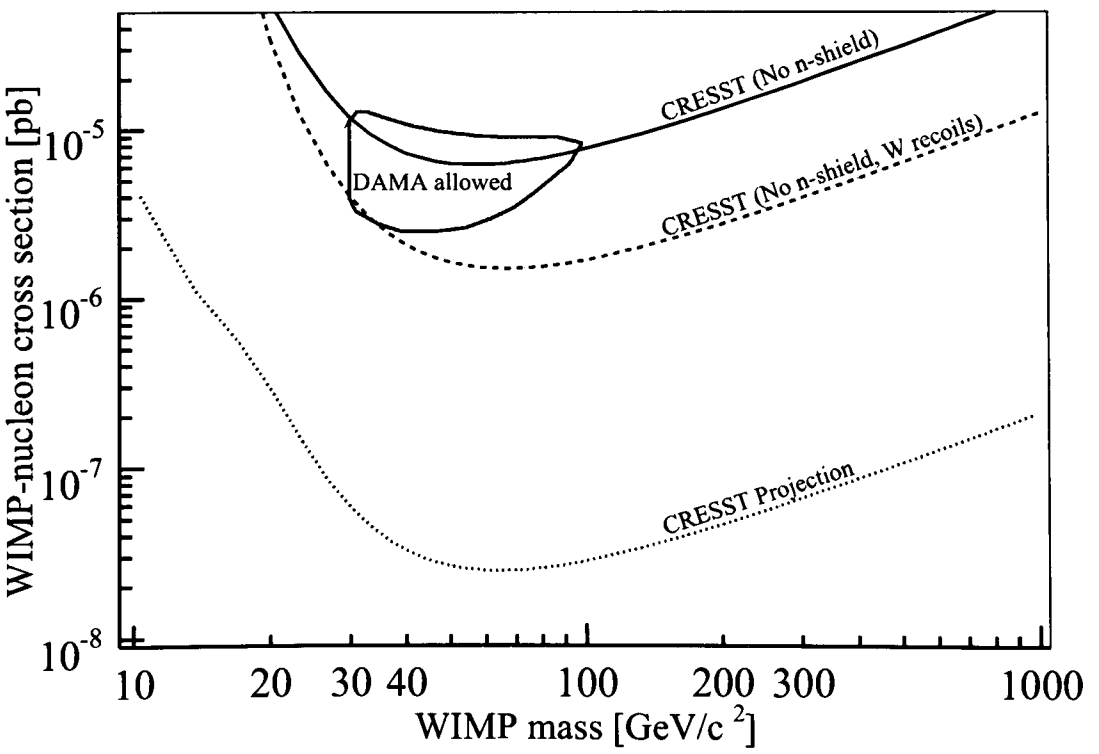

Figure 2.6: *Projected limits of the CRESST experiment*

Fig. 2.6 shows the projected limits for the CRESST experiment. They are compatible with the limits projected for the second phases of other leading experiments, including CDMS II [44], Edelweiss II [45] and Zeplin II [32]. The CRESST experiment becomes particularly interesting in the case of the detection of a positive WIMP signal. The CPSD technique can be adapted to include other target crystals such as $ZnWO_4$ or $CaMoO_4$ in order explore possible materials signatures, whilst maintaining all the other detector properties constant [46, 47]. If the differential recoil spectra for scintillators follow the trend predicted by equation (1.19), CRESST will be in a position to confirm that the observed signals come from WIMP interactions. Further examples of materials under consideration for CPSD application are given in chapter 6.

Future experiments are being planned for the case where no positive WIMP signal is detected. One option under consideration is the the construction of large array of CPSD based on CRESST technology, as for example in the EURECA detector [48]. In summary, the CPSD technique can look forward to an active future in the search for DM.

2.3.2 Other applications of CPSD

Neutrinoless double beta decays

The search for neutrinoless double beta decays is also an extremely important topic for particle physics. Neutrinoless double beta decays ($0\nu\beta\beta$) are forbidden by the standard model as they violate lepton number conservation. However if neutrinos are Majorana particles (massive particles which are their own antiparticle), $0\nu\beta\beta$ could be allowed [49]. The proof of the existence of Majorana neutrinos would be at least as important as the discovery of a WIMP signal. Double beta decay searches also provide constraints on any lepton violating gauge theories, including a number of supersymmetric models [50].

As opposed to DM searches which look for signals of the order of 10keV, $0\nu\beta\beta$ searches are interested in energies of more than 1MeV. The double beta signal would consist of a peak corresponding to the energy deposition of two high energy electrons, the total energy corresponding to the Q-value of the decay. CPSD are currently being considered as possible $0\nu\beta\beta$ due mainly to their high energy resolution [51, 52].

Rare radioactive decay processes

Recent results from the CRESST collaboration have reported measurements of rare radioactive processes in tungsten [53]. Though not a priority of the CRESST team, it is an indication of the power of the CPSD technique for detecting processes which were previously undetectable.

2.4 Summary

The CRESST experiment is a dark matter experiment having reported competitive WIMP limits obtained using cryogenic scintillation-photon detectors (CPSD). CPSD are a promising tool for the future confirmation of WIMP signals through exploiting the different material signatures of scintillators. The CRESST collaboration have also demonstrated that CPSD can be used to remove the majority of the background due to natural radioactivity by the active rejection of electron recoil events. The current limit on the discrimination power of CPSD comes from the low intensity of the light signal. The CPSD technique is relatively young and there is scope for a significant improvement in their performance. To improve the light signal and hence the overall performance of CPSD, two complementary methods can be used. The first is to maximise the scintillation efficiency of the crystals by understanding their spectroscopic properties. The second is to optimise the light collection efficiency by MC simulations. This second method is the main focus of this thesis, and the next chapter describes the MC program that was chosen for the simulations.

Chapter 3

MC programs for the simulation of light collection in HIS

The future of CRESST and dark matter searches will almost certainly involve CPSD detectors operating with a variety of scintillation materials. The optimisation of the light collection of these detectors will be a key element of their success and can be efficiently performed by MC simulations. The particle physics community recently faced a similar problem due to the relatively low light yield of $PbWO_4$ [54] used in the CERN Compact Muon Solenoid [55] at the CERN Large Hadron Collider. A number of programs were presented to perform simulations of the light collection and the following section aims to review these to select the program most appropriate for the simulation of CRESST modules. The selection is based on the ability of the MC programs to carry out the steps involved in the simulation of optical photon transport forms. The chapter is concluded with a discussion on the approach chosen by the selected program to simulate the physics processes of light transport in HIS, including its advantages and limitations.

3.1 The generic Monte-Carlo for HIS crystals

Any simulations of photon transport invariably require the following steps:

1) Energy deposition and photon generation

2) Photon transport processes

3) Photon detection

Two programs were identified as potential candidates suitable for the simulation of the CRESST setup. Litrani [56] is an open source program which has been extensively used for simulations of the $PbWO_4$ crystals of the CMS. Detect2000 [57] is an open source program which was designed for the simulation of HIS crystals used in gamma-cameras. By considering the steps of the "life" of the photon, the suitability of the programs is evaluated. At the same time, this allows to look at features of other published programs which could be of interest for CRESST.

3.1.1 Energy deposition and photon generation

Energy deposition and the spatial distribution of photons

The first step in photon transport simulations is to decide where to generate the photons by reproducing the mechanisms of energy deposition. The process of conversion of energy into scintillation light depends on the type of incoming radiation (γ, α, neutron...) and its energy. The energy determines the main processes of energy deposition (for example for a γ this can be via Compton scattering, the photo-electric effect etc...) which affects the spatial distribution of light production. Two approaches are used to simulate energy deposition. The first approach (used by Litrani) is to simulate the energy deposition using simple models for a reduced number of processes. The second approach (used by Detect2000) is to use an external program such as Geant4 [58] to simulate energy deposition. Litrani and Detect2000 also provide an option to generate photons isotropically from a unique point inside the crystal, an approach which is useful to investigate the position dependence of the light collection efficiency and frequently used in medical physics [59].

Photon Generation

Programs which have simulated energy deposition then need to link this with the generation of photons. The intrinsic light yield of a scintillator is usually presented as a constant number of photons per MeV. However, the intrinsic light yield per MeV of HIS is not constant, specially at low energies (E<100keV) [60, 61, 62, 63]. This is usually referred to in literature as the non-proportionality of light yield, and needs to be accounted for in MC simulations of light production. Both Detect2000 and Litrani would need to be modified to take this effect into account. So far, all that has been determined is where and in what number photons are to be generated, but not the actual photon generation. Photon creation tends to be modelled by a series of point like isotropic generations (a notable exception is the simulation of Cerenkov light). For energy deposited via Compton scattering, each point of scattering will be a source of photons with random direction.

Apart from direction, the other important property of the photons is their wavelength. Litrani offers the possibility of generating a photon emission spectrum by summing the Gaussian distributions which constitute the emission spectrum of a material. Detect2000 allows for the sampling of a user specified spectral distribution function which is not limited to a sum of Gaussians. A further feature of Detect2000 is that every photon can have a second associated wavelength in order to simulate interactions with wavelength changes, such as scattering from colour centres and wavelength shifting fibres.

3.1.2 The next step: propagation of the generated photons

The next step can involve two very different processes, namely an interaction within the bulk of a material (volume interaction) or a process at the boundary between two materials (surface interactions) such as a reflection from the face of a crystal. The implementation of the simulation of these processes in MC programs is discussed below.

Surface interactions: reflection and transmission

When a photon reaches a boundary between two materials it is either transmitted with probability T or reflected with a probability R such that $T + R = 1$. Surface absorption is a feature which is often added at this stage though technically it is a separate process preceding or succeeding a boundary interaction. The literature discusses two different approaches to calculating how reflection properties affect the light yield of an experiment. Detect2000 uses case specific models to describe surface interactions, for example metallic reflectors are defined using the Metal model. This is based on the approach used by Knoll and Henderson [64] and the Detect2000 models have been taken up by other simulation packages such as Geant4. The models used are Polish, Ground, Unified, Detect, Paint and Metal. The Unified model is the most complete of the Detect2000 models allowing for the definition of very specific reflection distributions. It is the result of detailed studies on the reflection properties of surfaces and how these affect the reflection/transmission of the crystals [65].

Litrani has a unique approach in dealing with boundary interactions. At each boundary, the Maxwell equations are solved for the particular trajectory of the photon. A reflecting surface is defined uniquely in terms of its complex refractive index, eliminating the need for case specific models. The reason for simulating boundary interactions in this way is that it is a straightforward way to implement surface interactions of birefringent materials. Litrani also allows for additional absorption and diffusion to be introduced in the construction of a surface, in order to simulate non-ideal reflectors.

The problem of simulating non-ideal surfaces (oxidised metals, de-polished crystals, thin paint) is one which has not been resolved by any published MC package, whether custom made [66, 67] or using the Detect2000 models [68, 69]. The simulation of de-polished surfaces is of particular interest as the light yield obtained from HIS can often be increased

by de-polishing some or all of the surfaces of the crystal. De-polished surfaces are surfaces for which it is not possible to approximate the local surface to a plane. This can be due to surface damage (scratches, cutting procedures) or voluntary design (sandpaper roughening). Though photon transport within a polished scintillator is well understood, the accurate simulation of reflectors and de-polished surfaces remains elusive.

Volume interactions: bulk absorption and scattering

One procedure that nearly all MC programs seem to have in common is how to determine the next volume interaction point. The distance d to the next interaction is given by equation (3.1).

$$d = \frac{-ln(R)}{\alpha_{int}} \tag{3.1}$$

where R is a random number generated in the range]0,1] (0 to 1 excluding 0 but including 1) and α_{int} is the interaction coefficient ($\alpha_{int}^{-1} = L_{int}$: the free path length). This is as far as the similarities go. The more complete programs (Litrani, Detect2000) allow for the interaction coefficients to be wavelength dependent. They also include methods for simulating the scattering of optical photons, an interaction which is often ignored in simulations of HIS [59, 70, 71]. As will be demonstrated in chapters 7 and 8, scattering in HIS plays a fundamental role in the process of light collection and cannot be omitted. This is confirmed in other papers [72, 73]. In Litrani and Detect2000, absorption and scattering are treated in a very similar way, in fact scattering is equivalent to an absorption followed by the re-emission of a photon. The interaction length (more often referred to as attenuation length) is defined by equation (3.2).

$$\alpha_{int}(\lambda) = \alpha_{abs}(\lambda) + \alpha_{scat}(\lambda) = \alpha_{abs}^{lat}(\lambda) + \alpha_{abs}^{def}(\lambda) + \alpha_{scat}^{lat}(\lambda) + \alpha_{scat}^{def}(\lambda) \tag{3.2}$$

where $\alpha_{int}(\lambda)$ is the wavelength dependent interaction length. The lattice absorption length is denoted by $\alpha_{abs}^{lat}(\lambda)$; and $\alpha_{scat}^{lat}(\lambda)$ is the Rayleigh scattering. The absorption and dispersion due to defects are denoted by $\alpha_{abs}^{def}(\lambda)$ and $\alpha_{scat}^{def}(\lambda)$ respectively. Though each of these are in theory distinct processes they tend to be regrouped into single absorption and scattering terms: $\alpha_{abs}(\lambda)$ and $\alpha_{scat}(\lambda)$. In Litrani for example, it is only possible to define these last two parameters. Detect2000 includes the possibility for dispersive scattering, i.e. a process which changes the wavelength of the photon due to colour centres in the crystal. Litrani offers a different advantage in that it is the only program allowing for anisotropic absorption and scattering, i.e. the optical properties depend on the direction of propagation of the photon. This will be an important point for the selection of the program since CRESST uses HIS which are mostly birefringent.

3.1.3 The final process: photon detection

After the process of generation and the determination of interactions taking place, the final step is to simulate photon detection. This is usually implemented in two ways, via surface detectors or volume detectors. Volume detectors operate very much the same as a normal volume, with the addition that the number of photons absorbed in the volume is recorded. Surface detectors operate like a normal surface with a supplementary absorption coefficient. The number of extra photons absorbed by this surface is the number of photons detected. The absorption properties correspond to the detection efficiency of the surface or volume. The simulation of detectors such as photo-multiplier tubes (PMTs) and avalanche photo-diodes (APDs) remains very basic in both programs and is mainly an extension of the surface detector classes. The electronic noise and the loss of resolution due to pulse amplification are not reproduced. Detailed studies of photo-sensors such as PMTs do exist [74] but the implementation of similar routines in studies of scintillators remains rare [59, 71].

3.2 Selecting the MC for the simulation of CRESST modules

Table 3.1: *Summary of the main features available in Litrani and Detect2000*

Monte-Carlo	Energy Deposition	Wavelength Dependence	Scat	Surface Interactions	Birefr	Complex Geometry
Litrani [56]	Limited	Yes	Yes	Limited	Yes	No
Detect2000 [57]	External	Yes	Yes	Limited	No	Limited

Table (3.1) shows a summary of the main features of Litrani and Detect2000. In order to assist in the selection between the two programs, a literature search was conducted on simulations using the two programs. In line with the original scope of the programs Detect2000 has been predominantly used by members of the medical imaging community [73, 75, 76, 77, 78] and Litrani is mainly used in particle physics simulations [72, 79]. The deciding factor for the selection of a program for use in this thesis was the capability to simulate birefringent crystals such as $CaWO_4$ and $ZnWO_4$. Litrani is the only program which offers this possibility. None of the programs alone could provide complete simulations of the CRESST modules and it is hoped that in the future the geometrical flexibility of programs like Geant4 or that of Okawa and Maeda [80] will be combined with the possibility of simulating birefringence as in Litrani.

In selecting the program to perform simulations of the CRESST modules, important features and limitations of MC have been considered. Two main points are noted; firstly the importance of including scattering interactions in simulations; and secondly the difficulty of simulating reflectors and de-polished surfaces. The next section presents the physics and usage of Litrani as well as additions to the code to optimise for the simulation of CRESST modules.

3.3 The Litrani MC

Before simulating the propagation of particles in matter it is necessary to define the properties and dimensions of the materials in which the particles travel. In Litrani, this is done by defining a number of materials and their optical properties. Then one needs to define the shapes that make up the setup to be simulated. Each shape is assigned a material from those already defined and a position in the setup (called a node). Litrani only has a limited number of shapes available and only allows for additive construction. This is a major limitation as it limits the complexity of the MC simulation in terms of shapes available. Some of the shapes available are: tubes, cylinders, trapezoids, parallelepipeds and cones. Once the shape's dimensions have been defined, it is placed in the geometry by affixing it to a node. The node defines the position and orientation of the shape. If any of the faces of the shape are in contact with any other shape, Litrani requires that this contact be declared.

3.3.1 Defining materials

In Litrani, the following parameters are needed in order to define the optical properties of a material:

(a) The optical type of the material

(b) The refractive index

(c) The absorption coefficient

(d) The scattering coefficient

(e) The emission spectrum

(f) The emission intensity

(a) The optical type of a material indicates if it is isotropic, uniaxial positive birefringent, uniaxial negative birefringent and anisotropic. In isotropic materials, a photon

propagating in any direction will experience the same refractive index. In all other cases, the refractive index is direction dependent.

(b) Litrani requires the refractive index to be defined in terms of the dielectric tensor ϵ. The refractive index tensor $\mathbf{n}$ is defined by $\mathbf{n^2} = \mu\epsilon$ where μ is the magnetic permeability of the material. The dielectric tensor can always be diagonalised to produce 3 values which correspond to the optical axis of the crystal. If the crystal is non-isotropic, Litrani requires two (uniaxial) or three (anisotropic) values for the diagonal elements of the tensor (which can be wavelength dependent) as well as the direction of the optical axes.

(c) As for the dielectric tensor, the absorption coefficient can be entered as anisotropic in Litrani. The absorption length can also be wavelength dependent.

(d) The scattering coefficient in Litrani is isotropic and can be wavelength dependent. This scattering is not necessarily due to Rayleigh scattering but can also be due to crystal defects.

(e) To simulate an emission spectrum in Litrani the material must be defined as fluorescent. A fluorescent material is assumed to have a spectrum composed of a sum of Gaussian bands. This permits the simulation of most spectra as long as these are understood in terms of their composing bands.

(f) A routine was added to Litrani to include effects due to the non-proportionality of the intrinsic light yield with energy. The intrinsic light yield is entered for a number of energies, and is obtained by interpolation for intermediary points.

3.3.2 Defining reflectors

The approach for defining reflectors is very much the same as for defining a material. A reflector is a material that does not support photon propagation in its bulk and hence is not associated with a shape but is associated with a surface. However this surface must belong to a shape and as such the complexity of reflector shapes is limited. The advantage of this method is that the reflection properties are uniquely defined by the complex dielectric tensor. The disadvantage of this technique is that the optical properties of realistic reflectors (metal + oxidised layer) are hard to reproduce. In order to reproduce the behaviour of realistic reflectors, Litrani contains a routine for supplementary absorption. This is implemented by absorbing a defined fraction of photons which would have otherwise been reflected. The simulation of diffusion is carried out in very much the same way. A diffusion coefficient is defined and the corresponding proportion of reflected photons are re-directed using a distribution corresponding to generally observed diffusion patterns [56] (3.3).

$$\frac{dN}{d\Omega} = cos(\theta)sin(\theta)d\theta d\phi \tag{3.3}$$

Despite these routines, the validity of the simulation of complex reflectors must be taken with a pinch of salt.

3.3.3 Defining sources of photons

When simulating experiments where photons are created by the deposition of energy from particles, defining the source of photons requires the simulation of the energy deposition mechanisms. The standard release of Litrani provides routines for energy deposition via pair production and Cerenkov radiation, in line with its purpose as high energy physics program. The simulations that will be performed for this work required the addition of routines for energy deposition via the photo-electric effect and Compton scattering. The

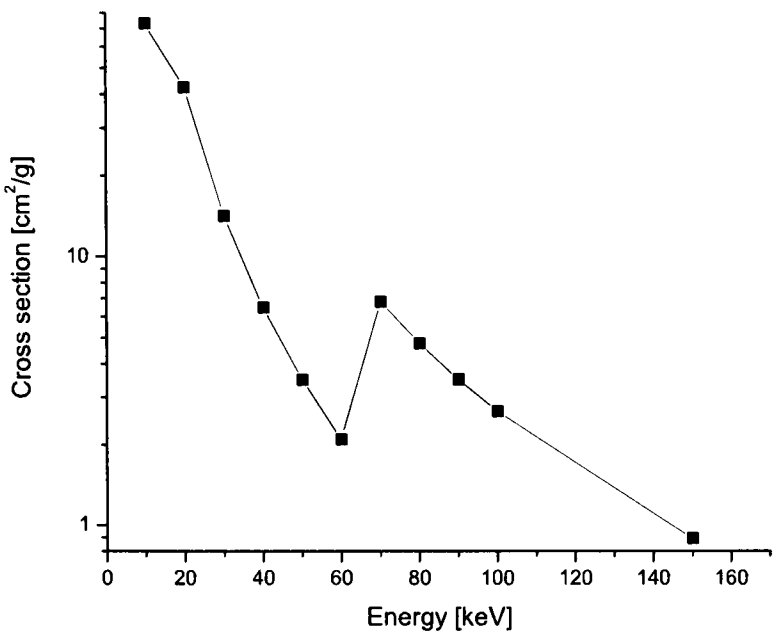

Figure 3.1: *Photo-electric cross section of x-rays in $CaWO_4$ including some features due to absorption edges [81].*

routines and their implementation for a $CaWO_4$ crystal are described below.

The photoelectric effect is implemented by considering how far γ-rays travel inside the crystal. The path length L of the radiation in the crystal is related to the cross section by equation (3.4).

$$L = \frac{1}{\sigma\rho} \tag{3.4}$$

where ρ is the density of the material. Literature often refers to a model developed by H.Messel et al. [82] to calculate the photo-electric cross section. However this model is limited to elements that do not have a high atomic number which excludes calculations for $CaWO_4$ due to the constituent W nuclei. The photo-electric cross sections used are provided by a database [81] and the values used in the MC are shown in Fig. 3.1. Cross-sections for energies in between the points presented are obtained by linear interpolation.

It is not possible to use the same database to produce the cross sections for Compton scattering since it is also necessary to generate the angular dependence of the scattered photons. The simulation of Compton scattering is based on a routine published by F.Arqueros et al. [83]. The formula for calculating the Compton cross-section per nucleon is shown in equation (3.5).

$$\sigma_{KN} = 2\pi r_e^2 \left[\frac{1+\gamma}{\gamma^2} \left(\frac{2(1+\gamma)}{1+2\gamma} - \frac{ln(1+2\gamma)}{\gamma} \right) + \frac{ln(1+2\gamma)}{2\gamma} - \frac{1+3\gamma}{(1+2\gamma)^2} \right] \tag{3.5}$$

where $r_e = 2.82\text{x}10^{-15}$m is the classical electron radius and γ is energy in units of electron mass. The formula used for calculating the scattering angle is shown in equation (3.6) below (equation (3.5) is the integral of (3.6)):

$$\frac{d\sigma_{KN}}{d\Omega} = \frac{r_e^2}{2[1+\gamma(1-cos\theta)]^2} \times \left[1 + cos^2\theta + \frac{\gamma^2(1-cos\theta)^2}{1+\gamma(1-cos\theta)} \right] \tag{3.6}$$

The scattering angle defines the amount of energy deposited. The energy deposited due to a Compton scattering of angle θ given by equation (3.7).

$$E = \frac{\gamma m_e c^2}{1+\gamma(1-cos\theta)} \tag{3.7}$$

where m_e is the electron mass. At energies <0.2 MeV, coherent (Thompson) scattering starts to play an important role relative to Compton scattering. Since at these energies the photo-electric cross-section dominates the overall scattering cross-section by a few orders of magnitude, Thompson scattering is not considered to play an important part in the energy deposition and is omitted.

The routines for the simulation of the photoelectric effect and Compton scattering define how much energy is deposited in the crystal and where. The routine present in the standard release of Litrani to convert the deposited energy into a number of photons to generate assumes an intrinsic light yield which is proportional to the energy deposited.

A routine was added to account for the non-proportionality of light yield of HIS. The non-proportionality curve for $CaWO_4$ was obtained from measurements performed by Moszyński et al. [84]. This completes the modifications made so that Litrani can be used to simulate interactions due to γ interactions $\leq$1MeV. Once the number of photons to be generated is determined, the photons are generated with an isotropic distribution and with a wavelength distribution corresponding to the input of the user. From here the photon propagation routines take over.

3.3.4 Photon propagation and detection

The propagation of photons in a medium is completely defined by the Maxwell equations and the optical properties of the medium. The Maxwell equations can be solved using the plane wave equations for the electric (E) and magnetic (H) fields:

$$E = E_0 e^{i(\omega t - k.r)} \tag{3.8}$$

$$H = H_0 e^{i(\omega t - k.r)} \tag{3.9}$$

where k is the wave vector, and ω is the angular frequency of the wave. The wave vector can be rewritten in terms of the complex refractive index ($\tilde{n}$= n(1-iχ)) and the angular frequency as shown in equation (3.10):

$$k = \frac{\omega \tilde{n}}{c} \tag{3.10}$$

where "c" is the speed of light. The plane wave equations can thus be rewritten as:

$$E = E_0 e^{-\frac{\omega \chi}{c} r} e^{i\omega(t - \frac{n}{c}.r)} \tag{3.11}$$

$$H = H_0 e^{-\frac{\omega \chi}{c} r} e^{i\omega(t - \frac{n}{c}.r)} \tag{3.12}$$

All the information pertaining to the propagation of photons is contained in these equations. The absorption coefficient is equal to $\frac{2\omega\chi}{c}$ and the transmission and reflection coefficients at a boundary can be calculated using Maxwell's equations. In Litrani, the quantities such at the complex refractive index are entered as wavelength dependent tensors, meaning that birefringence and wavelength dependence can also be accounted for. It is only when additional properties such as defect scattering and diffuse reflections are added that reflectors and bulk materials need to be distinguished.

The detection of photons in Litrani is operated using the same principles as for the rest of the program. A detector has either the properties of an absorbing optical material (photons can propagate through the material) or of an absorbing surface. Any photon which stops in the volume or is absorbed at the surface are registered so that the total number of photons can be retrieved. The number of photons detected can be moderated by the introduction of a quantum efficiency. This concludes the principles of photon propagation and detection in Litrani. Though the implementation of the propagation algorithms are complicated, the basis of Litrani is that the code is as close to possible to the physics processes that take place in HIS.

3.4 Summary

From a review of commonly available MC programs, it is considered that Litrani offers the best possibilities for the simulation of CRESST modules. Litrani not only offers the possibility to simulate wavelength dependent processes including scattering and photon emission, it also permits the simulation of anisotropies which are common in HIS. Six input parameters have been identified as factors necessary to perform accurate simulations of HIS. Some can be measured directly by experiment, as is the case of the emission spectrum, the time decay and the refractive index for example. The measurements of

these parameters are described in chapters 4-7. Chapters 7-8 describe how to obtain the parameters such as scattering and absorption which cannot be measured directly. Armed with the proper input parameters and an appropriate MC tool, the optimisation of the light collection in CPSD can be carried out. The next chapter presents methods that can be used to measure the scintillation properties which are necessary input MC parameters.

Chapter 4

Luminescence processes in HIS and their investigation

Future phases of CRESST, and indeed future cryogenic dark matter experiments will use a range of target materials to detect WIMP interactions. Cryogenic phonon-scintillation detectors (CPSD) offer unrivalled possibilities for the confirmation of WIMP signals by comparing differential recoil spectra. The successful implementation of a material as a CPSD is determined primarily by its scintillation intensity. There are two main solutions to increase the amount of light detected which correspond to the focus of the current work. A first solution is to optimise the light collection efficiency, a process which can be carried out using MC simulations. The second solution is to increase the number of photons produced by a scintillator. This can be achieved by understanding the scintillation properties of the material. Is is also of particular interest for CRESST and future large scale experiments such as EURECA to understand how the luminescence varies between crystals of the same material. Understanding the scintillation properties is therefore necessary for providing input parameters for light collection optimisation by MC, for optimising the scintillation efficiency of materials and for understanding how to compare results between two CPSD. This chapter looks at the theory of scintillation mechanisms, paying particular attention to temperature dependent effects. This is followed by a description of experimental techniques that can be used to investigate the luminescence properties of scintillators.

4.1 Energy levels in crystals

4.1.1 Conduction and valence bands

Luminescence occurs when an electron relaxes from being in an excited state back to the ground state through the emission of a photon. Luminescence is an umbrella term for light emission processes which are not due to incandescence. Luminescence processes include for example fluorescence (prompt emission of light) and phosphorescence (delayed emission of light). For a material to be a scintillator (i.e. luminescent) it must have discrete energy levels or relaxation will occur by thermal interactions. The existence of separate energy bands can be demonstrated using the Krönig-Penney model [85]. The wave function of the electrons must be a solution of the one dimensional Schrödinger equation:

$$\frac{d^2\Psi(x)}{dx^2} + \frac{2m}{\hbar^2}(E - V(x))\Psi(x) = 0 \tag{4.1}$$

In one dimension, the potential due to the crystal lattice (i.e. periodic representation of atoms or ionic complexes) is a repetition of a regular potential: V(x) = V(x+a) where a is the one-dimensional lattice constant. The Krönig-Penney model approximates the regular Coulomb potential by a series of square well potentials. The wave function which is a solution to this Schrödinger equation has the same periodic properties as that of the potential [86]. This result is known as Bloch's theorem, and the resulting wave function can be written as $\Psi(x) = u_k(x)e^{ikx}$ where $u_k(x)$ is a function which depends on k and varies with the same period as V(x). It can further be shown that solutions to the Schrödinger equation only exist for certain energy eigenvalues which form the discrete energy levels required for photon emission. Transferring this to three dimensions with a Coulomb potential produces the same structure of forbidden and allowed energy bands albeit with different energies.

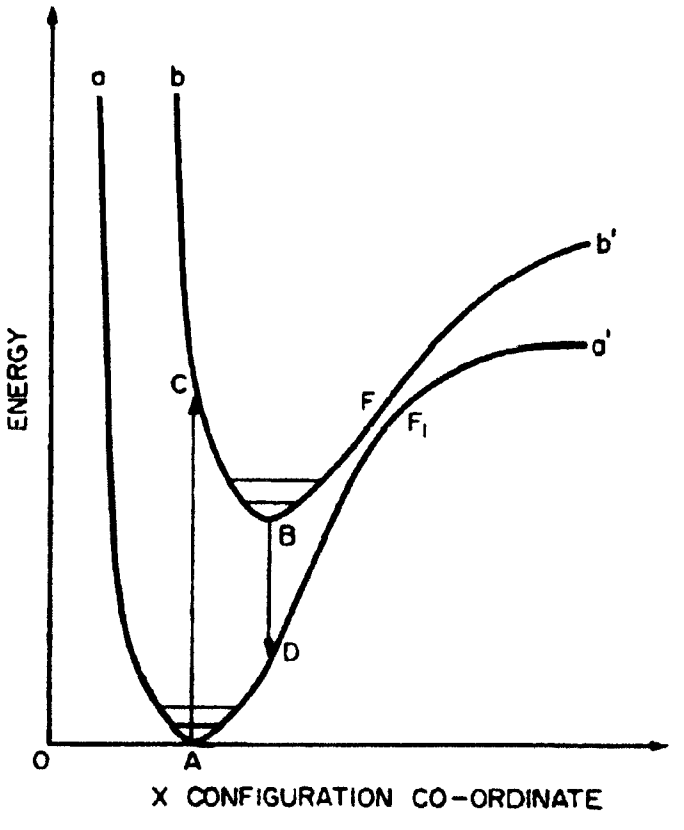

Figure 4.1: *Configuration coordination model of scintillation of a di-atomic crystal*

Fig. 4.1 shows the potential energy diagram for a diatomic crystal O-A, where x-axis represents the inter-ionic distance. The curve aAa' is the ground state and the curve bBb' is the excited state. This curve is a simplified representation of what happens in more complex crystals but can serve to understand the general principles of scintillation. Transitions between the bands always occur along the vertical axis since the excitation or relaxation of the electrons occurs too fast for the inter-ionic distances to be affected (Franck-Condon Principle). However the time average inter-ionic distance can be significantly affected and is shown in the diagram as having a new average position OB. In the ground and the excited state the ion vibrates around its rest position R_0 (corresponding respectively to OA or OB on the diagram) according to the formula:

$$E = k(R - R_0)^2/2 \tag{4.2}$$

where E is the potential energy, (R-R_0) is the displacement from the equilibrium and k is the restoring constant. The difference between OA and OB (OB - OA = ΔR) is the

difference in average separation of the ions in the excited and ground states. Literature commonly refers to two special cases of ΔR [87]. For $\Delta R \sim 0$, referred to as the weak coupling scheme, the emission is characterised by a narrow line. If $\Delta R \gg 0$, there is broad band emission and this is referred to as the strong coupling scheme. These schemes will be useful when explaining the behaviour of crystals at different temperatures.

4.1.2 Excitons

To pass from the valence band to the conduction band, an electron must gain energy equivalent to the band gap E_g. The process of promotion from the valence band results in a "hole" being created in this band which has an effective positive charge. The electron and hole can form a state bound by the Coulomb potential called an exciton. The energy level of the electron (E_e) in the exciton is given by:

$$E_e = E_g + E_b \tag{4.3}$$

where E_b is the binding energy. In this case, the convention adopted is that E_b is a negative quantity. A simple representation of exciton formation is shown in Fig. 4.2. The

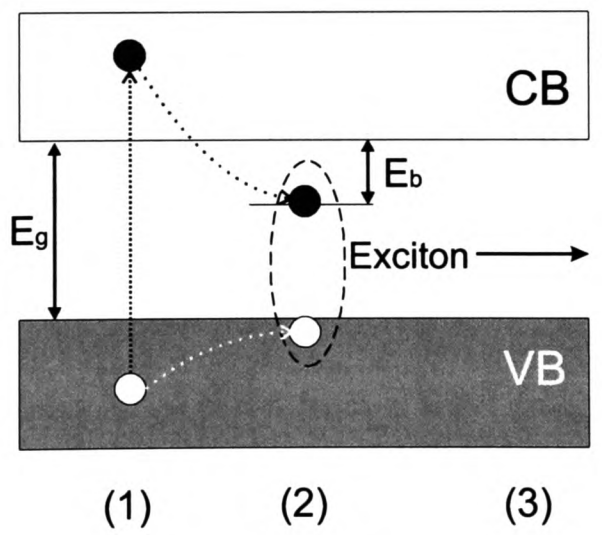

Figure 4.2: *Illustration of exciton formation. (1)An electron is excited from the valence band to the conduction band leaving a hole in the valence band. (2) The electron and hole thermalise and form a bound state. (3) If the hole is free to move, the exciton can migrate. If the hole is bound to a particular atom or ion, the exciton is called self trapped.*

binding energy also determines the size of the exciton which is equivalent to its effective Bohr radius [88]. If the size of the exciton is large compared to the lattice constant, then the exciton is referred to as a Wannier exciton. If the size of the exciton is small, the exciton is referred to as a Frenkel exciton. If the electron from the exciton is bound to an ion by a potential well then the exciton is referred to as being a self trapped exciton (STE).

4.1.3 Absorption of energy

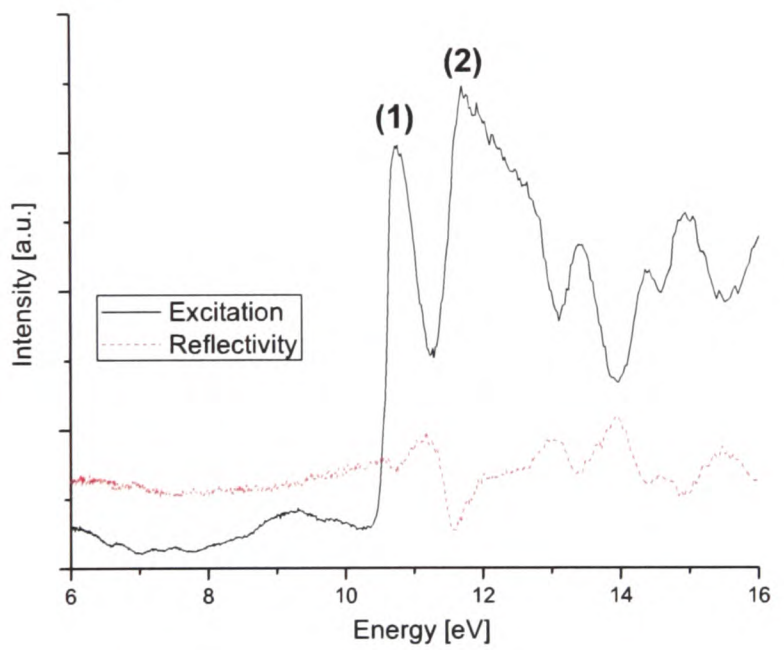

Figure 4.3: *Solid: Excitation spectrum of CaF_2. The band at (1) is due to excitonic states. The band at (2) is due to the excitation of electrons from the valence band to the conduction band. Dashed: Reflectivity spectrum of CaF_2*

To create excitons or excite an electron from a band to another, energy must be absorbed by the scintillator. For photon excitation, the energy E_{ex} is proportional to the frequency of the radiation: $E_{ex} = h\nu$ where h is Planck's constant. The absorption of energy causes electrons of the scintillator to be excited. In most cases the electrons relax via thermal modes, i.e. by emission of phonons. However if $E_{ex} > E_g$ where E_g is the energy gap of a radiative transition, then a fraction of the absorbed energy can be re-emitted as

light during the relaxation of the excited electrons. The excitation spectrum of a scintillator shows the relative amount of light emitted for different excitation energies. A peak in the excitation spectrum indicates that a radiative transition is successfully excited by the energy of the incoming photons. The excitation spectrum can thus be used to identify the emission bands of materials. In the excitation spectrum of pure CaF_2 shown in Fig. 4.3 there are two pronounced increases in the integrated luminescence. These indicated that the incoming radiation energy matches the energy difference between two bands or the energy needed to create excitons. Previous works indicate that the peak at ~10eV is due to excitonic states whilst the band at ~12eV can be attributed to transitions between the valence band to the conduction band [89].

The peaks in the excitation spectrum are caused by an increase in the probability of absorbing the radiation of a particular excitation, and/or because the radiation excites a transition which has a higher scintillation efficiency. A complementary way of obtaining information on the band structure is by measuring the reflectivity spectrum [90, 91]. The reflectivity spectrum measures how much of the incoming excitation radiation is reflected from the surface of the crystal. If more light is absorbed by the crystal (due to for example the excitation energy matching a band-gap energy) then the intensity of the reflected light decreases. Excitation and reflectivity studies thus ideally complement each other for the identification of the band structure of HIS.

If the energy of the incoming radiation is higher than the energy of the band gaps (for example for γ-ray excitation), the absorption of energy occurs through multiple electron excitations, causing an increase in intensity but little change in the emission spectrum. Vacuum ultra-violet (5-50eV) measurements give information on the band structure which allows to identify the transitions responsible for the observed luminescence and helps to identify potential improvements. Measurements with E_{ex} >1keV show what intensity of

luminescence can be expected for materials in WIMP interactions. Both are important in selecting and improving potential CPSD materials.

4.1.4 Emission of light and the luminescence spectrum

One of the most important considerations for luminescence properties of a material is that the spectrum of emitted light should match the detection equipment. In the context of CRESST, this means matching the reflectivity range of reflectors and sensitivity range of the detector. A further motivation is that by understanding the emission spectrum, it may be possible to identify ways in which to increase the intrinsic light yield of the scintillator. Two main types of emission can be distinguished, one which is intrinsic to the material and another extrinsic. Intrinsic emission is the emission associated with a pure crystal of the scintillator. Extrinsic emission can be due to defects in the lattice, impurities in the crystal or dopants included with the intent of modifying the luminescence properties. Rare event searches have a special need to identify dopants as these not only modify the light output but can also introduce radioactive isotopes. It is also a possibility that the removal of defects leads to a decrease in emission, rendering the material less attractive as a CPSD. The energy of the emission band reveals information on the band structure of the material which eventually can lead to the identification of intrinsic and extrinsic emission. Most of the scintillators considered for CRESST will be intrinsic scintillators, i.e. scintillators with no doping as dopants are often radioactive or come accompanied with radioactive contaminants. Broadly speaking the scintillators investigated have chemical composition of type XMO_4 where X = Ca, Zn, Cd... and M = W, Mo... and can be divided into two structure types, scheelites and wolframites. The structure of a crystal determines the band structure and hence is a major influence on the luminescence properties. The band structure of generic tungstate scheelites and wolframites is shown in Fig. 4.4. Similar energy diagrams apply for scheelites and wolframites formed with other metallic ions such as molybdates. Intrinsic radiation in scintillators of type XMO_4 with scheelite

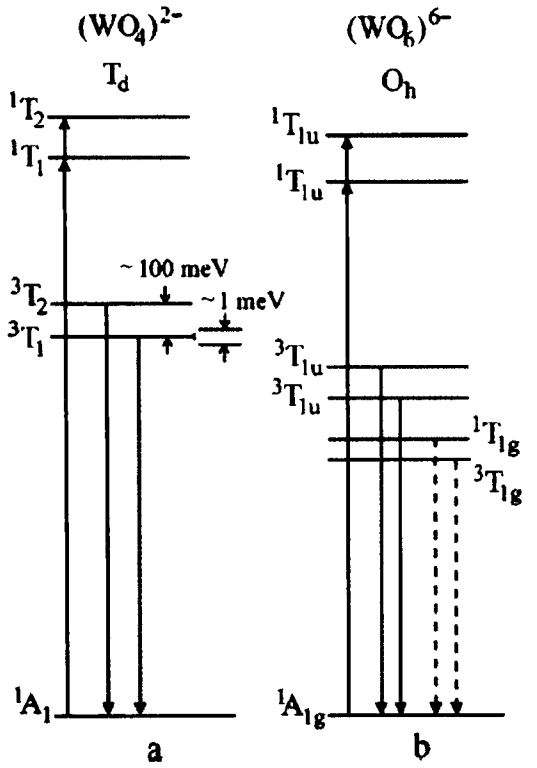

Figure 4.4: *Schematic diagram of the energy levels in (a) scheelite and (b) wolframite crystals. The full arrows indicate allowed absorption and radiative transitions. The dotted arrows denote parity forbidden transitions.*

structure is due to electronic transitions in the MO_4^{2-} complex. In wolframites the intrinsic component is due to electronic transitions in the MO_6^{6-}. It is worth noting from the figures that in both cases the main luminescent transition is composed of a superposition of emission from bands separated by only ~100meV. A measurement of this energy difference has only recently been carried out using dedicated equipment by Itoh and Sakurai [92]. Understanding the energy levels of scintillators is also key to explaining the temperature dependence of their luminescence properties.

4.2 Temperature dependent effects

The spin-orbit splitting of the emitting ^3T level in scheelites and the $^3T_{1u}$ levels in wolframites is thought to be responsible for the increase of the decay time as temperature decreases [93]. Transitions from the lower level of the spin-orbit split states is thought to be forbidden such that the energy levels can be represented by Fig. 4.5. For $\tau_{31}, \tau_{21} \gg \tau_{23}$,

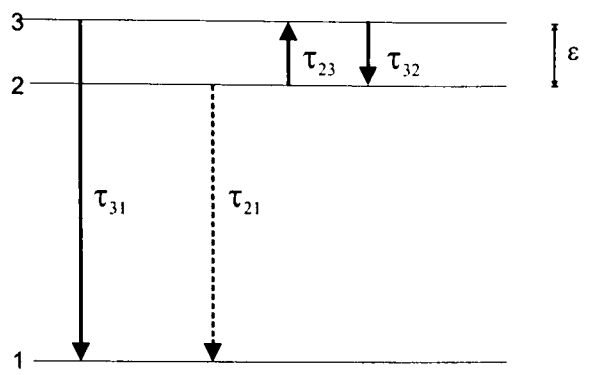

Figure 4.5: *Three level scheme of XMO_4 used to explain the sharp increase in the long component decay constant. ϵ is the energy gap between the radiative and metastable levels, and each τ is the decay time constant for each energy transition.*

the expected decay time is given by equation 4.4 [94].

$$\tau_L = \frac{1 + e^{\frac{\epsilon}{k_B T}}}{\tau_{31}^{-1} + \tau_{21}^{-1} e^{\frac{\epsilon}{k_B T}}} \tag{4.4}$$

where k_B is the Boltzmann constant. As T$\rightarrow$0, $\tau_L \rightarrow \tau_{21}$, and in a "standalone" ion of WO_4^{2-} the decay time would become infinite as the transition is forbidden. However it is thought that the perturbations caused by the inter-ionic bonding distorts the bands allowing for an eventual relaxation through radiative transitions. This explains the low temperature behaviour of the emission of the scintillators investigated.

At high temperatures (T$\gg$50K), the spin-orbital split levels can effectively be viewed as one level since the kinetic energy of electrons in any of the bands is much greater than the band gap. This allows us to use the configuration coordinate model and the interpretation given to it by Mott [95]. A luminescent state can decay through two predominant channels, a radiative and non radiative channel. The radiative process occurs with a probability $1/\tau_r$ whilst the non-radiative process occurs via thermal activation with a probability of $\nu e^{-\Delta E/k_B T}$ where ΔE is the activation energy. The constant ν is called the frequency factor and is related to the rate of transfer of the population from the excited-state to the

ground-state. The temperature dependent decay time is then given by:

$$\frac{1}{\tau(T)} = \frac{1}{\tau_R} + \nu e^{-\Delta E/k_B T} \tag{4.5}$$

These values can in turn be used to explain the temperature dependence of the total intensity of luminescence (Mott's formula).

$$I(T) = \frac{\tau(T)}{\tau_R} = \frac{1}{1 + Ce^{-\Delta E/k_B T}} \tag{4.6}$$

where C=$\tau_R \nu$. An application of Mott's formula to HIS can be found in [96].

Equations (4.5) and (4.6) are only valid at high temperature but the approximation to one non split band can also be used to extract information on low temperature properties not affected by the time constants. Continuing with the configuration model in the strong coupling scheme (broad band emission), it can be shown that the temperature dependence of the width of the emission band is given by the canonical co-tangential equation [97]:

$$W(T) = W_0 \sqrt{coth(\hbar\omega/2kT)}, \tag{4.7}$$

where W_0 is the bandwidth at 0 K and $\hbar\omega$ is the energy of the lattice vibrations that interact with the electronic bond. This gives the energy at which phonons are produced during the interaction with radiation. These phonons are not in thermal equilibrium and will eventually interact to become thermal phonons. Assuming a Debye distribution of the thermal phonon density of states, it is also possible to calculate the cutoff energy of the thermal phonons [98]:

$$E(T) = E_0 + CT^4 \int_0^{\hbar\omega_D/kT} x^3 dx/(e^x - 1), \tag{4.8}$$

where E_0 is the energy of the transitions at 0 K, $\hbar\omega_D$ is the Debye cut-off energy of the

acoustic phonons and C is a numerical constant. These results are very interesting in the context of CPSD as they show that luminescence measurements can be linked with the phonon properties of the crystals. At very low temperatures, the Debye cut-off energy can be directly related to the molar specific heat of the scintillators (c_m) as shown in equation (4.9).

$$c_m = 1941(\frac{kT}{\hbar\omega_D})^3 \; Jmol^{-1}K^{-1} \tag{4.9}$$

To obtain the phonon properties by luminescence measurements requires measuring the peak width and position with a high degree of precision. The rest of this chapter will now be dedicated to explaining the various apparatus which were used to perform luminescence measurements.

4.3 Apparatus used to measure luminescence properties of HIS

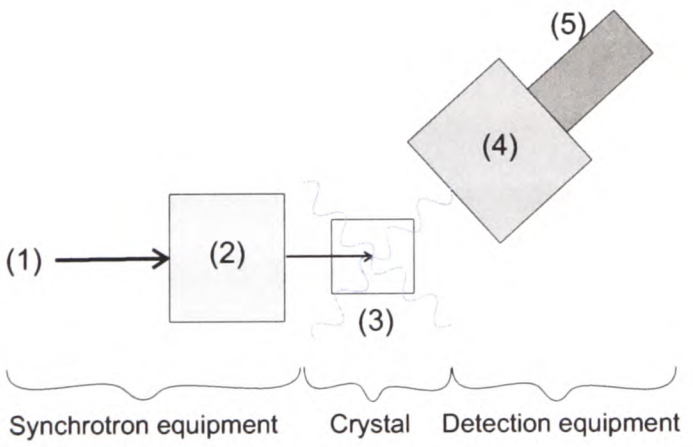

Figure 4.6: *(1) Synchrotron radiation is produced by electrons held in a storage ring. (2) The radiation is directed onto a primary monochromator which permits the selection of a specific radiation energy. (3) The synchrotron radiation hits the scintillation sample producing light. (4) Some light arrives at the entrance slit of a secondary monochromator which can be used to select photons of a particular wavelength. (5) The photons are detected by equipment such as a PMT or a CCD camera.*

Apparatus used to study scintillators for this work can be broadly divided in two

categories: synchrotron apparatus and time decay apparatus. The time decay apparatus was custom built and is described in the following chapter. The experiments using synchrotron radiation are described below. Fig. 4.6 shows the important features of a simplified synchrotron facility. Synchrotron light (1) is directed by a series of gratings and reflectors onto a primary monochromator (2) which is used to select the energy of incoming radiation that will excite the sample (3). The synchrotron radiation causes scintillation light to be produced in the crystal which escapes in all directions including toward a secondary monochromator (4). In general, the crystal is placed in a reflective chamber to maximise the amount of light collected and increase the sensitivity of the setup. The secondary monochromator is used to select the wavelength of the scintillation light which is let through to the detector. The intensity or spectrum of the scintillation light is measured using a PMT or a CCD camera (5).

In the course of this work, two synchrotron facilities were used to investigate the properties of scintillators which are candidates for implementation as CPSD. The first is the SuperLumi station at HASYLAB (Hamburg, Germany) operating in the energy range 4-40 eV [99]. This facility is best suited for exploring the spectroscopic properties of materials in order to define their band structure. The second is the mobile luminescence end-station (MoLES) at SRS Daresbury laboratory [100] that provides monochromatic X-ray photons in the range 2-4 keV. This facility is ideal for exploring spectroscopic properties in the range of energies close to those expected for WIMP interactions. A description of the main components of these facilities is given below.

4.3.1 The Superlumi Station at DESY

The SuperLumi setup is attached to the DORIS III storage ring of the DESY (Deutsches Elektronen-Synchrotron) laboratory. The schematic diagram of the experiment is shown in Fig. 4.7. Superlumi is provided with UV and VUV (vacuum UV) photons created by

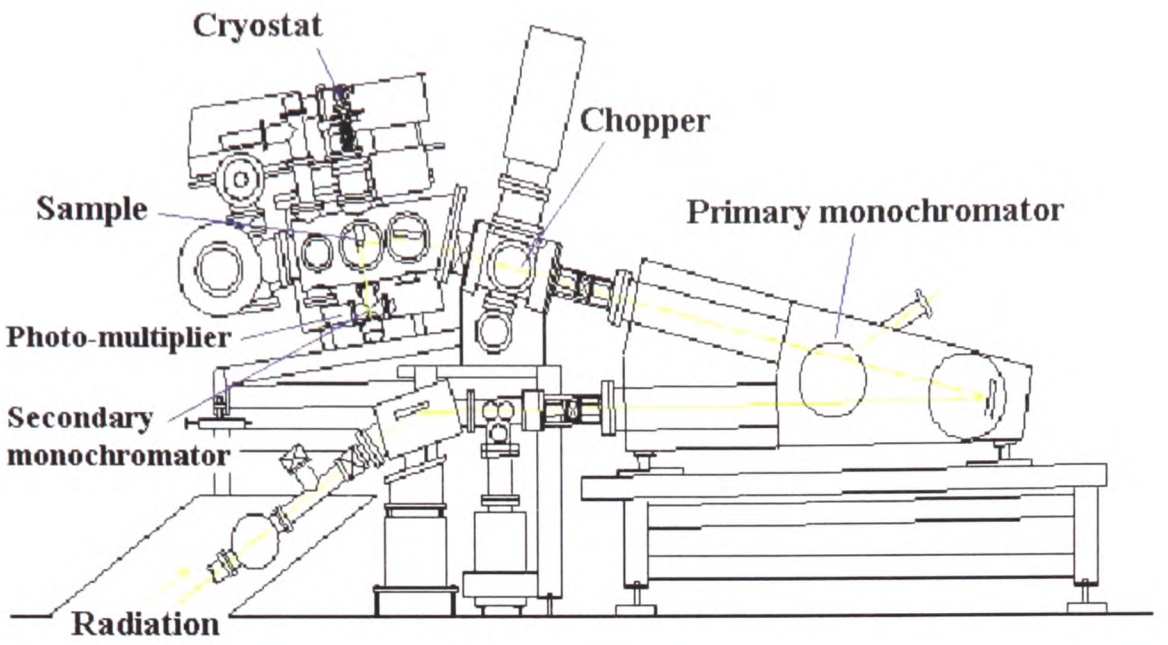

Figure 4.7: *The Superlumi facility*

synchrotron radiation from the DORIS storage ring. The path of the synchrotron radiation is shown in Fig. 4.7. The primary monochromator is a CGA/M^{c}Pherson normal incidence monochromator. Two gratings are available to select the range of excitation energies. An Al grating is used to select the energy of the synchrotron radiation in the range 4.2-24eV. Additionally a quartz (SiO_2) filter is available for the suppression of secondary order wavelengths when using the Al grating. A Pt grating is available to allow through photons in the range 24-40eV for which the Al grating is opaque. The beam intensity has to be corrected for the relative transmissivity of the primary monochromator for each wavelength. The intensity of the synchrotron radiation let through by each of the gratings (and filters) is shown in Fig. 4.8(a). The curves in this figure are obtained by illuminating a sample of sodium salycilate ($C_7H_5NaO_3$). Sodium salycilate obeys the Kasha-Vavilov rule which states that for non ionising radiation, the quantum yield of a material is independent of the excitation energy as a consequence of there being only one main relaxation mechanism (internal conversion + radiation). Therefore, any variation in the luminescence intensity of sodium salycilate must be due to changes in the intensity of the arriving synchrotron radiation. The Kasha-Vavilov rule only applies to certain fluorophores (typically organic), and does not apply to the HIS under investigation.

The samples are placed in a vacuum chamber and can be cooled to 8K using a helium

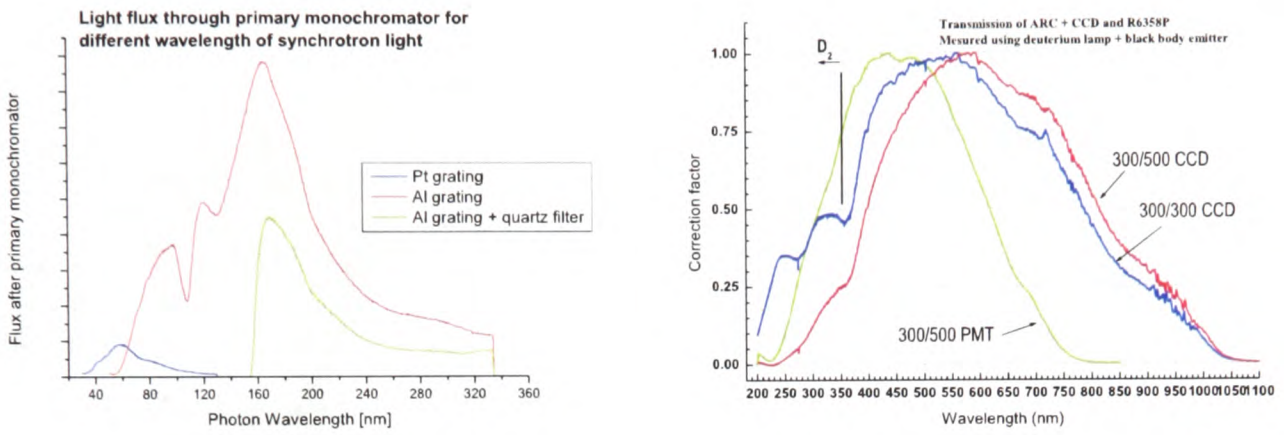

(a) (b)

Figure 4.8: *(a) Intensity of radiation let through by the primary monochromator gratings and filters. (b) Correction curves for the gratings and the detectors of the Superlumi experiment*

flow cryostat. For all measurements, the sample position relative to the beam is optimised to detect the maximum intensity of synchrotron radiation reflected by the sample surface. This minimises contamination of the luminescence light by harmonics of the synchrotron photons. The reflected radiation is detected with a XP2020Q PMT. In order to examine the spectroscopic properties of individual bands, the emitted light is directed on a secondary monochromator which is used to narrow its bandwidth to approximately 200nm before detection. The secondary monochromator is a Spectral Pro 308 Czerny-Turner monochromator from the Acton Research Company (ARC). The emitted light is detected either by a Hamamatsu R6358 PMT (range 185-830nm) or using a Princeton Instruments 1100PB/UVAR LN CCD. As for the primary monochromator, there is the option of having various gratings to tune the performance of the detector. For all measurements presented here, the grating used had 300 grooves/mm with 500nm blazing (abbreviated to 300/500nm) unless specified otherwise. Since the reflectivity of the grating is not constant over the range of light detected, it is necessary to obtain a correction curve for the grating. Fig. 4.8(b) shows the correction curves for the gratings used. The curves include

corrections for the responses of the PMT and CCD and any other optical elements. All the data presented in this work are corrected for the effects of the detection system.

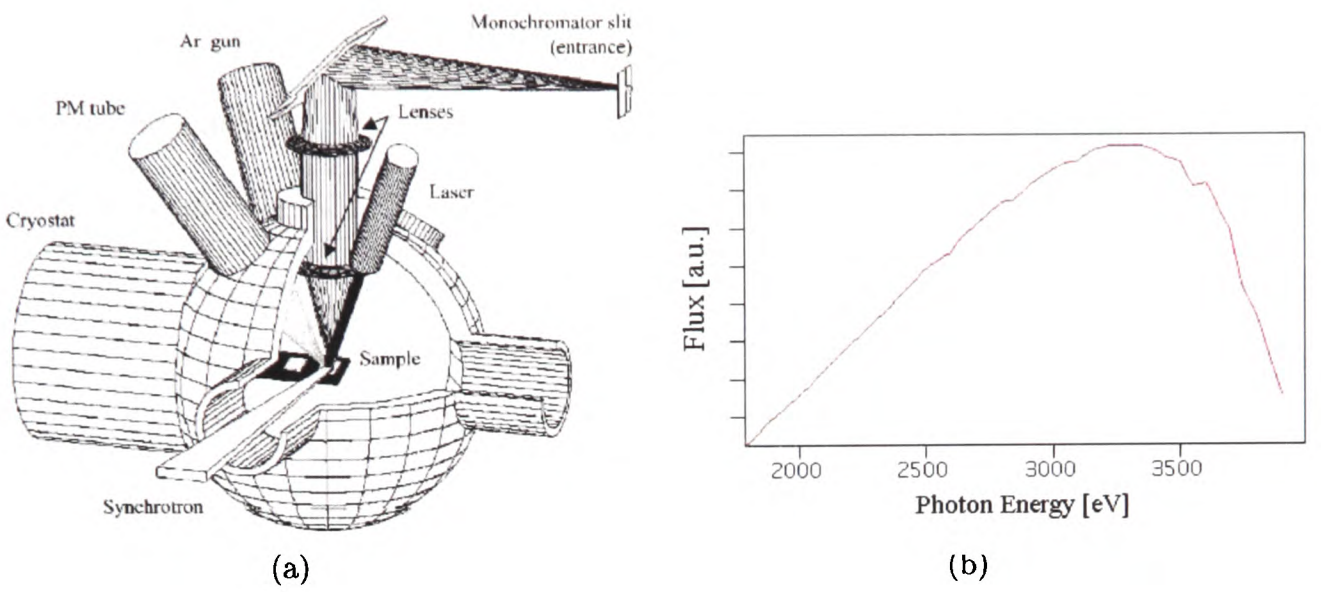

Figure 4.9: *(a) Schematic diagram of the MoLeS vacuum chamber; (b) Flux of synchrotron light received from beam-line 4.2.*

4.3.2 The MoLeS at the Daresbury SRS

The mobile luminescence end station (MoLeS) was used at station 4.2 of the Daresbury Synchrotron Radiation Source (SRS) [100]. Synchrotron radiation from the SRS is focused onto a double crystal primary monochromator using a series of quartz mirrors. The monochromator has two rocking InSb(111) crystals which select the synchrotron radiation energy in the range 1.9-4.5keV. Further details of the mirror/crystal setup can be obtained from [101]. The energy dependence of the radiation intensity received from beam-line 4.2 is shown in Fig. 4.9(b). The synchrotron radiation then arrives in the vacuum chamber in which the sample is kept. A schematic diagram of the MoLeS chamber is shown in Fig. 4.9(a). As in the SuperLumi setup, both the excitation and luminescence spectra can be measured by a combination of primary and secondary monochromators. The secondary monochromator to select the wavelength of the detected light is a Triax-190 monochro-

mator (manufactured by Jobin-Yvon). The diffraction grating had 1200grooves/mm and 630nm blaze unless specified otherwise. An important additional feature of the MoLeS chamber is the lens placed close to the sample in order to maximise the amount of light collected. The emitted light is then detected by a Hamamatsu R2949, R2658P, or Electron Tubes 9111WB PMT depending on the wavelength of the light to be detected. As for the SuperLumi facility, corrections are applied to account for the sensitivity of the light detection system to different wavelengths. Overall the MoLeS setup is very similar to that at SuperLumi, with one notable difference. The MoLeS setup is mobile, meaning that it can be affixed to beam lines of different energies to explore a wider range of excitation energies. MoLeS and SuperLumi are complementary techniques to look at the spectroscopic properties of scintillators, the first for examining scintillators at energies close to the expected WIMP interaction energy, and the second for examining the spectroscopic properties of scintillators. However they are not particularly suited for measuring the long time decays of pure HIS. This prompted the development of a new method to measure these time decays in order to extract the maximum information possible on the scintillation properties of HIS which is discussed in the following chapter.

Chapter 5

The multi-photon coincidence counting technique (MPCC)

This chapter contains a description of custom built apparatus used to measure the decay time constants of scintillators by recording the arrival time distribution of scintillation photons. The multi-photon coincidence counting (MPCC) technique was designed to facilitate the measurement of decay time spectra over a wide range of temperatures by accelerating the data taking process with respect to conventional methods. Furthermore, by using statistical analysis methods on the recorded pulses, the MPCC technique allows the removal of multiple event contributions which can cause the misidentification of extra decay components, and therefore errors in the evaluation of the potential application of scintillators as CPSD materials. As an example literature reports a possible third long decay component in $CaWO_4$ [84] which the MPCC technique showed was due to multiple events [102]. To ensure that the removal of multiple events introduces no bias in the measurement of the decay characteristics, two independent cuts have been developed based on a Shapiro-Wilks test and non-homogeneous Poisson statistics. The performance of the cuts is tested on MC data. The MC simulation program is able to produce data corresponding to single or multiple events.

5.1 Conventional techniques for measuring scintillation decay times

Decay time measurements are an essential tool in understanding the luminescence properties of scintillating materials. Unlike many other applications which use HIS, rare event searches do not require scintillators to have a fast decay time. Experiments such as CRESST therefore have the possibility to use scintillators such as $CaWO_4$ which are traditionally considered as "slow". The readout circuit of the light detectors can be modified to suit slow decay times as was done for $CaWO_4$ in CRESST [43]. The multi-photon coincidence counting technique (MPCC) technique was developed in order to simultaneously measure the decay time and the light yield of potential CPSD scintillators over the range of temperature 8-350K. For reasons of practicality and costs it is desirable to speed up conventional time decay measurements techniques. Conventional techniques for measuring the light yield of a scintillator usually rely on operating the PMT in integrating mode and it is very hard to obtain timing characteristics using this method. A more common method for the measurement of timing characteristics is the delayed coincidence single-photon counting (DC-SPC) technique. The method is based on measuring the distribution of the time difference between either two photon signals from one event or the time difference between the trigger signal and a photon signal [103, 104]. The time differences are stored and plotted in the form of a histogram. This histogram is fitted to a mathematical function suitable for describing the decay mechanism. This method has excellent timing resolution ($\sim$0.5 ns) and it is commonly used for measuring decay characteristics of fast scintillators with decay time constants in the range of nano-seconds to micro-seconds. The DC-SPC technique is very good for measuring fast decay events but loses attractiveness for slow scintillators. Firstly the method requires the detection of a large number of events to produce a meaningful histogram. It also requires the probability of detection of more than one photon during a sampling period to be less than 0.01; otherwise there will be bias toward a faster decay time constant [105, 106]. To

reduce this bias the number of photons is artificially limited using a diaphragm or a filter; which reduces the rate of detected events. The accurate measurements of decay time may require measurements that last up to a few days. Such a technique is not very suitable in the case of studies on temperatures dependence of luminescence properties.

The DC-SPC also has an inherent source of error stemming from its inability to identify multiple events. A rough estimate for a decay time constant of 10 μs, a recording time of 100 μs and an event rate of 1000 s^{-1} shows that approximately 4% of the recorded events will include scintillation resulting from more than one particle interaction i.e. multiple excitations. This seemingly negligible contribution to the total signal results in a noticeable tailing effect. Thus when analysing such data one might easily misinterpret this background as an additional decay component with a long lifetime. The crystals under consideration for CPSD tend to have decay times of the order of 100μs making DC-SPC unsuited for measuring the decay times. This prompted the development of a new technique based on recording the arrival times of all detected photons from an event. Though long decay constants are usually a disadvantage, they can be advantageously exploited to implement photon counting which will allow the recognition of bad events.

5.2 Setup for the multi-photon coincidence counting (MPCC) technique

A picture of the MPCC setup is shown in Fig. 5.1(a). The crystal sample is placed inside a helium flow cryostat equipped with optical windows. An ^{241}Am (5.5MeV) alpha source is placed inside the cryostat setup as shown in Fig. 5.1(b). Two 9125B Electron Tubes photo-multipliers tubes (PMTs) are attached to quartz windows on the optical cryostat such that they are at right angles to each other. Each PMT is connected directly to a custom built fast pre-amplifier with two settings for the integration constant equal to

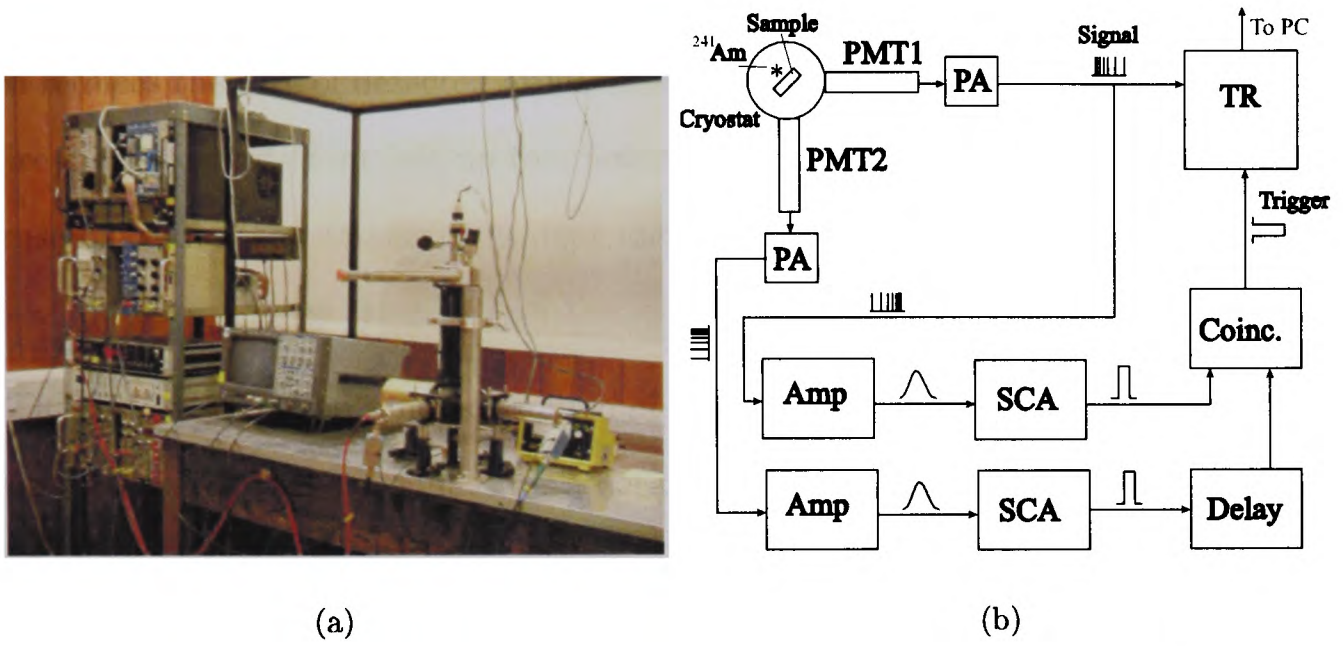

(a) (b)

Figure 5.1: *(a) Picture and (b) read out electronics of the MPCC experiment*

2.2ns or 10ns, achieved using a high speed OPA633 buffer amplifier. The signal from one PMT is split with one branch going directly to a LeCroy TR8828 transient recorder (TR). The other branch is sent via a single channel analyser (SCA) to be regrouped with the signal from the second PMT. The discrimination thresholds of the SCA are set to reduce the number of pulses with low and very high amplitudes which are respectively associated with electronic noise and spurious events caused by cosmic muons. The logic output pulses of both SCA are fed into a coincidence unit which provides the trigger for the transient recorder. If the trigger condition is met, the event is recorded by the TR and stored on a PC. The TR has a range of sample times from 5 to 80 ns and is able to record up to 16KB of data per record. Overall, the choice of the components of the DAQ circuit is determined primarily by the timing properties, the aim being to keep all timing constants of the same order of magnitude. The FWHM of photo-electron pulses is $\sim$15-20ns, corresponding to a total duration of 3-4 sampling times of 5ns which defines the resolving power of the setup. When using a 5ns sampling time, two photons must be separated by at least 3 sample periods to be resolved by the analysis software. Another circuit characteristic to consider is the time delay between the scintillation event

and the arrival of the trigger signal. The arrival time of the trigger signal depends on many factors, including the scintillation light yield, the decay time and all the time and amplification factors of the electronic circuit. However for all measurements performed, the arrival time of the trigger pulse was less than 8μs after the start of the scintillation pulses. It is therefore sufficient to set the TR pre-trigger recording time to 8μs.

5.3 Preliminary analysis and corrections

The TR writes events to a binary data file via custom made DAQ software designed using the particle physics ROOT framework [107]. The binary file is analysed using software also written using the ROOT framework. The program contains classes to represent events, scintillation pulses and all information related to the data acquisition. In this chapter the following terminology is used to describe the analysis of scintillation records: Each trigger signal results in one event being recorded. An event in this sense does not necessarily correspond to a scintillation event as the trigger could be caused by electronic noise. Each event is composed of pulses, which usually correspond to the detection of a photon, but may also be due to noise.

A typical room temperature $CaWO_4$ scintillation event is shown in Fig. 5.2(a). Fig. 5.2(b) is a close up of this event showing individual photon pulses. A series of routines were developed so that the recognition of the arrival time of the photons can be performed by software. The first routine looks to find the baseline and proceeds as follows.

- Starting from point 0, compare data points i, i+1 and i+2 in the record.
- If these are the same, then this gives the baseline
- If these are different, increment i, and restart the first procedure.

Data points which are above this baseline are set as equal to the baseline. The points are due to ringing from the electronics (photon pulses are below the baseline) and could

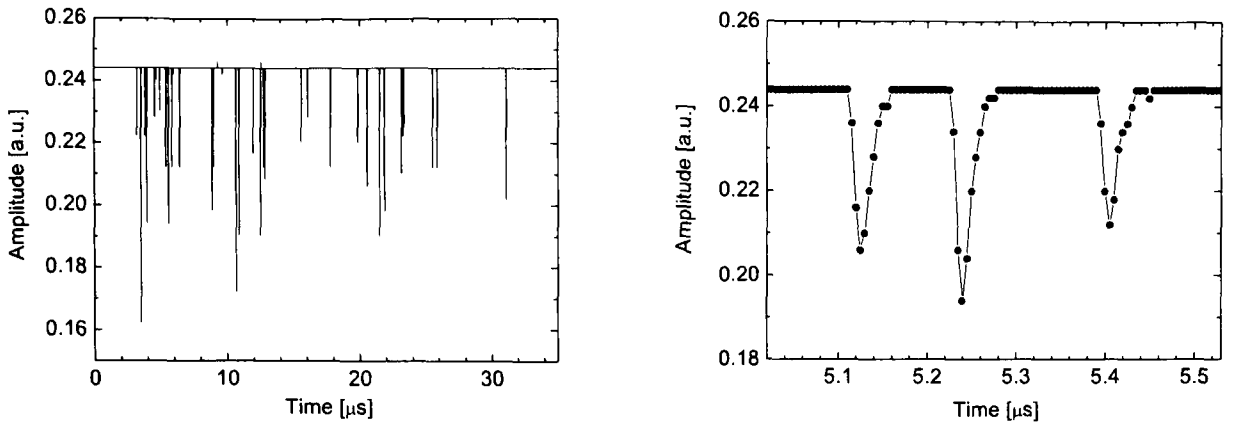

(a) (b)

Figure 5.2: *A typical room temperature $CaWO_4$ event recorded using the MPCC apparatus. The whole record is shown in (a) whilst in (b) a close up of a time section of (a) is presented which shows individual photon pulses.*

interfere with subsequent pulse searching algorithms. In Fig. 5.2(a) there are two points that will be adjusted in this way. The next routine is applied to recognise individual photon pulses in the event. The routine works by identifying the start of a pulse (pulse "dips") rather than identifying peaks. Every data point in an event is initially considered as a potential pulse dip and tested. A data point is labelled as a pulse dip if it matches one of two conditions.

- Fast dipping pulses where the pulse dip time $<$ sampling time. The data point should have decreased by at least two voltage increments (the increments are defined by the number of significant bits recorded by the TR) with respect to the previous data point, in which case a dip is recognised.

- Slow dipping pulses where the pulse dip time $>$ sampling time. At least two out of three data points decrease consecutively in which case a dip is recognised.

Both routines are necessary if all pulse dips are to be recognised. Once a dip has been recognised a new routine takes over in order to determine the "peak" of the pulse.

- A routine looks for the end of the pulse which is defined as given by a return to the

baseline or the start of the next recognised pulse dip.

- The largest amplitude within the peak range is then identified as the pulse peak.

The arrival times of the photons are measured with respect to the arrival time of the first photon. These routines were checked on approximately 50 events obtained at different temperatures and using variable TR settings and no pulse mismatch was observed.

5.4 Light yield measurements with the MPCC technique

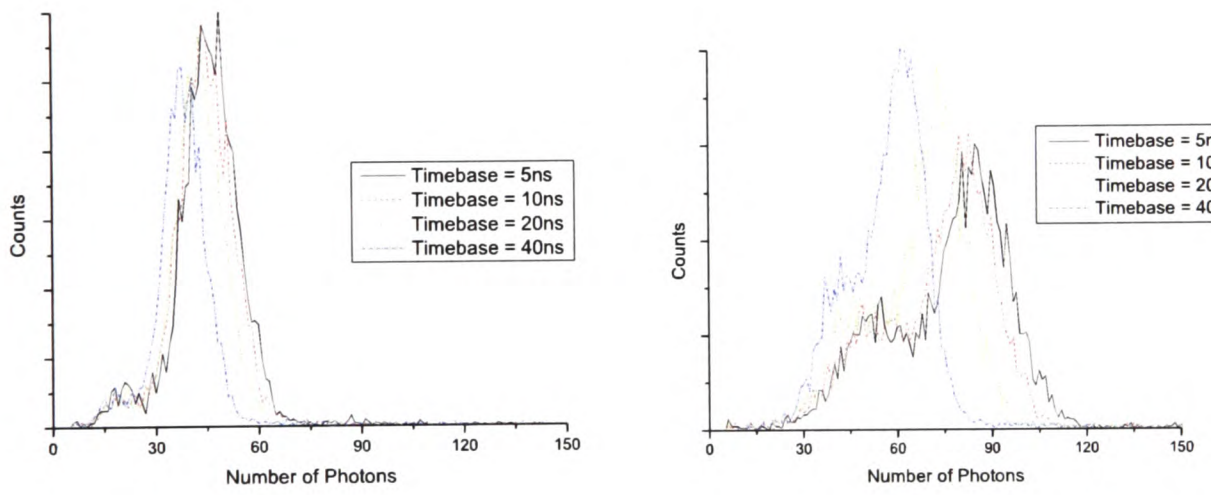

(a) (b)

Figure 5.3: *Distribution of the number of photons detected per event for different sampling times measured with γ-rays of ^{241}Am (a) and ^{57}Co (b). If the number of photons detected is independent of the sampling time, it means that the rate of photons is appropriate for photon counting. The ^{241}Am spectrum between 5 and 10ns fits this criterion, whilst no sampling time is appropriate for measurements of ^{57}Co.*

The basic condition for photon counting is that all photon pulses be separated by at least the full width of a typical photon pulse. Two photons arriving within a period of less than three samples will be counted as a single pulse, resulting in an underestimation of the number of photons. Measurements were performed to test that the rate of photons

being detected was compatible with the read-out electronics and analysis software. Keeping all other settings equal, the sampling time of the TR is varied from 5 to 40 ns. The "correct" sampling time is determined by finding the point where the number of photons counted does not change with further reductions in the sampling time. Fig. 5.3 shows this method as it was first applied using a $CaWO_4$ crystal placed on a PMT window (see chapter 8 for details of the setup). This setup has a higher light detection efficiency than the MPCC setup and more clearly illustrates how to determine the appropriate sampling time. Investigations carried out show that ^{57}Co (E=122keV) events cause the production of too many photons ($\sim$90) to allow accurate photon counting. Reducing the sampling time from 10ns to 5ns produces a significant change in the number of photons counted by the software, indicating that the sampling time is inappropriate (Fig. 5.3(b)). In other words some pulses identified as being due to one photo-electron actually stem from the pile-up of two photo-electron pulses. Events from ^{241}Am γ-rays (E=59.5keV) cause the production of approximately 50 photo-electrons. Very little change is observed between the number of counted photons when the sampling time is changed from 10ns down to 5ns, indicating that a sampling time in this range is appropriate for photon counting.

In order to determine the relative light yield of scintillators, it is not necessary to count the number of photons as the PMT can be used in integrating mode. The same software is used for recording the events, but instead of identifying and counting the pulses, the event integral is calculated by the software. The experiment can be "calibrated" using an appropriate source such that for any energy it is possible to convert the integrated result into a photon count. As an example of this, measurements of the relative light yield of $CaWO_4$ irradiated with γ-rays from ^{241}Am and ^{57}Co were carried out. The relative light yield should be compatible with measurements of the light yield non-proportionality of $CaWO_4$ performed by Moszyński et al. [84]. Fig. 5.4 shows the LY spectra obtained using γ-rays from ^{241}Am and ^{57}Co. The ratio of integrated signals for ^{241}Am compared to ^{57}Co is 47.3$\pm$0.2%. Assuming that the LY/MeV is a constant, this figure would be expected to be 48.8$\pm$0.1%. Hence it is concluded that the LY of $CaWO_4$ when irradiated by 59.5keV

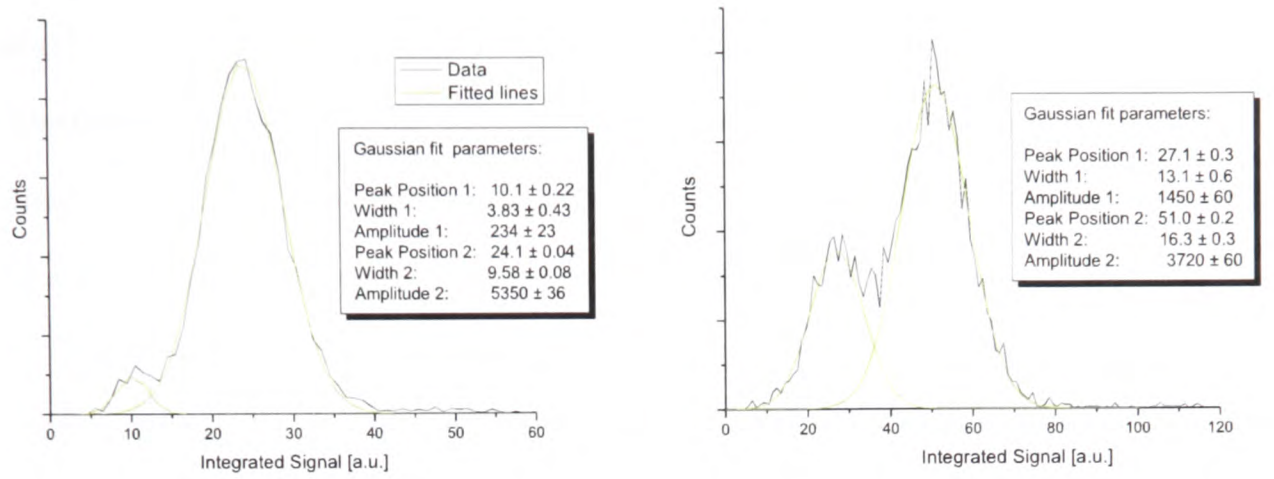

(a) (b)

Figure 5.4: *Integrated amplitude spectrum of $CaWO_4$ irradiated by ^{241}Am (a) and ^{57}Co (b). The peak for ^{241}Am is at 24.1 units and the peak for ^{57}Co is at 51.0 units. In both graphs, the radiation is accompanied by a noise pre-peak. The relative amplitude of the background and signal peak is dependent on the source position, suggesting that the background peaks are due to interactions of the radiation with surrounding matter and the collimator cover.*

gammas is 97±0.5% (47.3/48.8) of that when irradiated by 122keV gammas, in exact agreement with the results of Moszyński et al.

The MPCC setup has been tested to show that it could operate in both photon counting and integrating modes. In particular it was shown that the MPCC can be used to measure the arrival times of photons. The arrival time distribution of the photons can now be analysed in order to eliminate pre-trigger and multiple events from the dataset.

5.5 Advanced analysis and event discrimination

5.5.1 Hard cuts on pulses arriving before the trigger time

The arrival times of all photons within a record are measured relative to the first photon of the event. In some cases, records contain noise photons which have arrived before

the scintillation event takes place. Failing to remove these pre-trigger events results in a distorted spectrum of the arrival time of the photons. The trigger signal is produced when the integrated signal of the event is higher than a threshold which corresponds ~2-3 photo-electrons. The exact time range between when the first photon from an event is detected and when the trigger is produced depends on many factors including the time between pulses, the pulse heights of the photons, the decay constant and delay of the electronic integrating circuit and the light yield of the crystal. Fig. 5.5 shows the arrival

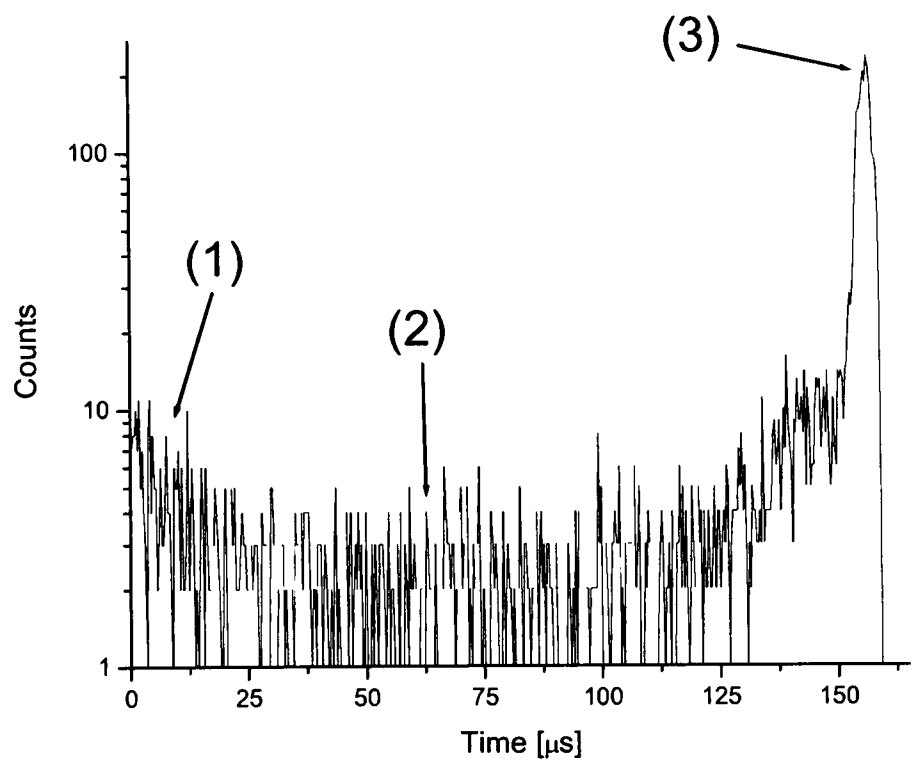

Figure 5.5: *Arrival times of the first photons in $CaMoO_4$ at 270K (1) Photons from previous events; (2) Electronic noise; (3) Correctly triggering events peak*

times of the first photons of $CaMoO_4$ events at 270K. Three features can be identified. Firstly (indicated by (1) on the figure), a small peak at close to time 0, which is due to photons from previous scintillations events "spilling" over into the next record. Depending on the decay time and the record duration, this peak can vary from being not present to being more prominent than the good trigger peak (3). Number (2) in the figure indicates the constant background noise present during a measurement due to dark counts, light

leaks and other sources of noise. Number (3) indicates the distribution of arrival times of first photons for "correct" events. Events with a first photon not in this peak are labelled as "pre-trigger" events and are cut out. The placement of each cut is determined visually, by observing where the good trigger peak becomes distinct from the background noise. A new data set is produced from which it is still necessary to eliminate multiple events. The routines for doing this are presented below.

5.5.2 Multiple event recognition

The removal of multiple events is one of the main advantages of the MPCC technique and something which single photon methods cannot achieve. When removing multiple events it is also important to ensure that no bias is created by the elimination of good events. To reach a high level of confidence that the elimination routines do not introduce bias in the experiment, a number of methods to discard multiple events have been developed and tested.

Multiple event recognition using a Shapiro-Wilks likelihood test

The first method tested is based on evaluating whether an event looks as if it is created by an exponential decay using a Shapiro-Wilks test. This method was developed by my supervisor and was extensively tested as part of the current work. In most of the HIS considered, the intensity of the slow component is much higher than that of the fast component so the arrival times distribution can be approximated to a single exponential decay. If this approximation is valid, it can be shown that if N+1 photons are detected following a scintillation event then the decay time constant τ can be calculated using equation (5.1).

$$\tau = \frac{1}{N}\sum_{i=1}^{N}\Delta t_i + \Delta t_m \frac{1}{e^{-\Delta t_m/\tau} - 1} \tag{5.1}$$

where Δt_i is the arrival time of the i^{th} photon calculated with respect to the arrival time of the first photon and Δt_m is the recording time remaining after the detection of the first photon. Assuming $\Delta t_m > 5\tau$ one can estimate that the second term in equation (5.1) contributes less than 3% to the results of calculation. With a single time constant being an approximation anyhow, the second term has been ignored, allowing us to estimate the single decay time constant as simply the mean of the photon arrival times with respect to the first photon. The algorithm used for the search and elimination of multiple events is based on the simple idea that the decay time constant calculated using equation (5.1) should be noticeably different for single and multiple events. It is also assumed that the approximation of the real decay time spectrum to a single exponential will affect the W-test much less than if the event is a multiple event. The expected decay constant ($\bar{\tau}$) is defined as the decay time which is most frequently observed in a set of measurements. A Shapiro-Wilks test is used to decide whether or not an event is caused by a single interaction. The test variable W is defined as the ratio of likelihoods of the decay time being τ calculated using equation (5.1), compared to the likelihood of the time decay being $\bar{\tau}$ [102, 108]:

$$W = 2ln\left[\frac{P(\tau|\tau)}{P(\tau|\bar{\tau})}\right] \tag{5.2}$$

$$= -2\left[ln(\frac{\tau}{\bar{\tau}}) + 1 - \frac{\tau}{\bar{\tau}}\right] \tag{5.3}$$

W represents a measure of the discrepancy between the most likely decay time constant of the process and that obtained for an individual event. When $\tau \approx \bar{\tau}$, W can be approximated by the square of the relative deviation of the time constant from the most likely time constant.

$$W = (\frac{\Delta\tau}{\bar{\tau}})^2 \tag{5.4}$$

where $\Delta\tau = \bar{\tau} - \tau$. Fig. 5.6 shows the histogram of W plotted for a large number

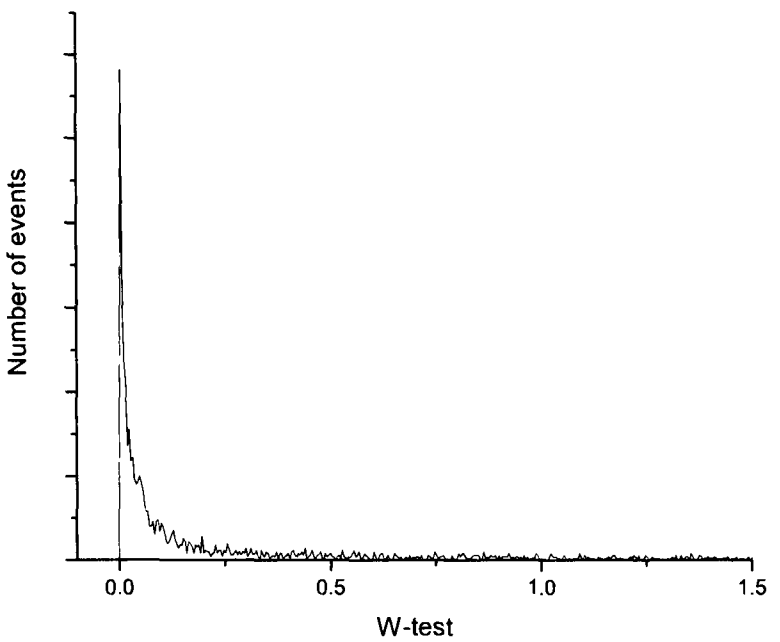

Figure 5.6: *Shapiro-Wilks test of $CaWO_4$ scintillation events compared to a single exponential decay.*

of scintillation events detected in $CaWO_4$. Studies were performed to verify how the tailing effect and time decay components were affect by the cut on the W-test. It was found that cutting in the range W = 0.05-0.5 produced no significant change on the time decay constants calculated. However as the cut-off threshold was placed higher, more tail started to appear at longer times in the records due to multiple events. The cut was thus implemented at W=0.1, close to the minimum range which leaves time decay constants unchanged. The main point of performing these cuts is to eliminate any doubt that the tail component observed in scintillation decay curves is in fact due to multiple events as opposed to a long third component. To make sure that good events are not artificially eliminated on the basis that they do not look sufficiently like a single exponential, a separate routine was developed which progressively sifts through small portions of each event to spot the start of a possible second scintillation event.

Multiple event recognition using an approximation to homogeneous Poisson statistics

When a second event occurs, the rate of photons will suddenly increase. The probability of this sudden increase in event rate can be determined using non-homogeneous Poisson statistics [109, 110]. The difference between non-homogeneous and homogeneous processes is that in the first case the average rate of events is not constant whilst in the second it is. A typical example of a non-homogeneous process is the emission of photons from a scintillation process. The reason that scintillation events are a non-homogeneous process is that once a photon is emitted, the process cannot be repeated. Hence, instead of a steady rate of photons, the observed rate of photons decreases with time. Using the approximation of a single exponential decay, scintillation processes are characterised by equation (5.5).

$$\frac{dN}{dt} = -t/\tau \tag{5.5}$$

where N is the number of photons detected between t and $t + \delta t$. N(t) is defined as the number of photons that have been detected up to time t and N_0 is defined as the total number of photons that can be detected by recording for an infinite time. Therefore at any given time, there is a quantity $N_L = N_0 - N(t)$ which corresponds to the number of photons which are yet to be detected. In the limit $\frac{N(t+\delta t)-N(t)}{N_L} \ll 1$, the number of photons yet to be emitted is approximately constant, meaning that the rate of detection of photons is approximately constant. Homogeneous Poisson statistics can therefore be used to implement a cut on multiple events by comparing the expected rate of photons with the measured rate. If a second event occurs at time t, the rate will jump in a way that would be very improbable for a single event, and the record can be eliminated. The implementation of the cut is carried out in the following way:

- The total number of photons per event N_0 is recorded

- The routine starts looping over all pulses. The time difference between each pulse i and $i-1$ is recorded as $\delta t(i) = t_i - t_{i-1}$.

- The time taken for another m pulses to arrive is recorded as t_{i+m}. For each event, m is determined by requiring the ratio m/N_0 to be a constant. m/N_0 is user defined, but to make the Poisson approximation valid requires $m/N_0 << 1$.

- The rate of pulses Γ when the i^{th} pulse is recorded is given by the average rate over next m pulses: $\Gamma(i) = \frac{m}{t_{i+m}-t_i}$

By the definitions above, only one pulse has been observed in time δt. If N_0 is sufficiently large, the rate of pulses is approximately constant between $i-1$ and i and the expected number of photons in time δt is given by $\mu(i) = \Gamma(i)\delta t(i)$. The probability of observing only 1 photon in δt is given by Poisson statistics:

$$P(i) = \mu(i)e^{-\mu(i)} \tag{5.6}$$

The routine loops over all the pulses, looking for any unlikely increases in the pulse rate, characterised by a low probability P(i). To determine if a multiple event has been recorded, the lowest probability P_{min} for all pulses of the event is recorded. If $P_{min} < P_{cutoff}$ then the event is rejected as a multiple event. How to choose the cutoff probability is discussed later in this chapter.

Studies on the validity of using the homogeneous Poisson approximation

The validity of the cut is evaluated by comparing its performance to a cut based on non-homogeneous Poisson statistics on scintillation events with decay time τ. Let us consider the general case of a photon i arriving at time t=T. We define the quantity δT as the time difference between T and the arrival time of photon $i-1$. We also define the quantity ΔT which is the time taken to see "m" photons starting from time T. The expression for

calculating the expected number of events μ in the time interval ΔT is:

$$\mu = \int_{T}^{T+\Delta T} \lambda(t)dt \tag{5.7}$$

where $\lambda(t)$ is the time dependent rate of observation of photons. In the case of scintillation decays, $\lambda(t) = \frac{e^{-t/\tau}}{\tau}$ (single exponential approximation) one obtains the expected number of photons (μ_n) for a non-homogeneous distribution in the interval T to T-δt:

$$\mu_n = N_0 e^{-T/\tau}(e^{\delta T/\tau} - 1) \tag{5.8}$$

where N_0 is the total number of photons seen in a single event. Equation (5.8) can be rearranged to find the expected time to see μ_n photons:

$$\Delta T = -\tau ln(1 - \frac{\mu_n}{N_0} e^{T/\tau}) \tag{5.9}$$

By setting μ_n=m, equation (5.9) can be reinterpreted as being an estimate of the expected value of ΔT given τ.

For the homogeneous approximation, let us assume that m<< N_0, and that hence the rate of detection of photons is nearly constant. The time (ΔT) taken for "m" photons to be detected starting from T gives the rate λ as shown in equation (5.10).

$$\lambda = m/\Delta T \tag{5.10}$$

The expected number of photons μ_H in time δT using the homogeneous approximation is now simply given by $\mu_H = \lambda\delta$T. Substituting for the reference value of ΔT from equation (5.9) yields the expected number of events between time T and T-δT for the homogeneous

approximation (as opposed to the assumed value m):

$$\mu_H = \frac{-m}{ln(1 - \frac{m}{N_0}e^{T/\tau})}\frac{\delta T}{\tau} \tag{5.11}$$

Using equation (5.6), it is possible to compare the probability of seeing only 1 event in time δT calculated using the expected rates from equations (5.8) and (5.11). The prob-

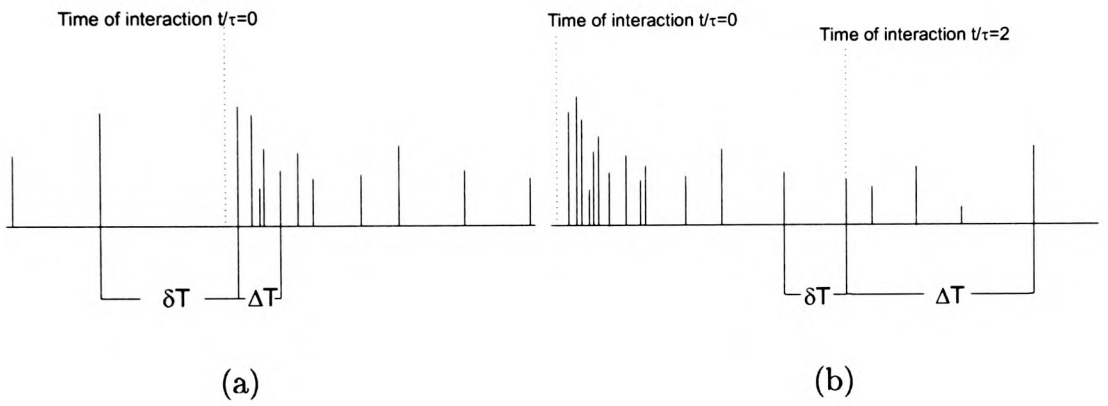

Figure 5.7: *(a) Pulse i is detected early in an event (b) Pulse i arrives late in the event.*

abilities depend on the arrival time of a photon compared to the start of its scintillation event. Fig. 5.7(a) shows the case where i is the first detected early in an event, i.e. it arrives close to t/τ=0. Fig. 5.7(b) shows the case when i arrives late in an event, at t/τ=2 for example. Figs. 5.8(a) and (b) shows the probability of seeing one event in time $\frac{\delta T}{\tau}$ for when photon i has arrived early and late in an event. In Fig. 5.8(a), the cuts on δt/τ resulting from a value of P_{min} >0.1 are indicated by the shaded zones. In the non-homogeneous case this corresponds to a cutoff value of δt/τ >0.07. In the homogeneous approximation case, this corresponds to a cutoff value of δt/τ >0.095. In other words the cuts made using the homogeneous approximation are conservative. Setting P_{min}=0.005 will result all events that have $\frac{\delta T}{\tau}$ >0.25 being cut out.

The comparison between the predictions using homogeneous and non-homogeneous distributions becomes much worse "late" into the event. The homogeneous approximation performs very badly at cutting out events when considering pulses "late" in an event. The reason for the degradation in the cut performance is that as T/τ increases, the number

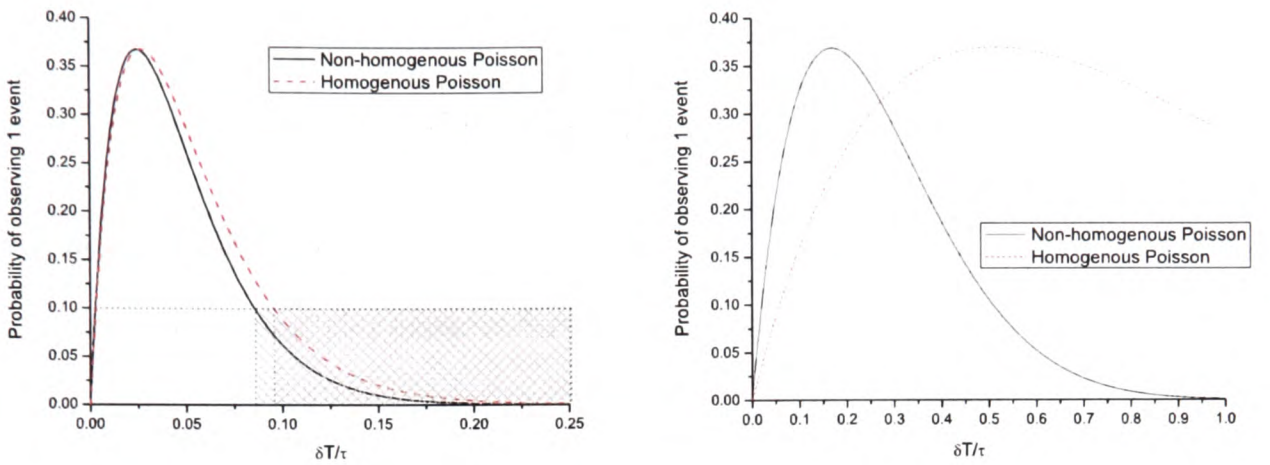

Figure 5.8: *Probability of only one event occurring in time $\delta T/\tau$ calculated using homogeneous and non-homogeneous Poisson statistics for m=5, N_0=40 and (a) T/τ=0 and (b) T/τ=2. The shaded area in (a) represents the cut on $\delta t/\tau$ arising from a cutoff value $P_{min} > 0.1$*

"potential pulses" decreases and $\frac{\Delta N}{N_L} \rightarrow 1$. Hence the homogeneous Poisson approximation is no longer valid. In practice, it means that the Poisson cut works well if a second event has been recorded, but it is very bad at cutting single events. The breakdown of the homogeneous approximation late in single events is therefore an advantage for the cut. In summary, the cut can be expected to perform very well to eliminate multiple events in scintillators that have a single exponential decay. To test the performance of the cut on scintillation events that have a double exponential structure, a MC event generator was designed.

5.6 Test of multiple event rejection using a MC event generator

The aim of the MC is to generate records that resemble the records obtained from scintillation events of HIS such as $CaWO_4$. The logical flow of the MC event generator is

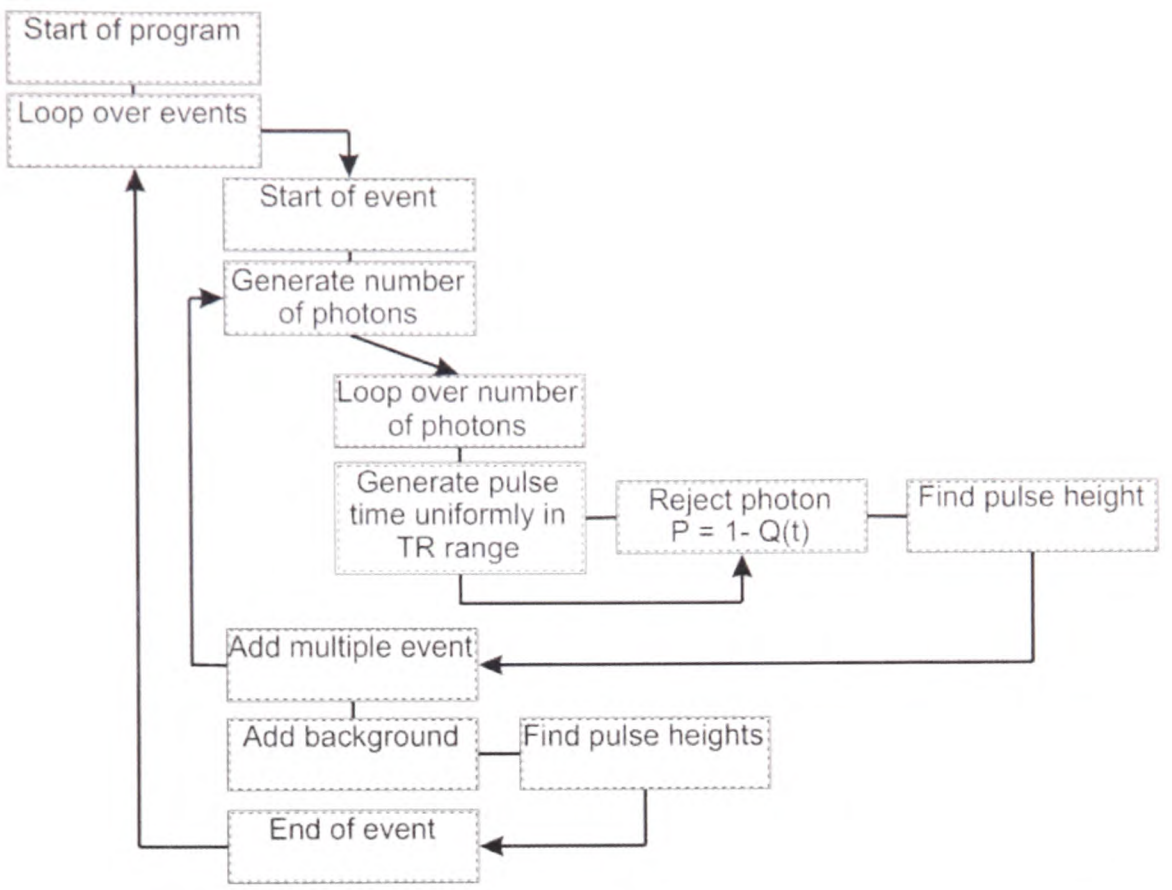

Figure 5.9: *Flow of processes used in order to generate scintillation events using the MC*

shown in Fig. 5.9. The number of photons for each event is obtained by sampling a Gaussian distribution with a user defined mean and width. The program then starts a loop to determine the arrival times of the individual photons, using the acceptance-rejection method with a double exponential decay distribution. Photons are generated uniformly in time and rejected with a probability P(t) = (1-Q(t)) where Q(t) is the normalised probability distribution. If a photon time is rejected the program looks for a new photon time until the time is not rejected. When the time of the photon is fixed, the amplitude of the pulse it creates is generated. The pulse amplitude distribution is approximated to a Gaussian. Each pulse decays with a decay constant of 15ns corresponding to the observed characteristics of the experimental pulses.

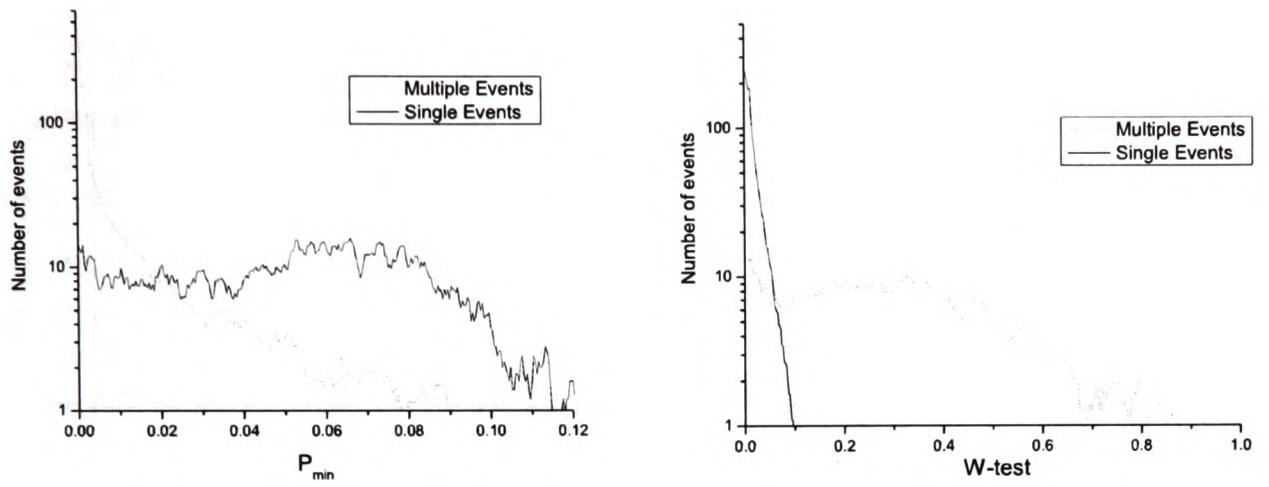

(a) (b)

Figure 5.10: *(a) Poisson approximation P_{min} and (b) Shapiro-Wilks Test distributions for 5000 single (solid line) and multiple events (dashed line)*

5.6.1 Comparison of the performance of the cuts

The results presented here are for events generated using decay characteristics close to what is expected for $CaWO_4$ events at low temperatures (see table 5.1) and using the recording properties of the TR8828 transient digitiser. Similar results were obtained for any simulated decay characteristics generated using the MC. Fig. 5.10(a) shows the discriminating power of the Poisson cut and Fig. 5.10(b) shows the discriminating power of the Shapiro-Wilks cut. It is not possible to find a Poisson cut which eliminates all multiple events. A cut at P_{min} >0.005 ensures that most multiple events are eliminated but at the price of eliminating a significant proportion of good events. By carrying out the cuts on a record containing only good events, it was observed that the calculated decay times were not affected by the elimination of these good events. In fact it is possible to cut quite freely on P_{min} without having an adverse consequence on the determination of the correct time constants. Looking at the Shapiro-Wilks test, a W-cut at W<0.1 ensures that all good events are kept with a small proportion of multiple events let though. Overall, table 5.1 shows that both cuts perform equivalently when the resulting photon

time distribution is fitted and compared to the MC input decay times. By carrying out the cuts on a record containing only good events, it was observed that the elimination of good events due to a too severe cut on the W-test affects the determination of the time constants more than compared to the Poisson approximation method.

As can be seen, both cuts lead to a worsening of the estimation of the decay charac-

Table 5.1: *Effect of cuts on the determination of the decay time. The performance of the cuts is evaluated for liquid helium temperature (LHeT) like events.*

Cut	τ_S	τ_L	A_S/A_L
MC	4	400	2.0
None	3.93±0.1	412±10	2.5
W<0.1	3.64±0.1	470±10	2.1
P_{min}>0.005	3.80±0.1	466±10	2.3
Complete	3.80±0.1	395±10	2.1

teristics. The reason for this is that both the Poisson and Shapiro-Wilks method do not cut uniformly on the time of arrival of the second or multiple event. Studies carried out have shown that both methods are unable to recognise a second event arriving close to the start of the first event or very late in the record time. The best cut can be achieved by introducing an additional cut on the total number of photons. A fitting routine is included to recognise the peak in number of photons which corresponds to the average number of photons produced by one scintillation event. A cut of 4σ around the peak is implemented. This eliminates multiple events nearly uniformly in time, except for pulses arriving very late in the record. A second event occurring late in the record will not have all its photons detected, and hence the cut is less effective. Similarly, multiple events due to low energy cosmic rays are also not removed by the N cut. This is why the best estimation of the decay parameters is obtained using a combination of the N cut, with weak Shapiro-Wilks (W<0.5) and Poisson cuts ($P_{min} > 1x10^{-6}$). The combination of cuts is referred to as "complete" in table 5.1. As can be seen the cuts reproduce nearly all the parameters exactly, including the ratio of amplitudes of both components which cannot be obtained without cuts.

The MC studies show that the proportion of good events eliminated using the "complete" cut is small, the exact figure depends on the decay times, total number of photons and background levels introduced in the MC. However there remains some contention as to whether or not decays involving three or more components would be removed by this cut. Both the Poisson based cut and the Shapiro-Wilks method assume that the decay time distribution can be approximated to a single exponential. It is of particular interest to verify that these simplifications do not eliminate slow components from being considered. In particular, these studies were motivated by an uncertainty on the true decay characteristics of $CaWO_4$ [84]. MC simulations were run to produce events characterised by a sum of three exponential decays. It was found that none of the cuts above eliminate events in a proportion higher than for events which are described by a two exponential decay. This provides great confidence that the shape of the decay time curve after the cuts will be the true characteristic decay curve of the crystal measured in the system.

5.7 Conclusions

The MPCC technique was developed in order to measure the scintillation decay times of heavy inorganic scintillators in the approximate range of 5-600μs. The technique is based on recording all photo-electron pulses produced by a PMT due to a scintillation event. Software routines recognise the recorded pulses and histogram the time arrival distribution of the photons detected as well as the total number of photons seen per event. The operating range of the photon counting has been verified and it was also confirmed that the MPCC can be used in integrated mode to obtain the relative light yield of different scintillators. Routines were implemented in order to ensure that the photon arrival time spectrum was not distorted due to a misidentification of the start of the scintillation event. One of the main advantages of the MPCC technique is its ability

to eliminate contributions due to multiple interaction events using offline cuts. The best cut obtained was using a combination of a cut on the number of photons, a Shapiro-Wilks likelihood cut and a homogeneous Poisson approximation cut. The cuts were tested using a MC event generator which reproduces the main features of a scintillation decay. It was shown that the cuts allow for a precise calculation of the decay times used as input for the MC generator. It was also shown that the cuts do not eliminate events that may contain a slow component which was one of the main aims of these studies. These tests of the MPCC hardware/software combination provide great confidence that measurements of the light yield and time decay of HIS can be performed in this way. Results of investigations using the MPCC, along with results from luminescence measurements are presented in the next chapter.

Chapter 6

Scintillation properties of CPSD materials

In the previous two chapters, a number of tools were described for examining the scintillation properties of prospective CPSD materials. The SuperLumi and MoLeS facilities are designed to gather spectroscopic information and the MPCC technique is used to measure the time decay characteristics and relative light yields. Used together, these techniques produce a comprehensive characterisation of scintillation properties of materials. Equipped with the necessary tools it is now possible to consider various scintillators and evaluate their worth as potential CPSD. The following chapter presents the results obtained when using these three techniques on a range of potential CPSD materials.

6.1 Requirements for rare-event search CPSD

A short consideration of what makes a good scintillator quickly leads to the conclusion that the most important property is a high light yield (LY). Ever since the first scintillator was discovered, which incidentally was $CaWO_4$ in 1895 [111], physicists and materials scientists have looked to increase the amount of light extracted from luminescent materials. CRESST has a different priority which is that scintillators for use as CPSD in low background experiments must be radiation free. This mostly excludes the possibility

of using activator ions to increase the light yield of the scintillators. Such dopants tend to contain high amounts of radioactive isotopes and hence are unsuitable for CRESST. Similarly, the requirement for low radioactive contamination imposes strict restrictions on the materials which can be used to grow crystals. There are further constraints for CPSD materials which are not usually taken into account in mainstream scintillator development. Firstly, the scintillators must be able to operate at very low temperatures. The current technology of tungsten film deposition for the phonon detector requires that the crystals must have a high melting point ($\gtrsim$1300^{o}C). The crystals must have good phonon properties which means that the growth process will have to produce large homogeneous crystals which is not possible for all scintillating materials. The crystals also need to have a low heat capacity in order to have good heat collection properties. In order to maximise the chance of an interaction with a WIMP, the crystals need to have high density and a high atomic mass of constituent elements. One advantage however is that CRESST and other rare event searches do not require fast scintillators. A limit on the decay time is imposed by the signal to noise ratio (a long decay time means the amplitude of the signal is reduced, hence reducing the signal to noise ratio). Faster decaying scintillator signals are thus desirable but not strictly necessary. Given the above restrictions, a number of materials have been investigated as potential CPSD scintillators. This section presents the results of luminescence and decay time studies carried out on $CaWO_4$, $ZnWO_4$, $CaMoO_4$, $CdMoO_4$, $MgMoO_4$, Al_2O_3:Ti, CaF_2 and MgF_2. The results in this section are presented by crystal families, i.e. tungstates, molybdates, fluorides and Al_2O_3.

6.2 Results

The molybdate and tungstate samples are grown by the Czochralskii technique from raw materials having 99.99% (4N) purity for tungstates and 99.95% for molybdates. The Ti-doped Al_2O_3 is a commercial sample of scintillation quality and is doped with 0.07% Ti. The purity of the fluorides is not known but investigations have shown that they

contain less contamination than other nominally pure samples provided by recognised scintillating crystal manufacturers. All samples for measurements were of size 5x5x1mm^3 and were polished to optical quality. The main results for each crystal are the temperature dependence of the emission spectra and the consequent assignment of emission bands in combination with identification of the excitation peaks.

6.2.1 $CaWO_4$

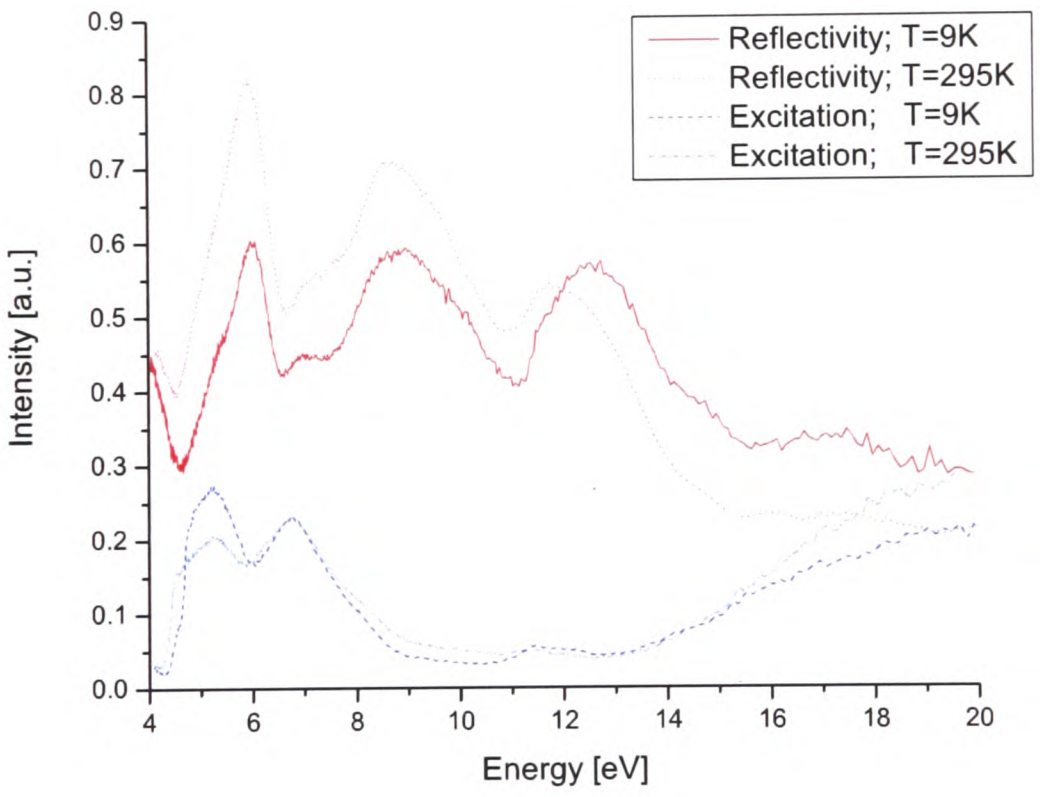

Figure 6.1: *The excitation and reflection spectrum of $CaWO_4$ under VUV excitation at room and liquid helium temperatures*

Fig. 6.1 shows the excitation and reflectivity spectrum of $CaWO_4$ in the range 4-20eV for emission of energy 2.9eV (430nm). Two main features can be identified. The sharp onset in the excitation spectrum (matched by a decrease in reflectivity) at ~4.5eV marks the minimum excitation energy required in order to obtain intrinsic luminescence [112]. The rise in the luminescence intensity seen above 13eV in $CaWO_4$ is associated with the

beginning of the multiplication of electronic excitations [113]. Fig. 6.2 shows the emission

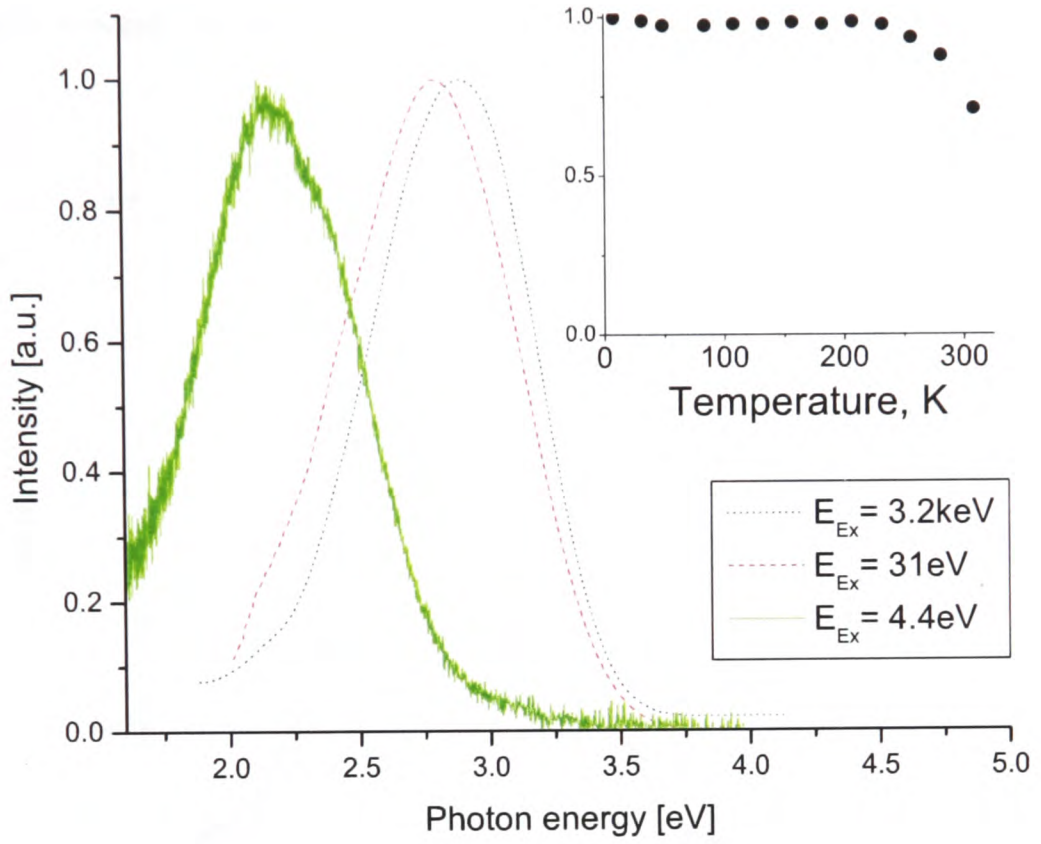

Figure 6.2: *Luminescence spectra of $CaWO_4$ under different excitation conditions. The spectra are normalised to all have a maximum intensity of 1.0. The curve corresponding to E_{ex}=4.4eV is of significantly lower intensity, hence the increased visibility of noise fluctuations.*

spectrum of $CaWO_4$ for different excitation energies. At E_{ex} >1keV (the range of interest for CRESST) $CaWO_4$ exhibits a single broad band emission centred at approximately 2.9eV. This band is due to transitions in the WO_4^{2-} anion complex and is interpreted as emission from the radiative decay of self-trapped molecular excitons [112, 114, 115]. This is assigned to the transition from the $^3T_{1,2}$ levels (triplet state) to the $^1A_1$ level (ground singlet state). This emission band is usually referred to as the intrinsic emission band which means that all $CaWO_4$ crystals will usually emit in this band. The inset shows the temperature variation of the intensity of this band. The quenching temperature (T_q) of the band is greater than can be measured using any of the experimental apparatus (>300K). At energies E_{ex} <4.5eV the emission is one green band centred at 2.1eV. This is attributed

to extrinsic emission from oxygen deficient sites (WO_3 Schottky defects) [112, 116, 117]. The relative intensity of this band is sample dependent and it is expected to disappear in a perfectly pure crystal. In order to further understand how the luminescence depends on

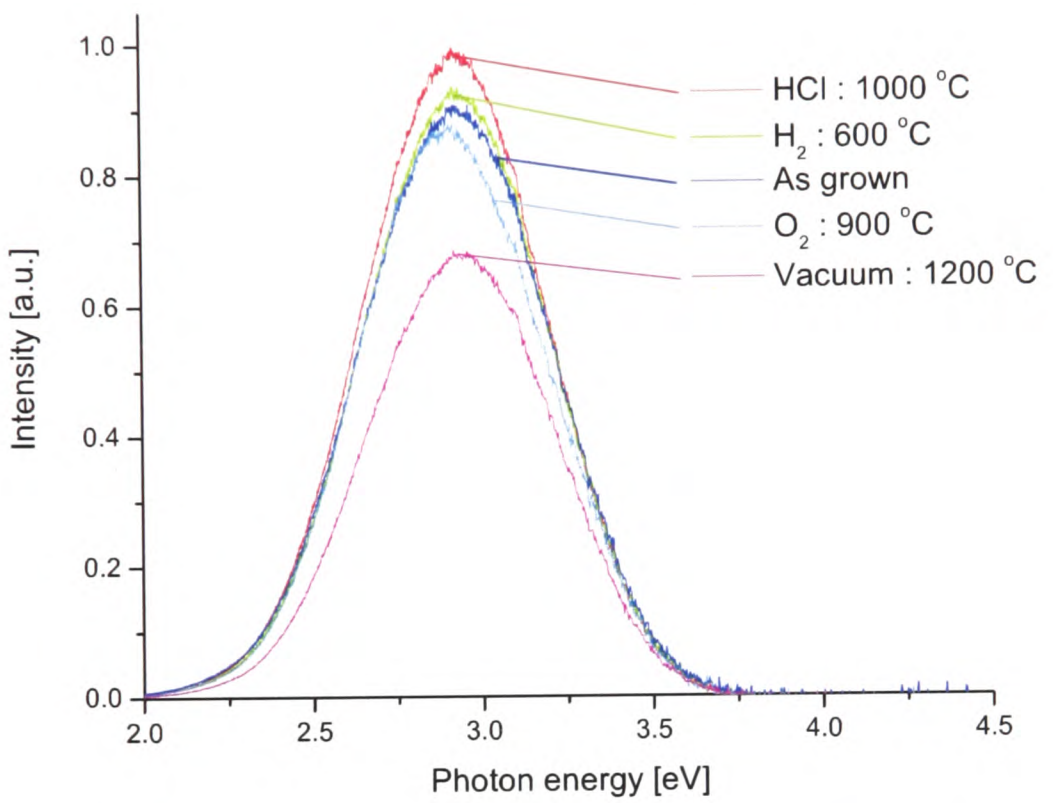

Figure 6.3: *Effects of post growth treatment on the luminescence properties of $CaWO_4$*

the quality of the sample, the luminescence of $CaWO_4$ crystals produced using different annealing conditions has been investigated. A $CaWO_4$ ingot was produced from raw material of 4N or better purity by SRC "Carat" (Lviv, Ukraine). The producer then cut six crystals from this ingot, annealed them in different conditions and then polished them to the same specifications. Fig. 6.3 shows how the luminescence of these crystals varies with annealing conditions. Annealing at 1000°C in either HCl or nitrogen results in crystals with a higher light yield, in line with previous observations [118]. It is very encouraging that a crystal which has already been selected due to its good light properties can have its light yield increased further by annealing.

Since $CaWO_4$ is used as a CPSD detector, it is also interesting to try and find out as

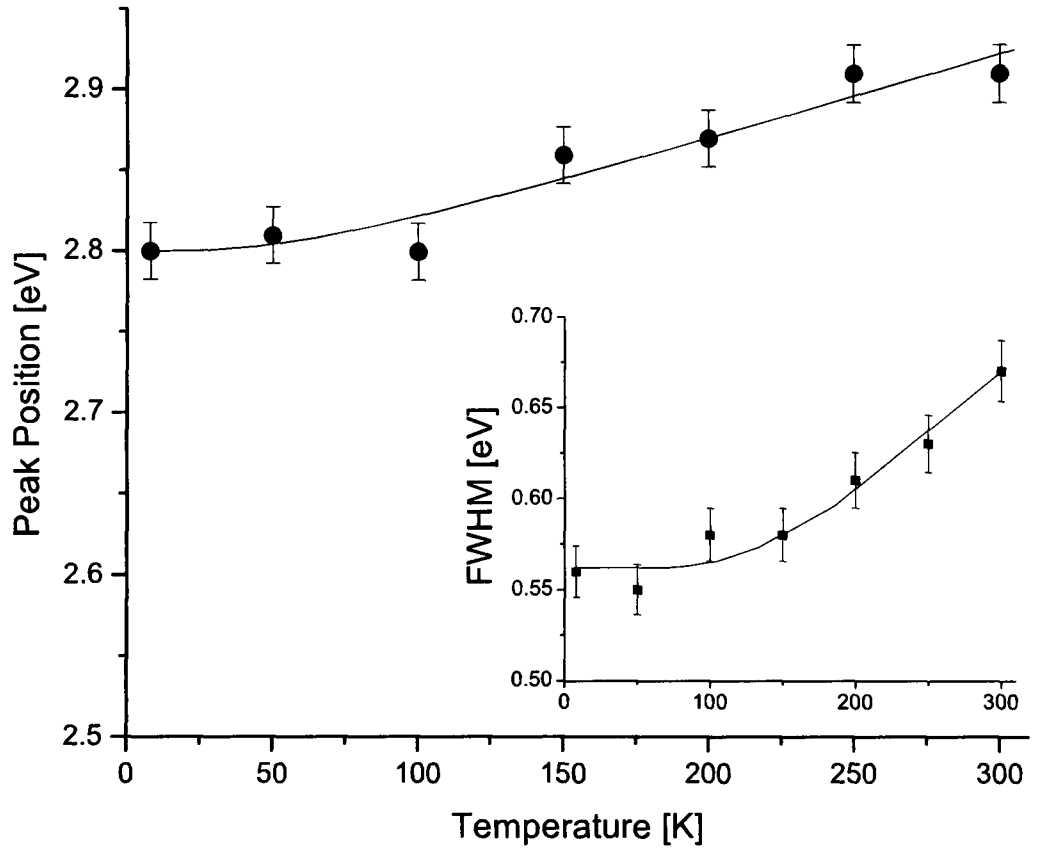

Figure 6.4: *Temperature dependence of the peak and width of the intrinsic emission band of* $CaWO_4$

much as possible about its phonon properties. As discussed in chapter 4, the lattice vibration energy and the phonon cutoff energy can be obtained by examining the temperature dependence of the luminescence peak width and energy respectively. Fig. 6.4 shows the temperature dependence of the peak position under excitation from 6.2eV photons. Fitting of equation (4.8) to the experimental data was performed using the minimisation by gradient method (MIGRAD algorithm) [119]. The Boltzmann distribution was numerically integrated using an extended version of the trapezoidal rule [120]. The best fits (solid line) were obtained with values of the phonon cut-off energy ($\hbar\omega_D$) of 26 ± 9 meV. This value is consistent with the value for the cut-off phonon energy of 22meV found in the literature and obtained from measurements of the elastic constant of $CaWO_4$ [121]. The inset shows the temperature dependence of the width of the intrinsic peak. The fit to equation (4.7) gives a phonon energy of 45±3meV which is consistent with the ν_2-internal vibration mode of WO_4 tetrahedrons in $CaWO_4$ (44 meV) [122].

As suggested in previous chapters, the temperature variation of the time decay characteristics of $CaWO_4$ were investigated using the MPCC technique. Fig. 6.5 shows the photon arrival time distribution at 8 and 350K. Fitting to two exponentials at room temperature yields decay constants of τ_S=1.3±0.1μs and τ_L=8.9±0.2μs which is in good agreement with results recently reported [123]. The data presented are the first experimental test of the MPCC technique. In the range ~50-150μs, a relatively high backround count is observed compared to later on in the event. This is due to the uneven elimination of low energy events; for example if a low energy cosmic interaction occurs shortly after a source interaction (or vice-versa), none of the cuts will eliminate the event, leading to an uneven background level.

Fig. 6.6 shows how the decay times vary with temperature. At T<50K, τ_L increases very sharply to become 405±20μs at 9 K. As previously discussed, this is expected given the existence of a metastable level a few meV below the emitting level. The scintillation decay time constant of $CaWO_4$ at millikelvin temperatures is reported to be 400±100μs with which the current measurements are in good agreement [124].

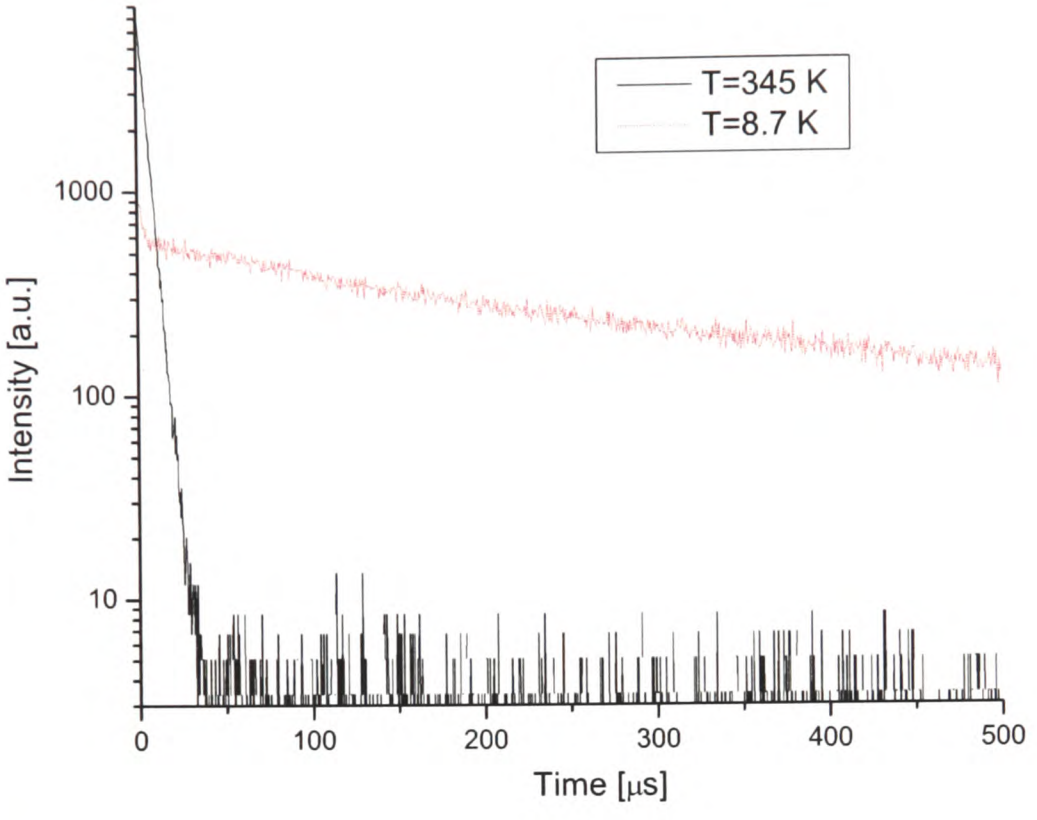

Figure 6.5: *Decay spectra of $CaWO_4$ at room and liquid helium temperatures*

6.2.2 $ZnWO_4$

Zinc tungstate is a commercially available scintillator which suits the strict restrictions that rare events searches place on the radio-purity of samples. As an example, the purity of the sample of $ZnWO_4$ used was measured to be ~1 ppm of Cr and ~0.1 ppm of Ba while the content of other metal impurities (35 in total) was below the detection limit of 0.02 ppm [47]. Fig. 6.7 shows the reflectivity and excitation spectrum of $ZnWO_4$ taken at peak emission (2.45eV). The main features of the reflection spectrum match closely that which were calculated for wolframites allowing the assignation of the bands to properties of the intrinsic radiation [125, 126]. As for $CaWO_4$, the rise in the excitation efficiency seen above 11 eV in $ZnWO_4$ is associated with the beginning of the multiplication of electronic excitation. Fig. 6.8 shows the luminescence spectrum at 9K at excitations of 31eV and 3.2eV. The luminescence spectra are the same across the whole excitation spectrum with a range from 1.8 to 3.0eV and a peak at 2.45eV. This emission is associated with the radia-

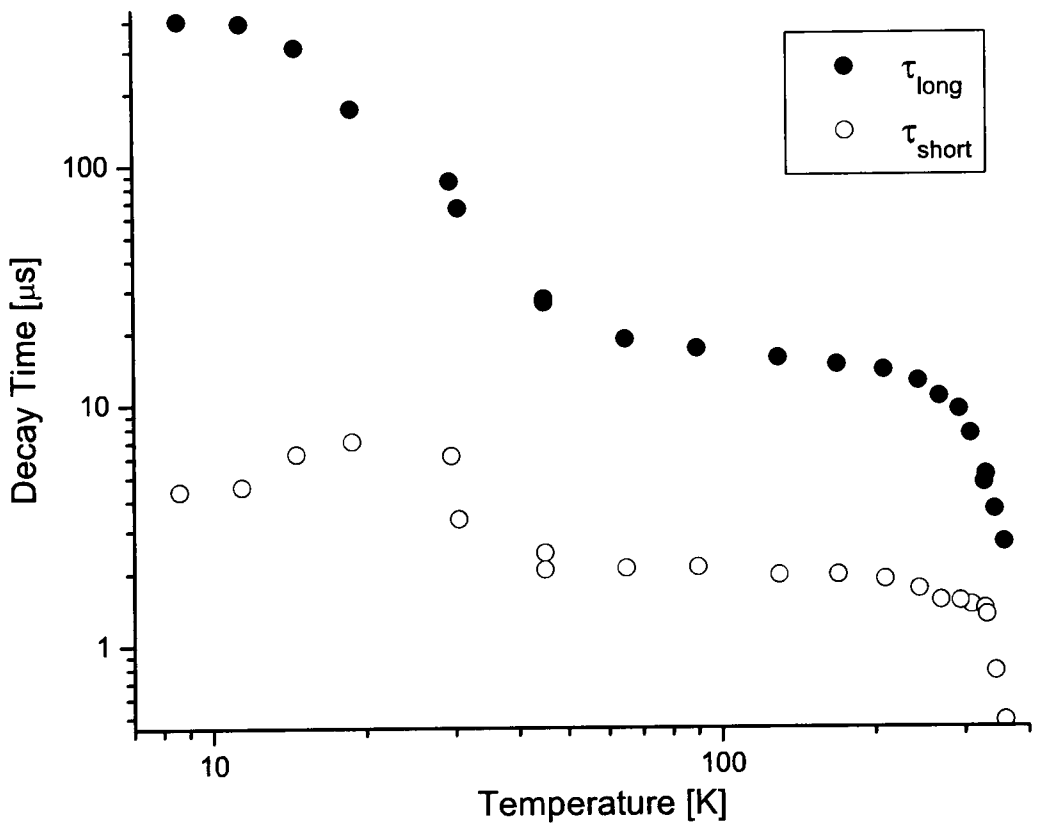

Figure 6.6: *Temperature dependence of the two decay time components of* $CaWO_4$.

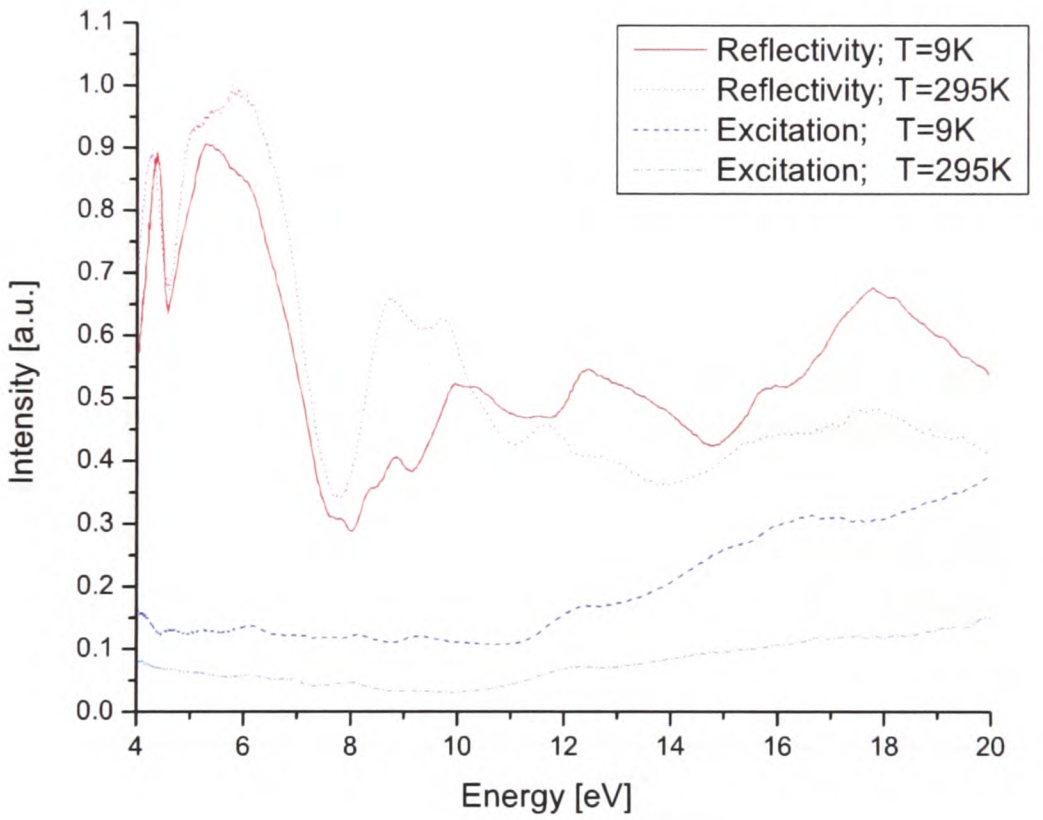

Figure 6.7: *The excitation (solid) and reflection (dash) spectrum of $ZnWO_4$ under VUV excitation;*

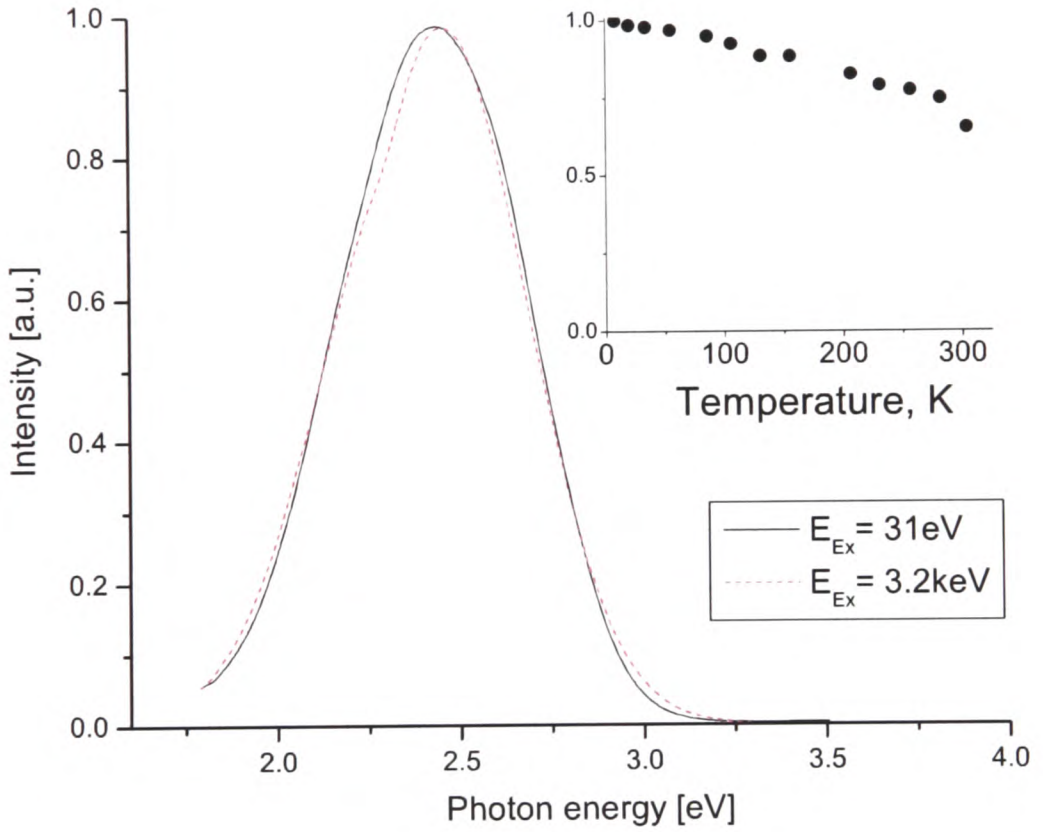

Figure 6.8: *The luminescence spectrum of $ZnWO_4$ under VUV excitation;*

tive transitions between tungsten and oxygen within the WO_6^{6-} molecular complex [127] typical of wolframite tungstates. The temperature dependence of the luminescence of $ZnWO_4$ is shown in the inset and follows a trend similar to $CaWO_4$, i.e. luminescence increases as temperature decreases. Once again the quenching temperature is too high to measure, T_q >300K. It is worth noting that the light output of $ZnWO_4$ at T= 9 K and 3.2 keV excitation is ~10% higher than that of $CaWO_4$. At E_{Ex}=320eV excitation energy the ratio for the light yield is 1.15±0.1. These results provide a strong indication that the intrinsic light yield of $ZnWO_4$ at low temperature is higher than that of $CaWO_4$ making $ZnWO_4$ a strong candidate for the next materials to be used as CPSD. In fact as a result of these studies, $ZnWO_4$ is now being tested as a CPSD [47]. Fig. 6.9 shows

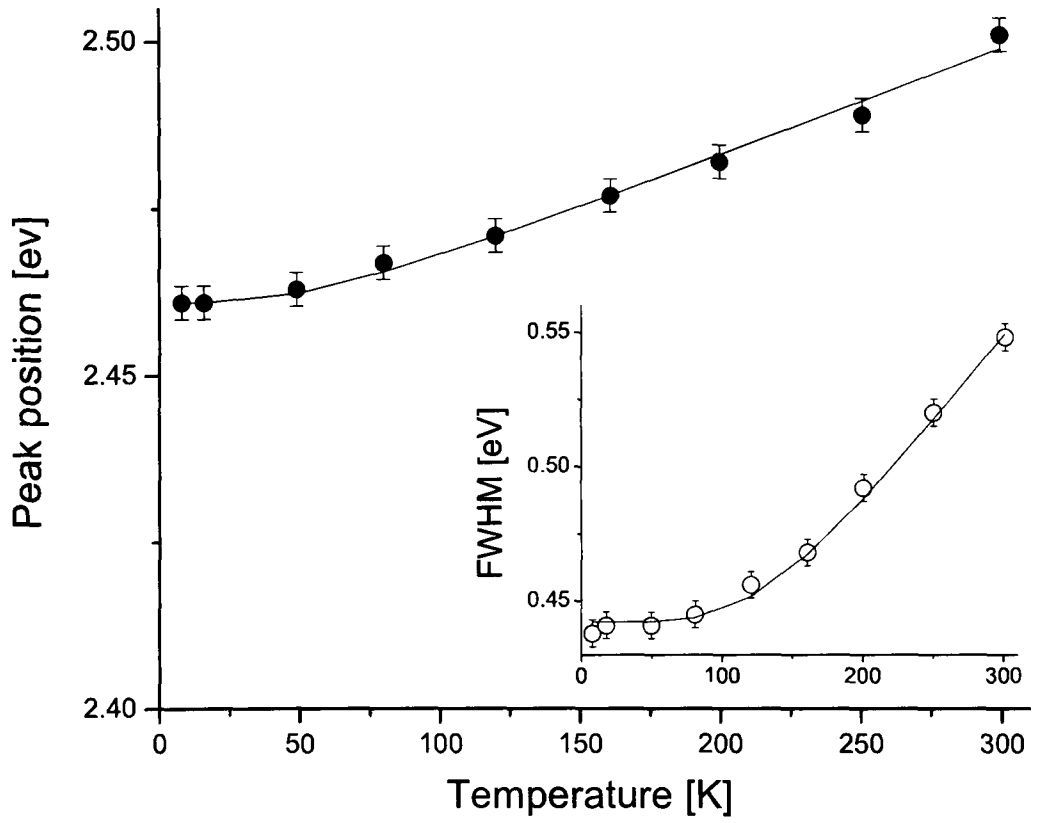

Figure 6.9: *Temperature dependence of the peak and width of the intrinsic emission band of $ZnWO_4$*

the temperature dependence of the luminescence peak position, and the inset shows the evolution of the width of this peak (E_{ex} = 31eV). Fitting as for $CaWO_4$ yields a phonon

cut-off energy of 17±6meV in agreement with the previously reported value of 16±2 [128]. Fitting the temperature dependence of the half-width of the intrinsic emission band to the canonical co-tangential formula yields a value of 40.5±0.5meV for the characteristic phonon energy. Equation (6.1) shows the inverse cube relation between the specific heat and the Debye cutoff energy ω_D.

$$C \propto \frac{T^3}{\omega_D^3} \tag{6.1}$$

where T is the temperature. This means that $ZnWO_4$ has a lower specific heat than $CaWO_4$, yet another advantage of using $ZnWO_4$ as a CPSD. Further support for the se-

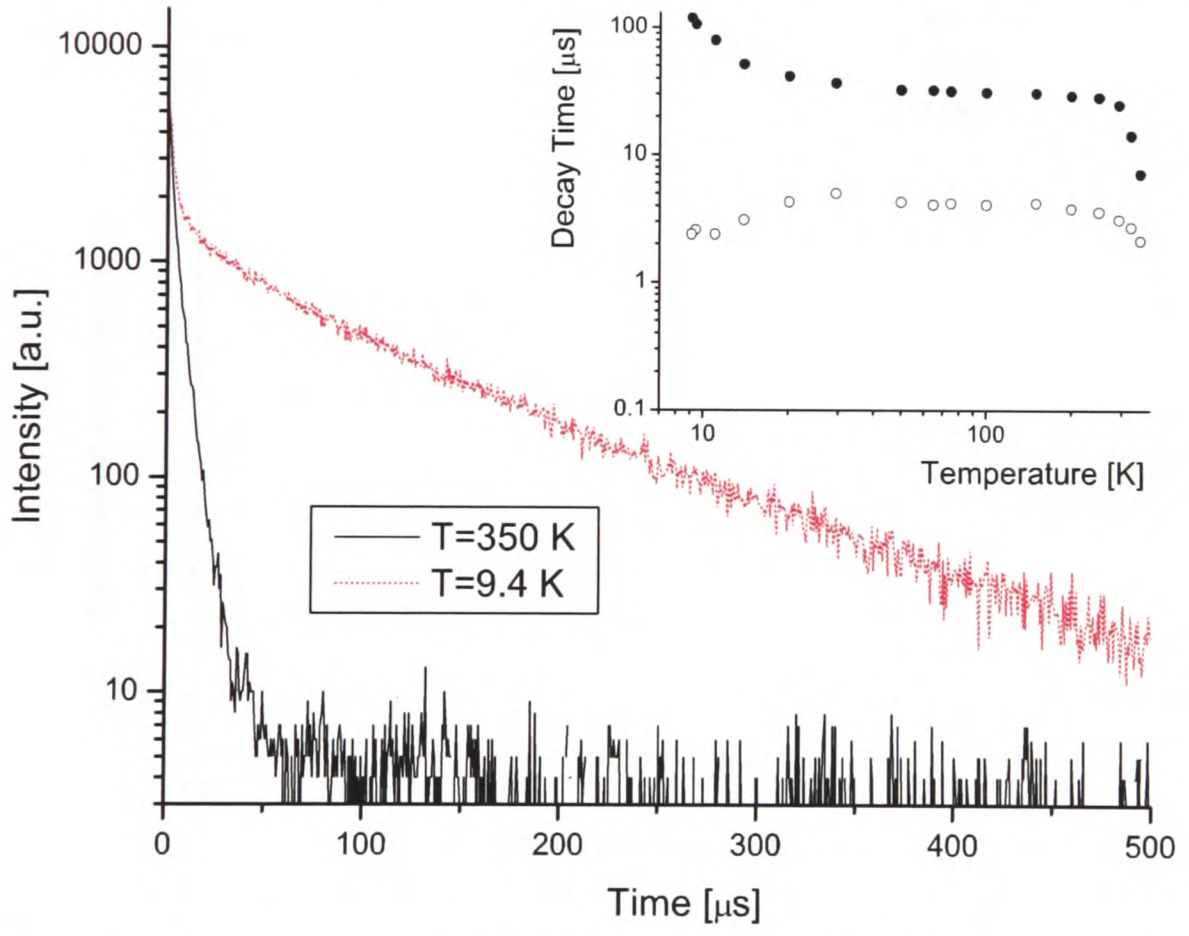

Figure 6.10: *Time decay spectrum of $ZnWO_4$ at room and liquid helium temperatures.*

lection of $ZnWO_4$ comes from the time decay characteristics at low temperatures. Fig. 6.10 shows the decay spectrum of $ZnWO_4$ measured at different temperatures. As for the time decay spectrum of $CaWO_4$, an increased background rate due to non-eliminated low energy multiple events is visible in the range ~50-150μs. The decay constant becomes longer

as temperature decreases but this happens more gradually than for $CaWO_4$. At 9K the long decay time constant of $ZnWO_4$ is 110±15μs and it is reported to go up to ~200μs at millikelvin temperatures [129]. This is still twice as short as $CaWO_4$. This means that for an equal amount of energy converted to photons, the amplitude of a pulse from a $ZnWO_4$ CPSD will be larger than for a $CaWO_4$ CPSD, resulting in a better chance of seperating low energy pulses from background noise.

6.2.3 $CaMoO_4$, $CdMoO_4$ and $MgMoO_4$

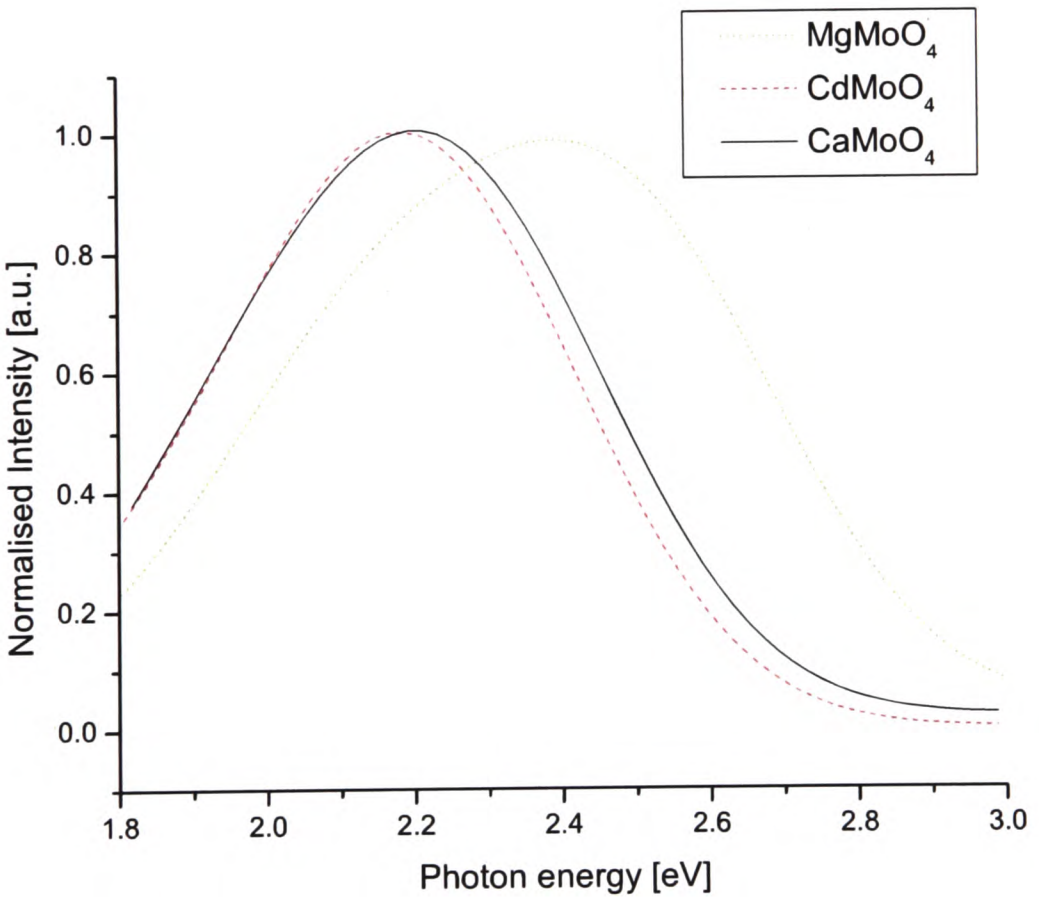

Figure 6.11: *The emission spectrum of $CaMoO_4$, $CdMoO_4$ and $MgMoO_4$*

The molybdate family, much like the tungstate family, are scintillating materials which are able to meet all the requirements imposed by rare event searches. Furthermore, $CaMoO_4$ is an ideal complimentary material to $CaWO_4$ when trying to exploit the material signature of a WIMP signal, a key property for new scintillators for CPSD. Another interesting

property of molybdates is that ^{100}Mo is considered as one of the most promising isotopes for the detection of double beta decays. Fig. 6.11 shows the luminescence spectra of the crystals measured using monochromatic X-ray excitation (3.2 keV). At low temperatures, molybdate crystals exhibit broad band luminescence with maxima at 2.4 ($MgMoO_4$), 2.2 ($CaMoO_4$) and 2.15eV ($CdMoO_4$). Of these crystals only $CaMoO_4$ has an appreciable

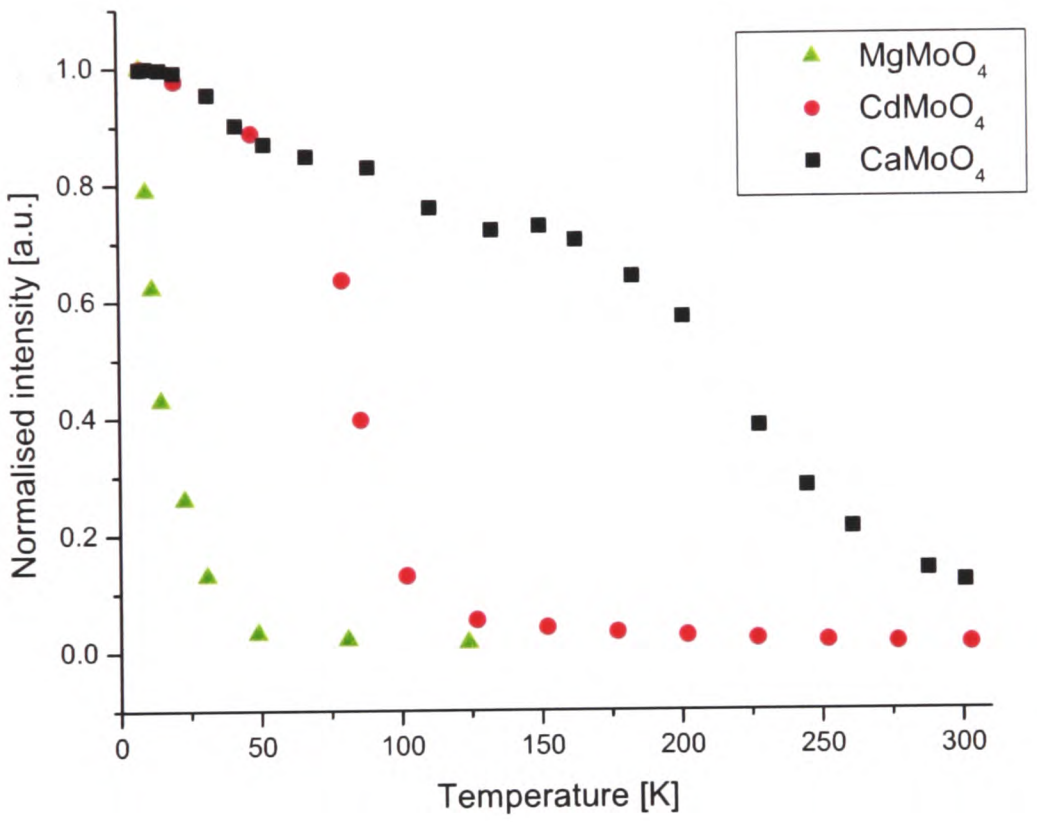

Figure 6.12: *The temperature dependence of the integrated intensity of the luminescence of $CaMoO_4$, $CdMoO_4$ and $MgMoO_4$*

light yield at room temperature. The quenching temperature T_q is 210 K for $CaMoO_4$, for $MgMoO_4$ it is T_q= 20 K and for $CdMoO_4$ it is T_q=80 K. The emission spectra of these crystals have a composite character and the best fit to the experimental results is obtained using a two Gaussians decomposition. The three molybdates have the same scheelite structure as $CaWO_4$ and it is believed that the emission characteristics can be interpreted in terms of the same model [130]. The higher energy emission band is associated with the radiative recombination of the electron-hole pairs localised at the

MoO_4^{2-} group [131]. This supposes that the low energy part of the spectrum is caused by defect emission. The structures visible in temperature dependence of the luminescence light yield of the $CaMoO_4$ [126] can then be attributed to this composite structure of the luminescence. At 8K, the molybdates have an integrated luminescence of 30% ($CaMoO_4$), 80% ($CdMoO_4$) and 30% ($MgMoO_4$) of $CaWO_4$. Given the high proportion of emission thought to be caused by defects, there are good prospects to improve the luminescence of these materials so that they may be as good CPSD candidates.

The decay time of the molybdates is in general found to be longer than that of the

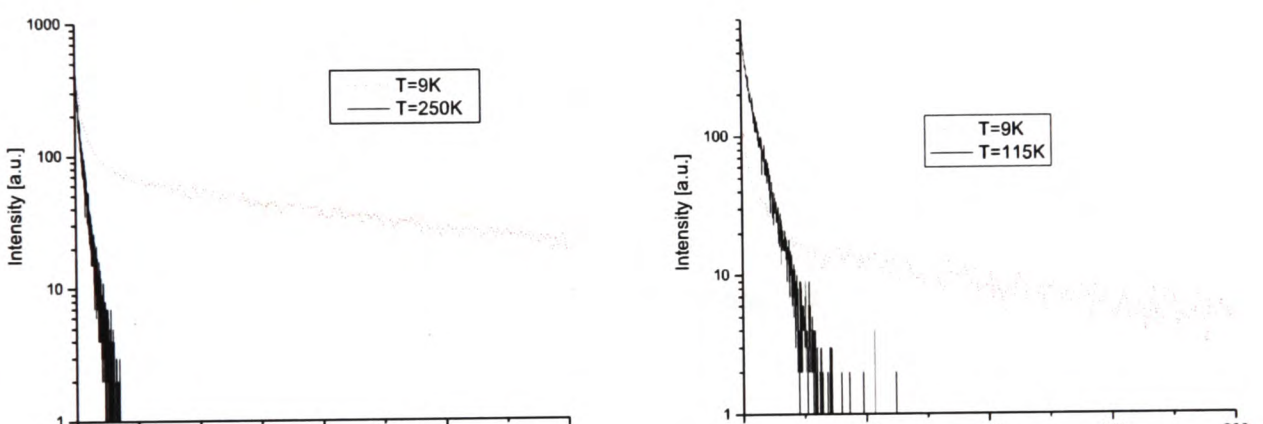

(a) (b)

Figure 6.13: *Decay time spectra of (a) $CaMoO_4$ and (b) $CdMoO_4$ at room and liquid helium temperatures*

tungstates [132]. Fig. 6.13(a) and (b) shows the decay spectra of $CaMoO_4$ and $CdMoO_4$. The principle decay times of each of the scintillators at 9K was found to be 650μs and 600μs for $CaMoO_4$ and $CdMoO_4$ respectively. Since $CdMoO_4$ does not scintillate at room temperature, the shorter decay curve shown in the figures is measured at the highest temperature at which the scintillation is intense enough to characterise. The measured decay times compare favourably with data available in literature for $CaMoO_4$ [131] and $CdMoO_4$ [133]. Though these decay times are longer than for $CaWO_4$ and $ZnWO_4$, they are not so long as to preclude the use of these molybdates as CPSD detectors.

6.2.4 CaF_2 and MgF_2

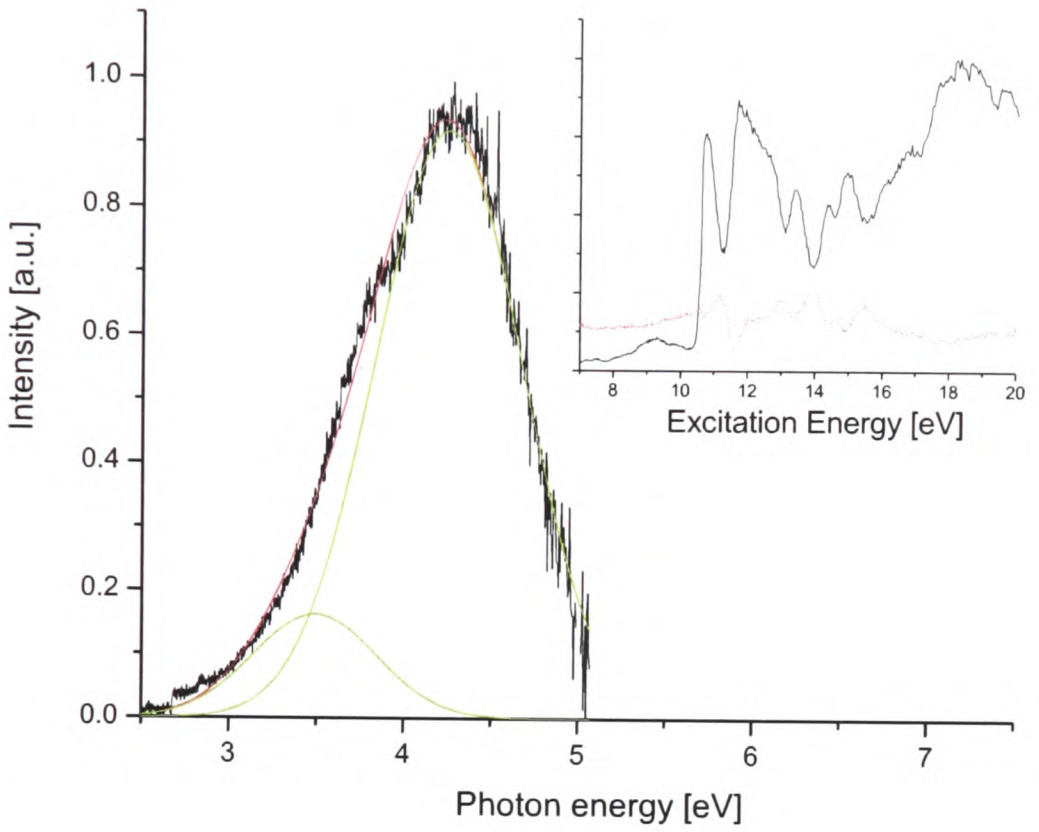

Figure 6.14: *The luminescence spectrum from 31eV VUV excitation, fitted to a sum of Gaussians. Inset: The excitation (solid) and reflection (dot) spectra*

Dark matter search experiments expect a very low event rate, and hence seek to increase the number of detected events. For experiments using low temperature techniques, this is usually achieved by increasing the density and WIMP interaction cross section of target materials in the detector. This requirement can be simplified to maximising the atomic mass of the constituent elements in the scintillator. This is a valid approach if the interactions between WIMPs and nuclei are spin-independent, or at least contain a significant spin-independent component. However if the dominant interaction is spin-dependent, then it is desirable to maximise spin interaction cross-section. Fluorine is an example a nucleon with a high spin interaction cross section [22] and hence halide compounds could become important materials in WIMP searches. CaF_2 has already been shown to be a suitable cryogenic detector when doped with Eu [134]. However there is an obvious prob-

lem for the use of Eu doped CaF_2 for rare event searches in that Eu cannot be obtained without radioactive isotopes. Furthermore, even though pure CaF_2 is a well studied material there was a need for a more direct comparison of performance with respect to other scintillators such as $CaWO_4$.

Tests were carried out on a nominally pure CaF_2 crystal of unknown origin. The main emission band we observe is at 4.25eV. This matches the emission band reported in literature [135, 136, 89, 96]. A second band is observed at 3.5eV, matching the reported band of 3.8eV reported as being existent in nominally pure CaF_2 [135] within the errors of the fit. Since the CaF_2 used for the purpose of these studies is from an unknown origin, it is necessary to consider if any of the emission could be caused by impurities. The possibility of Eu doping can be eliminated since the peak emission of Eu^{2+} in CaF_2 at 2.9eV [137] is not observed for any excitation. A review of the luminescence properties of CaF_2 with other dopants such as Ce^{3+}, Mn^{2+} or other earth metals indicated that these cannot account for the luminescence bands [136, 138]. Excitation spectrum studies were carried out looking at emitted light of wavelength 5.0 and 3.0 eV (this allows to separate the luminescence of each band). The excitation spectra showed no variation with respect to the spectrum obtained for peak emission (see inset). This indicates that the same valence band is the origin of the emission. The second band is reported in literature as being due to STE emission perturbed by lattice defects. Denks et al. [136] report an increase in the emission of a 3.8eV line in CaF_2:Mg compared with pure CaF_2. The Mg^{2+} ions replacing Ca^{2+} ions act as the required lattice deforming defect which tends to confirm this theory. As for the molybdates, developments in crystal production techniques could lead to an increase in overall light yield. CaF_2 also benefits from a lower refractive index (1.40 at 500nm) allowing for more photons to escape the crystal and hit the detector. In addition CaF_2 has a high melting point (1360K) which makes it a suitable candidate for the deposition of a cryogenic detector. The light yield of CaF_2 is already comparable with that of $CaWO_4$ when subjected to particle excitation,

and it is known that its light yield can be further improved with dopants. CaF_2:Mn is an example of non-radioactive doping which results in an increased light yield [136]. Though in this case the long decay time characteristics indicate that CaF_2:Mn will not be a suitable candidate [139], an appropriate R&D program may result in high luminescence, low background CaF_2 crystals being produced.

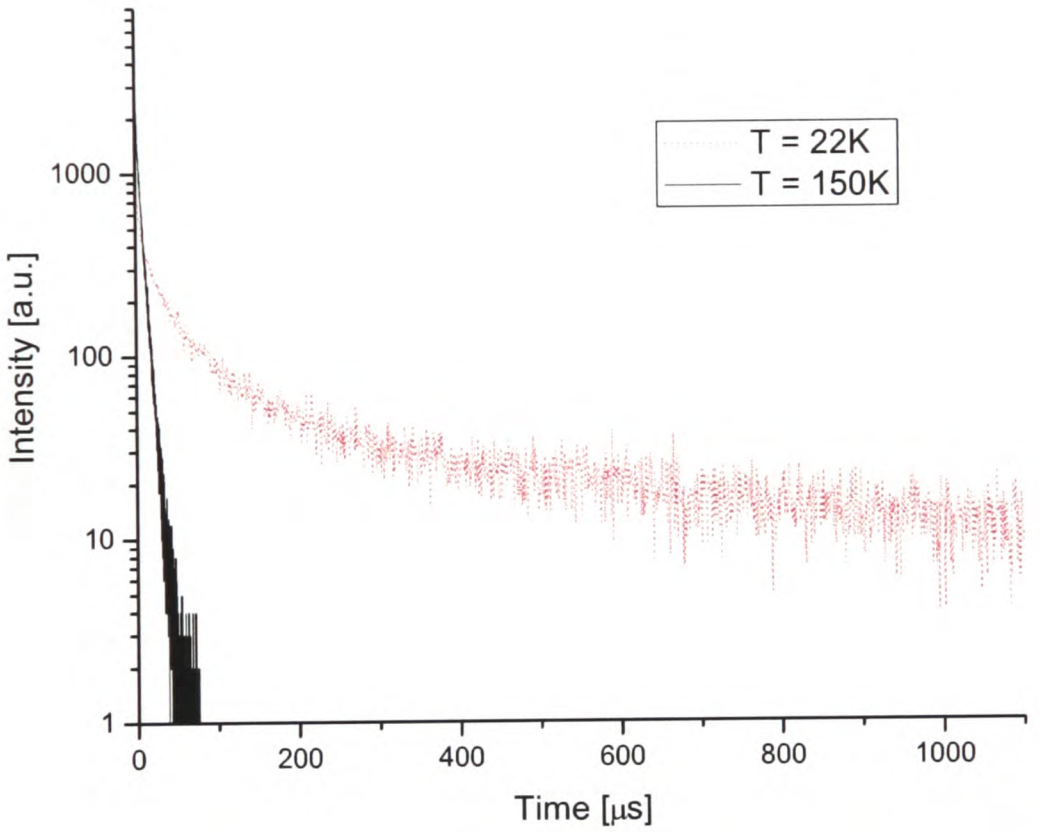

Figure 6.15: *Time decay spectrum of CaF_2 measured using the MPCC technique*

The decay time of CaF_2 measured in the time decay setup is shown in Fig. 6.15. The principle decay time at room temperature is measured as 6μs. This becomes close to 600μs when measured at temperatures of 20K.

A less well studied though complementary fluoride material which suits the requirement of low background radiation is MgF_2. The excitation and luminescence spectra of MgF_2 show very much the same properties of CaF_2. The main excitation peak can be attributed to excitonic emission. The luminescence band is centred at 3.0eV, in agreement with the reported luminescence band [140, 141]. It is also composed of a secondary band at 3.5eV

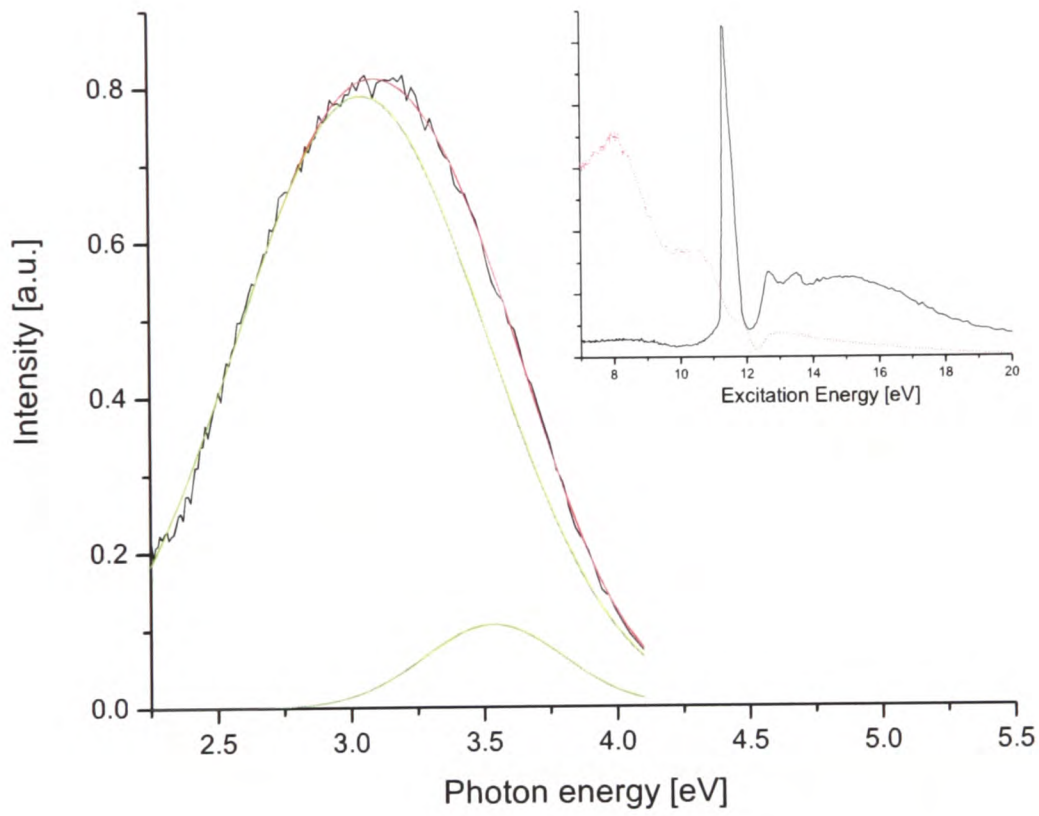

Figure 6.16: *The scintillation properties of MgF_2. (a) Main: The luminescence spectrum from 31eV VUV excitation. Inset: The excitation (solid) and reflection (dot) spectrum of MgF_2*

which, following the model of CaF_2, is assigned to perturbed STE emission. The low light yield of MgF_2 did not permit to measure the decay time and also suggests that unless suitable dopants are found, MgF_2 will not be a suitable candidate for CPSD detectors which require high sensitivity.

6.2.5 Al_2O_3:Ti

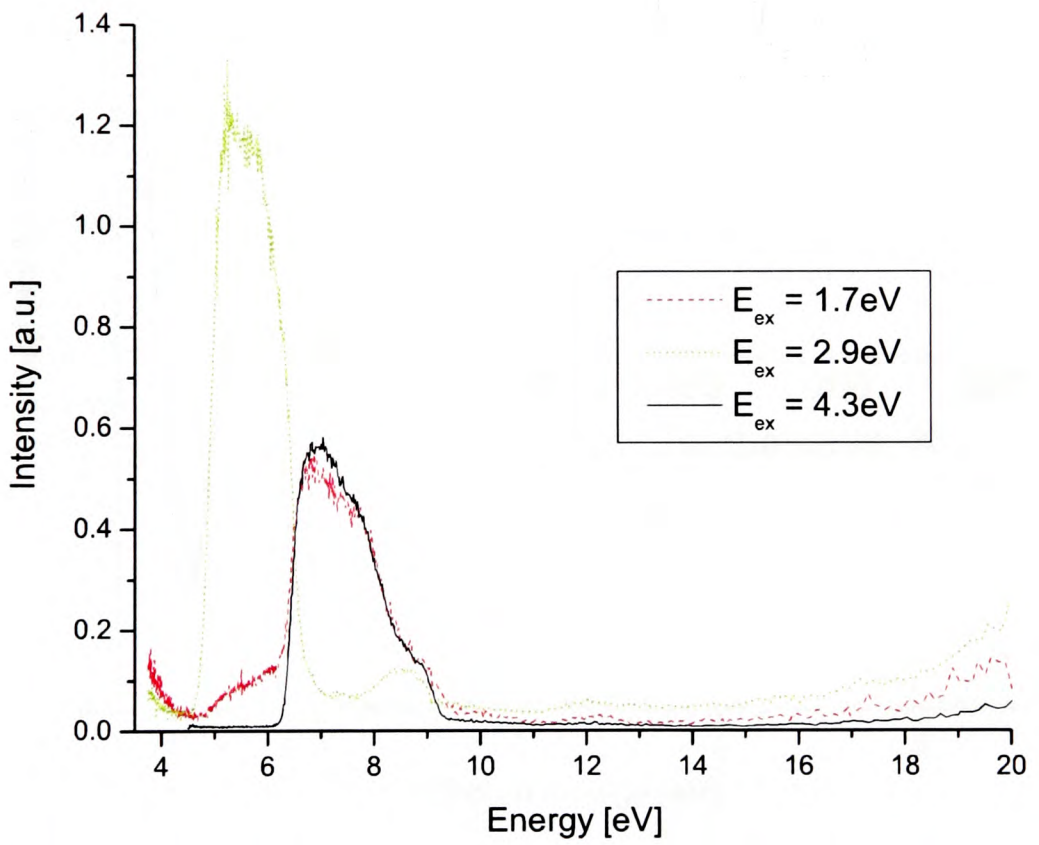

Figure 6.17: *Excitation spectrum of the different bands of Al_2O_3:Ti.*

The final material to be considered was Ti-doped Al_2O_3. Pure Al_2O_3 has already been used in CRESST I [142] as a phonon detector. It is believed that Ti-doped Al_2O_3, which is known as a very efficient laser material, can be adapted as CPSD. As can be deduced from the excitation spectrum, the emission mechanism of Al_2O_3:Ti is very complicated and will not be discussed in detail here. The usual emission due to Ti^{3+} ions was observed in the near infrared at 1.7eV and also at 2.9eV [143]. The emission spectrum was measured over

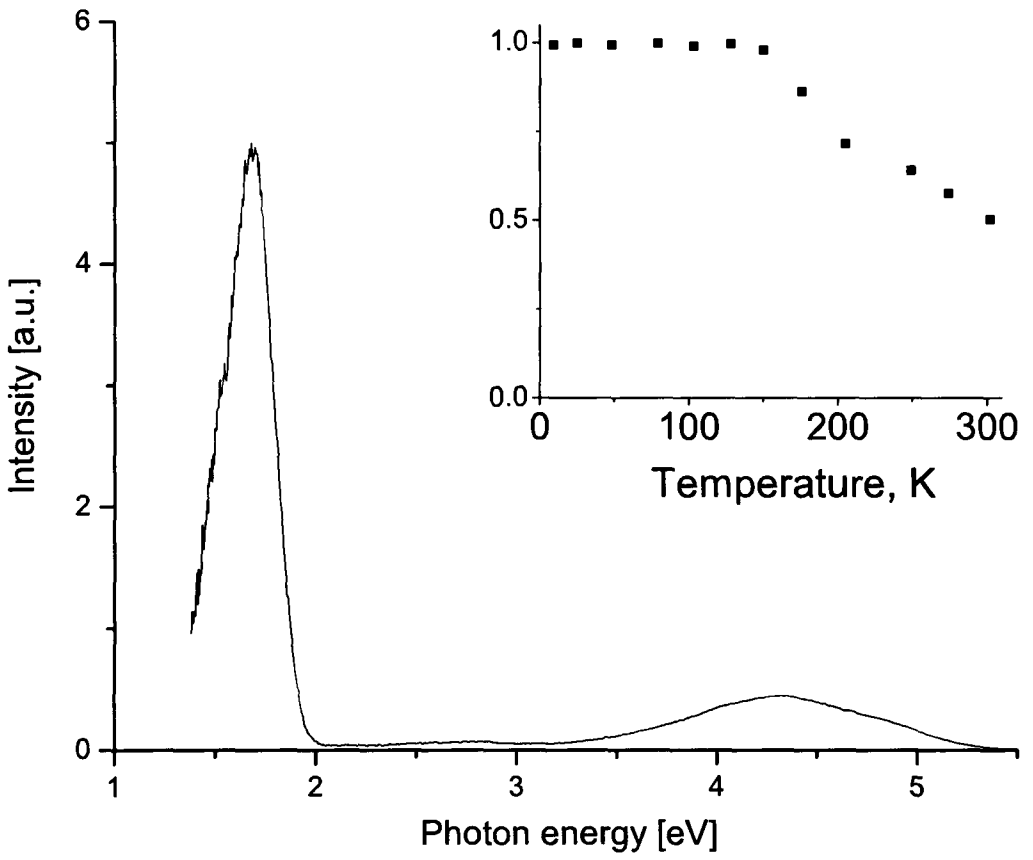

Figure 6.18: *Main: Luminescence spectrum at 31eV VUV excitation. Inset: Temperature dependence of the integrated luminescence.*

a wide range of wavelengths which resulted in the detection of a previously unreported UV luminescence peak at 4.3eV. This peak accounts for roughly one third of the integrated emission light yield. This highlights the necessity of performing luminescence studies on potential CPSD materials. Knowing that a significant proportion of the scintillation occurs in the UV range will allow modifications to be made to the light collection setup and hence increase the amount of light detected. The decay time of this last band of Al_2O_3 is too short to be measured using the MPCC technique (~138ns at 300K [144]). The relative light yield of Al_2O_3:Ti was estimated at 30% of $CaWO_4$ and it is thought that it could be significantly optimised by studies on the concentration of the titanium. This places Al_2O_3:Ti as a good candidate for CPSD so long as difficulties in collecting the light are resolved.

6.3 Summary of the scintillation properties of potential CPSD materials

All of the above materials were selected on the basis that they did not naturally contain radioactive isotopes, and that they had demonstrated good scintillation qualities. Of the materials tested, only MgF_2 had a light yield too low to be considered as a CPSD. Table 6.1 shows a summary of the materials tested and their properties of relevance to rare events searches. It should be noted that the pure $CaWO_4$ and $ZnWO_4$ used in these studies have already gone through a substantial phase of research and development to improve the scintillator quality. As such there are good reasons to be optimistic that the light yield of the other materials can be optimised to increase their worth as CPSD.

The list determined here was established primarily with the consideration of dark matter searches in mind. Other materials which are frequently reported as being of interest for neutrino-less double beta decays for example were not studied in as much detail. Further-

Table 6.1: *Summary of the scintillation properties of potential CPSD*

Material	Peak [eV]	LY [% $CaWO_4$ at 31eV]	T_q	Main decay (T) [μs (MPCC)]
$CaWO_4$	2.9	100	>300	405±20
$ZnWO_4$	2.45	110	>300	110±15
$CaMoO_4$	2.2	30	210	650±10
$CdMoO_4$	2.15	80	80	600±100
$MgMoO_4$	2.4	30	30	
CaF_2	4.25	30	~180	600±100
MgF_2	3.0	5	~50	
Al_2O_3:Ti	2.9, 4.3	30	~300	

more, since there has been no dedicated research project on the development of CPSD, the searches had to be limited to what are largely available commercial scintillators. This had led to possibly very interesting scintillators not being investigated. As an example one can consider $ZnMoO_4$, which would be the perfect complementary material for the three most promising dark matter CPSD, namely $CaWO_4$, $ZnWO_4$ and $CaMoO_4$. Another very interesting family of materials that has escaped investigation is the oxyfluorite group [133, 145, 146, 147] such as $Cd_2WO_3F_4$, which has existing members for molybdates and tungstates. The huge advantage of these materials is that they allow to search for all kinds of WIMP spin-dependent and spin-independent interactions at the same time.

The main purpose of the works carried out here was not to compile a complete list of all possible CPSD materials, but rather to develop a standard method for investigating the relative merits of potential scintillators. Using a range of techniques, both well developed such as VUV measurements, or newly developed for this purpose such as the MPCC technique, there is now a series of simple measurements that can be performed to investigate the luminescence properties of scintillators comprehensively. For each material investigated the following parameters can be obtained: spectroscopic characteristics (VUV synchrotron excitation), relative light yield at WIMP interaction energies (keV synchrotron excitation and MPCC) and finally decay time characteristics all at temperatures

close to the operating point of CPSD experiments. Furthermore, and very importantly in the context of the current work, these studies provide a good understanding of the luminescence properties of a number of scintillators which will be imperative for the simulation of the light collection efficiency.

Chapter 7

The optical properties of $CaWO_4$

One of the main reasons for investigating the luminescence properties of materials was to obtain the spectrum to be used for the generation of light in MC simulations. Apart from the luminescence properties of the scintillators, it is also necessary to know the optical properties of the material. The following section contains a review of the known optical parameters of $CaWO_4$ and a presentation of some of the methods to measure these. As the optical properties of crystals are known to be sample dependent, it is necessary to measure the specific properties of the crystals to be used in MC simulations. A reference crystal is used for this work which will later be used for tests of the MC program. The crystal is an off-cut from a CRESST crystal, thus being one of the highest purity $CaWO_4$ produced so far and ideal for testing intrinsic optical properties. The properties of the reference crystal are investigated in detail, including a part focusing on surface properties (polishing). Results from measurements of the attenuation coefficient and refractive indexes of $CaWO_4$ are presented.

7.1 Review of the optical properties of $CaWO_4$

There are three optical properties (as opposed to luminescence properties) which are important in the simulation of light collection in HIS. These are the refractive index, the absorption coefficient and the scattering coefficient. The refractive index of a scintillator determines the trapping angles and reflection coefficients at the surface of the crystal.

The absorption coefficient will determine how much light is re-absorbed by the bulk of the crystal and hence is also very important to determine. Scattering in the crystal will reduce the number of trapped photons and hence increase the light yield. These last two cannot be measured directly, though they can be constrained by performing transmissivity measurements. There is a further interest in measuring the transmissivity as a method based on this was developed to measure the quality of CMS $PbWO_4$ crystals [148]. A secondary aim of this chapter will be to explore to what extent this technique could be transferred to $CaWO_4$.

The difficulty in obtaining accurate results is associated with imperfections of the crystal surfaces. A sizable part of this section looks at the effects that non-perfect surface conditions can have on transmissivity measurements and how these imperfections can be uncovered. Once the surface effects are understood and controlled, measurements of the transmissivity of the reference crystal are performed. Finally, in order to further understand the observations made on the reference crystal, transmissivity measurements are made on two samples of different thickness cut from the same ingot. The idea behind this is to eliminate effects due to the surfaces by comparing the transmissivity in both samples. Before looking at the details of the experiments to measure the optical properties, a review of the known properties is presented. Table 7.1 shows reference values for the refractive index of $CaWO_4$ available from literature. The ordinary refractive index is denoted by n_o whilst n_e refers to the extraordinary refractive index. Values close to those

Table 7.1: *Reference refractive index of $CaWO_4$*

Wavelength [nm]	$n_o \pm 0.0005$	n_e
436 [149]	1.954	1.972
450 [150]	1.950	1.968
546 [149]	1.927	1.943
600 [150]	1.918	1.934
656 [149]	1.913	1.928

reported in Table 7.1 can also be obtained from reflectivity measurements [151]. The

most common method for measuring the refractive index of birefringent materials is by measuring the deviation of a beam through a prism [149, 150, 152]. This technique could not be used as the reference crystal was not of the appropriate shape. To measure the refractive index, one possibility is to measure the reflection spectrum of a beam directed onto a plane surface of the crystal [153, 154]. For a beam of light with normal incidence and circular polarisation the reflectivity at the boundary of two materials is linked to the refractive index of the crystal by equation (7.1):

$$R = \frac{(n_1 - n_2)^2}{(n_1 + n_2)^2} \tag{7.1}$$

where n_1 and n_2 are the refractive indexes of the two materials. Using the values from Table 7.1 and assuming the photons are parallel to the extraordinary index, one can calculate the value for the reflectivity of $CaWO_4$/air boundary at 436nm is 10.7%. Transmissivity measurements usually have to be corrected for this surface reflectivity using equation (7.2).

$$T = \frac{(1 - R)^2 e^{-\alpha_{att} d}}{1 - R^2 e^{-2\alpha_{att} d}} \tag{7.2}$$

where α_{att} is the attenuation coefficient in the direction of the photons and d is the thickness of the sample. The simplest method for measuring transmissivity is by shining a collimated light beam through the sample and comparing the intensity of the light detected with that when the sample is not present. This causes a square factor to appear in equation (7.2) as the beam traverses two faces (in and out of the crystal) and hence the measured intensity needs to be corrected for reflectivity twice. The denominator of equation (7.2) is the correction for multiple reflections. The attenuation length of $CaWO_4$ measured in this way is cited to be of the order of 10-30cm [155, 52, 38], the range of lengths being due to differences in the crystals measured. A common way of presenting the attenuation is in terms of the attenuation coefficient, which is the inverse of the attenuation length: $\alpha_{att} = L_{att}^{-1}$. This notation has the semantic advantage in that an

increase in the coefficient represents an increase in attenuation. The attenuation length is then related to the scattering and the absorption as shown in equation (7.3).

$$\alpha_{att} = \alpha_{abs} + \alpha_{scat} \tag{7.3}$$

where α_{abs} and α_{scat} are the absorption and scattering coefficients respectively. There is no way yet reported on experimental techniques to measure either α_{abs} or α_{scat} directly. In order to have a complete set of parameters for the MC simulations it would be necessary to calculate either α_{abs} or α_{scat} from first principles. In an ideal crystal (free of impurities and lattice deformations), scattering occurs through the process of Rayleigh scattering. The cross-section of this process (σ_{RS}) in a translucent medium can be calculated using equation (7.4) [156].

$$\sigma_{RS} = \frac{24\pi^3}{\lambda^4 N^2}\left(\frac{n^2-1}{n^2+2}\right) \tag{7.4}$$

where N is the number of scattering centres per unit volume and n is the refractive index. This equation is valid under the condition that $\lambda \gg R_{scat}$ where R_{scat} is the radius of the scattering centre and λ is the wavelength of the light. In pure $CaWO_4$, the radius of the scattering centres (constituent ions) is much smaller than the wavelength of light. The scattering coefficient is then given by equation (7.5).

$$\alpha_{scat}(\lambda) = \sum_i N^i \sigma^i_{rs}(\lambda) \tag{7.5}$$

where the summation is over the number of scattering centres. As a rough calculation, the approximation is made that each $CaWO_4$ "molecule" contributes two scattering centres with equivalent number density, namely the Ca^{2+} ion and the WO_4^{2-} complex. Therefore the sum simplifies to a sum of two equal contributions:

$$\alpha_{scat}(\lambda) = 2N\sigma_{RS}(\lambda) \tag{7.6}$$

$CaWO_4$ has a density of 6.06g/cm^3 and an atomic mass of 288. This is equivalent to N=1.25x10^{22}cm^{-3}. Table 7.2 shows the values of the scattering coefficient of $CaWO_4$ calculated for 4 wavelengths using equation (7.6). The values in Table 7.2 are the minimum

Table 7.2: *Rayleigh scattering coefficients of $CaWO_4$*

Wavelength [nm]	L_{scat} [cm]	α_{scat} [cm^{-1}]
405	90.9	0.011
546	299	3.35x10^{-3}
633	541	1.85x10^{-3}
1060	4.25x10^3	2.36x10^{-4}

amount of scattering that can be expected for a crystal of $CaWO_4$. In fact much more significant sources of scattering are present due to impurities, defect centres and lattice dislocations. Measurements of the attenuation for $CaWO_4$:Nd^{3+} performed with a laser beam of 1060nm [157] give an approximate value of $\alpha_{att} = 0.01$ cm^{-1}, approximately 100 times more than expected from pure Rayleigh scattering. This is thought to be due to defect scattering. It is hence not possible to calculate α_{scat} from first principles. Since α_{abs} cannot be calculated either, a separate method must be found to evaluate these before performing simulations. This will be the subject of the next chapter. This chapter focuses on measurements of the refractive index and the attenuation coefficient in order to provide at least two parameters for the MC.

7.2 Measurements of the properties of $CaWO_4$

The reference $CaWO_4$ crystal used for the measurements has dimensions 8.2x10.0x10.3mm, cut from a larger ingot grown using the Czochralskii technique. The crystal was produced from raw material of 4N or better purity and was manufactured by SRC "Carat" (Lviv, Ukraine). The principle optical axis of the crystal is parallel to the edge of length 10.3mm. The 6 faces of the $CaWO_4$ are labelled A-F, with the optical axis being perpendicular to faces E and F (opposite pairs are A-B, C-D and E-F) as shown in Fig 7.1. The following

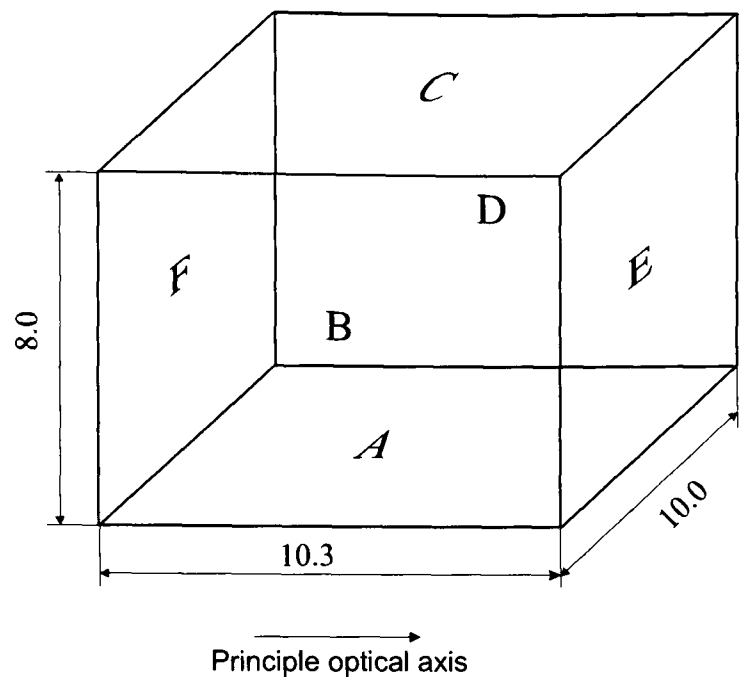

Figure 7.1: *Diagram of the faces of the $CaWO_4$ crystal used in the experiments*

subsections present the results of measurements of the transmissivity on this crystal.

7.2.1 Effects of the surface polish on the transmissivity

Since the crystal is to be used as a reference crystal for the calibration of MC simulations, it is important to verify that all the properties of the crystal can be reproduced by the MC. This is specially true for the surface properties since Litrani cannot reproduce surface irregularities of birefringent crystals. A combination of transmissivity measurements and surface examinations were used to investigate the detailed properties of the crystal. A brief description of the transmissivity setup and the microscope used to examine the surface are given below.

The transmissivity of the $CaWO_4$ sample was measured using a a Perkin-Elmer Lambda 15 UV/VIS spectro-photometer. The spectro-photometer uses a variety of sources to produce collimated light in the range 250-800nm with a beam spot diameter of $\sim$1mm. A schematic diagram of the setup for measuring the transmissivity is shown in Fig 7.2. If the surface of the crystal is de-polished, the transmissivity will be reduced due to scattering and absorption at these surfaces. To examine the surface properties an auto-collimated

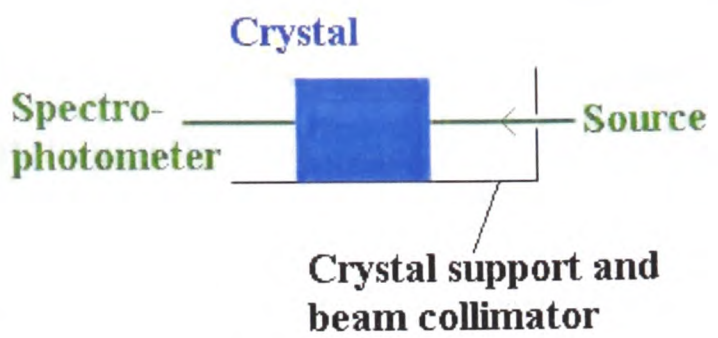

Figure 7.2: *Experimental setup for transmissivity measurements. The diagram is not to scale.*

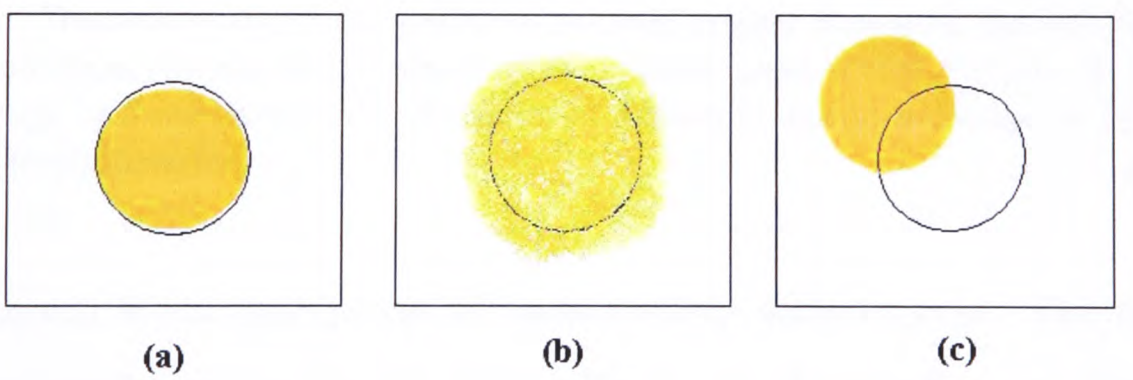

Figure 7.3: *Reflected spot image when viewed under a microscope. The black target ring represents the expected zone for a smooth surface. (a) Image of a well polished surface; (b) image of a surface with uneven polish; (c) image of a well polished surface with the beam not normal to the reflection surface.*

microscope was used. Fig. 7.3 illustrates how surface defects show up in this microscope. When considering transmissivity measurements, three possible surface "degradations" exist: bad polish, curved surfaces, and non-parallel surfaces. If the surface is perfectly smooth (well polished) and planar, a perfectly circular light spot can be observed within the target area. If a blurred circle is observed this is an indication of an unpolished surface. If the spot only falls partially in the target area, this is an indication of non-planar surfaces (curved or non-parallel).

Using the microscope to examine the faces (as cut and polished by the producer) shows

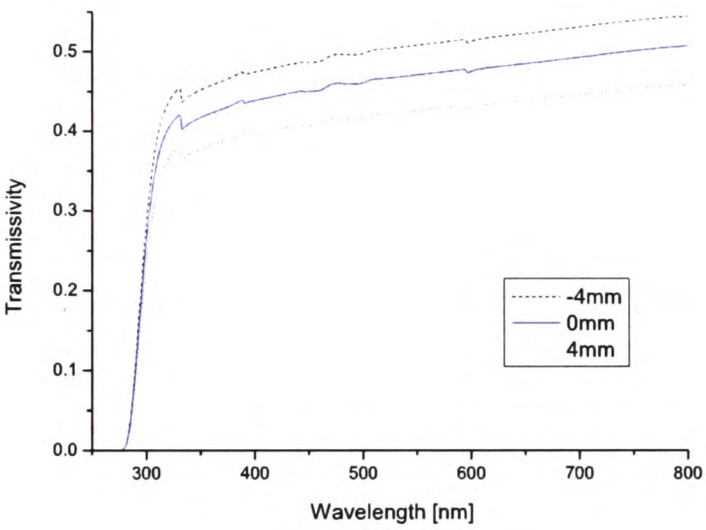

Figure 7.4: *Transmissivity of the producer polished crystal measured through faces A-C. The position 0mm represents the centre of the crystal, 4mm is close to face A. Each line is the average of 3 measurements, the jump at 320nm is due to a change in light source in the spectrophotometer.*

that the crystal is not appropriate for transmissivity measurements. The faces were curved, non-parallel and of unequal polish. These imperfections are not visible to the naked eye, but due to the high refractive index of $CaWO_4$ they have a large effect on the measured transmissivity. Fig. 7.4 shows that the transmissivity can vary by up to 25% with the beam spot position along face C. Measurements of the transmissivity for the same face rotated by 180^o around the direction of the incoming light produced variations of the same order. To eliminate the doubt that the variations are due to microscopic surface effects, a series of measurements were carried out around a localised point on each

of the faces. The variations observed did not exceed 1%, indicating that the difference of transmissivity is due to macroscopic effects.

The crystal was re-shaped to make all surfaces plane and parallel. The crystal was placed in a polishing jig and checked for being planar using an interferoscope [158]. The surfaces were measured to be optically flat to at least 2μm using the interferoscope. Before re-shaping, the crystal was gently heated as sudden heat changes cause the $CaWO_4$ to crack. The crystal was then polished starting with 1200 grit. It was further polished using a polishing lap of 1μm diamond suspension lubricated with ethandiol. Finally the crystal was re-polished using 0.25μm diamond suspension. The above was performed by the crystal cutting group of the physics department of the University of Oxford. When inspected, all surfaces were now found to be plane except very close to the corners of the crystal where some curvature was still noticeable. Small deviations from perfect parallelism of the faces were observed for all pairs of faces except the pair A-C. None of the surface displayed a perfect polish though surfaces A, C, E and F all had a definite beam spot, surface E being the clearest. There were also a small number of scratches visible to the attentive naked eye. These cover a tiny fraction of the total crystal surface and are not expected to affect the optical properties of the crystal significantly. Surfaces B and D were still not as well polished as could be hoped for so measurements were carried out on faces E and A or the pair of faces A-C, E-F.

The re-polished crystal was placed in an upgraded version of the transmissivity setup previously used. A vernier scale was added to increase the accuracy of the position measurements. A picture of the setup is shown in Fig. 7.5. The crystal is pressed against the far edge and the vernier scale is used to simultaneously move the support table and measure the displacement of the crystal. Fig. 7.6 shows the position dependence of the transmissivity of Face A. As can be seen, the re-polishing of the face has significantly reduced the position dependence of the transmissivity. In the central area of the crystal (range -2 to 2mm indicated by straight lines) the variation of the transmissivity is of the

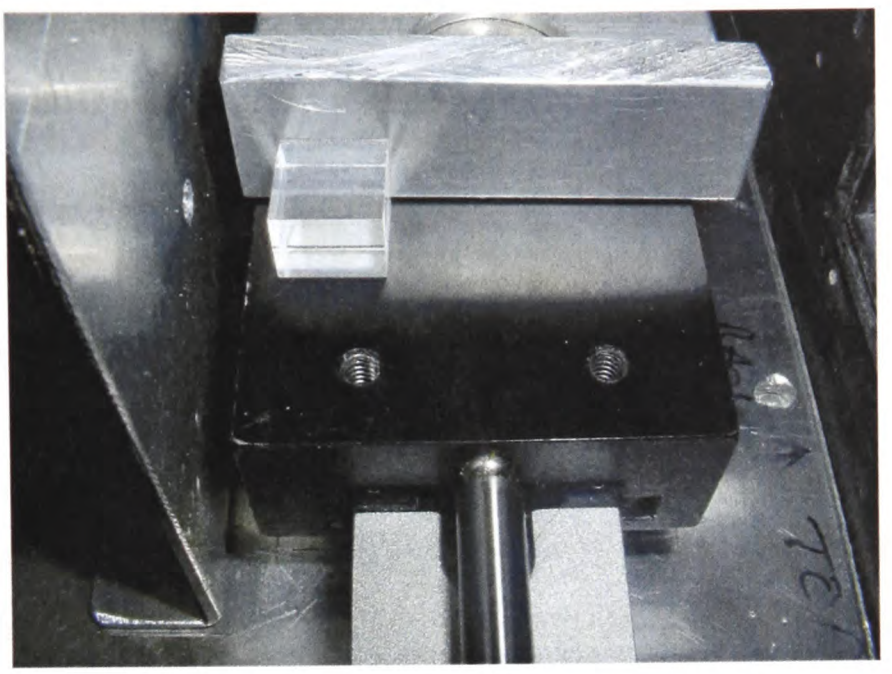

Figure 7.5: *Detailed view of the moving table installed in a spectrophotometer in order to measure the position dependence of the transmissivity of the reference $CaWO_4$ crystal. The hole in the aluminium plate on the left is the entrance position of the beam. The hole is further reduced in size for the experiment. The metal bar coming down the centre of the picture is the vernier scale used to measure the position of the edge of the crystal.*

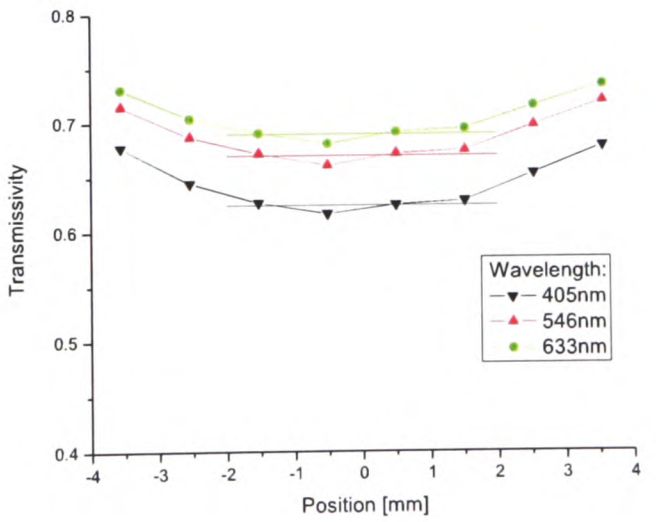

Figure 7.6: *Position dependence of the transmissivity of re-polished face A. The flat lines indicate the zone in which accurate measurements can be carried out.*

same order as the statistical errors between measurements. This indicates that this is an appropriate zone for accurate transmissivity measurements. To obtain the transmission coefficient, it is necessary to measure the reflectivity of the crystal.

7.2.2 Refractive index measurements and deduction of the transmission coefficient

An ellipsometer (also known as a reflection polarimeter) was used to measure the refractive index from which the reflectivity can be calculated. An ellipsometer measures the change in polarisation of a collimated beam when it is reflected from a surface. For these measurements a Rudolph AutoEL III nulling ellipsometer is used. A nulling ellipsometer is composed of a light source, a light source polariser, a mobile sample holder, a pre-detector polariser and a light detector. The mobile sample holder serves to line up the crystal such that the face being measured intersects the light beam in the place and at the angle required by the setup. The reflection off the surface causes the beam to change polarisation. The two polarisers are automatically rotated to a position where the detected light intensity is minimum which enables the machine to calculate the refractive index of the crystal [159]. The ellipsometer used has three wavelength selecting filters for 405, 546 and 633nm with bandwidth smaller than 10nm. The refractive index

Table 7.3: *Refractive index of $CaWO_4$ measured with a Rudolph AutoEL nulling ellipsometer averaged over 3 measurements*

Wavelength [nm]	$n_o \pm 0.003$	$n_e \pm 0.003$
405	1.990	2.002
546	1.955	1.969
633	1.945	1.961

of the reference crystal of $CaWO_4$ is shown in Table 7.3. Results are presented in terms of refractive index measured at face A (n_o) and face E (n_e). The values measured using this technique are approximately 0.04 higher than those usually quoted [149] [151] (from reflectivity measurements) whilst maintaining a birefringence of value Δn=0.02. These

figures are in agreement within errors when one considers the relatively large uncertainty of reflectivity measurements (due to surface irregularities.)

Table 7.4: *Attenuation length and coefficient of $CaWO_4$ as measured in a spectrophotometer. The values for transmissivity are corrected for reflectivity.*

Wavelength [nm]	T [%]	L_{att} [cm]	α_{att} [cm^{-1}]
405	69.3	7.94	0.126
546	73.0	11.6	0.0862
633	74.2	13.7	0.0730

The refractive index values can now be used to correct for the reflectivity of each of the surfaces in order to obtain α_{att} from the transmissivity measurements. The pair of faces with best polish (faces E and F) were selected for the performance of transmissivity measurements. Using the previous measurements of the refractive index and substituting into equation (7.2) it is possible to extract values for the attenuation length of $CaWO_4$ at different wavelengths. This is shown in Table 7.4. The values obtained are compatible with the typical values of attenuation in $CaWO_4$. In order to further investigate the contribution from surface effects, the transmissivity of two extra crystals was investigated.

7.3 Improved measurements using two cylindrical crystals

The two crystals were cut from a ingot grown by CARAT (Lviv) using the Czochralskii technique. The crystals are the same in all respects except that one is 5.1mm thick and another is 11.0mm thick. Both crystals have a radius of 5mm and have the optical axis aligned with the axis of cylindrical symmetry. The producer of the crystal was asked to take special care in producing crystals with perfectly flat faces and the best polish possible. Nonetheless, when viewing images through the crystals, they were seen to act as weak focusing lenses, indicating that the surfaces were not perfectly flat. The position dependence of the transmissivity was measured and an increase of a maximum of 2%

was observed with the increase of radial position. Following the method applied on the reference crystal, the transmissivity of the two crystals was measured in the centre of the plane faces. The transmissivity of the crystals at three different wavelengths are presented in Table 7.5. Before examining the significance of these results, let us consider

Table 7.5: *Transmissivity of the cylindrical crystals*

Wavelength [nm]	T (h = 5.1mm) [%]	T (h = 11.0mm)
405	78.4	75.2
546	79.9	77.6
633	80.3	78.2

the processes that occur when a beam of photons hits a surface of the crystal. It is usual to assume that a beam hitting a surface is either reflected with probability R, or transmitted with probability $T = (1 - R)$. Let us introduce a non-defined surface effect S, such that the relative intensity of the reflected beam is equal to SR and the relative intensity of the transmitted beam is $S(1 - R)$. This would correspond to a scheme where the surface under examination is partially absorbing. It can be shown [160, 161] that the transmissivity of a collimated beam through a crystal of thickness d, with surface effect S is:

$$T = \frac{S^2(1-R)^2 e^{-\alpha_{att}d}}{1 - S^2R^2e^{-2\alpha_{att}d}} \tag{7.7}$$

The above equation contains two unknown parameters (S and α_{att}) which requires two transmissivity measurements to be solved. Using the transmissivity values from Table 7.5 and the refractive index Table 7.3, a set of two non-linear equations is created which can be numerically solved using Mathematica [162]. The resulting values of S and α_{att} are shown in Table 7.6.

It is commonly accepted that surface contributions cause a reduction of the transmissivity due to scattering and absorption at each face, equivalent to saying S <1. However, estimations of the surface effects using equation (7.7) and shown in Table 7.6 indicate an

Table 7.6: *Attenuation coefficient and surface contributions calculated by comparing two cylindrical crystals of $CaWO_4$ of different size.*

Wavelength [nm]	α_{att} [cm]$^{-1}$	L_{att} [cm]	S
405	0.069	14.5	1.008
546	0.049	20.6	1.007
633	0.044	22.7	1.007

"increase" in transmissivity due to the surfaces ($S > 1$). The favoured explanation is that the crystals act like a weak biconvex lens with the radius of curvature decreasing with distance away from the principle "cylindrical" axis. This not only explains the positive contribution the surfaces have on the transmissivity but shows why the transmissivity increases as a function of radial position. Ignoring the effect of the surfaces will result in an underestimation of the attenuation coefficient. Using S=1 and the 405nm transmissivity of the thick crystal would yield an attenuation coefficient of 0.055cm^{-1}, about 20% lower than the value corrected for surface effects. This result is important in light of the

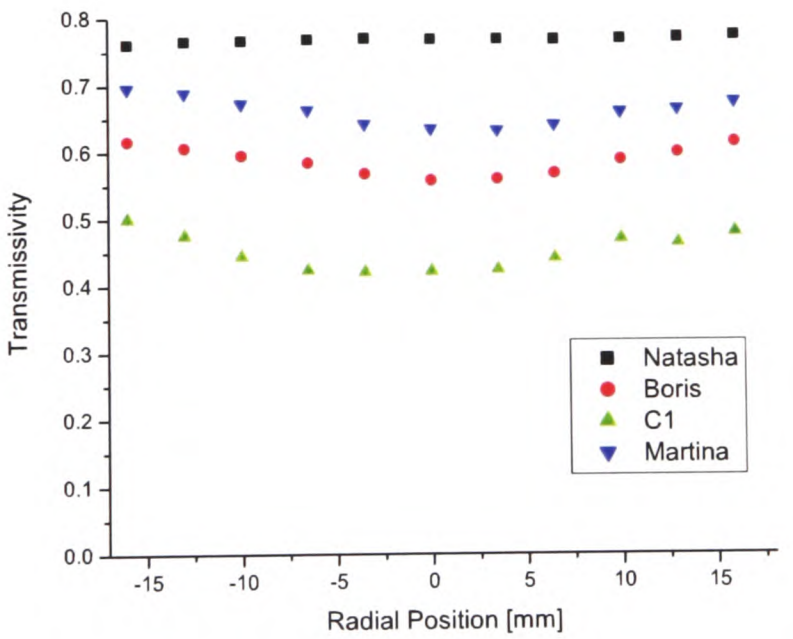

Figure 7.7: *Transmissivity of a number of CRESST crystals measured at 420nm*

experiments performed to understand the performance and light collection properties of the CRESST crystals.

Fig. 7.7 shows the position dependence of the transmissivity of 4 full size CRESST crystals measured by the Munich group [38]. There is a strong variation in transmissivity between the crystals, which is attributed to differences in purity and growth condition between the crystals. The crystals also exhibit the same position dependence trend as the crystals tested here leading to the conclusion that the faces are not planar. In fact there is a significant variation of magnitude of the position variation, from no observed variation (Natasha) to variations of $\sim$10% (C1). Given the efforts to obtain a set of crystals with uniform properties, the current results highlight the importance of developing a standard technique for the polishing and the shaping of crystals to be used as CPSD.

7.4 Conclusions

Measurements of the transmissivity of two cylindrical crystals have shown that the position dependence of the transmissivity is due to the slight convex shaping of the plane faces of these crystals. This is an important observation in the context of performing accurate MC simulations of crystals. The MC program Litrani is able to reproduce plane and curved faces, but not uneven surfaces. It is therefore necessary to ensure that the faces of the crystal are planar, which can be verified by using an auto-collimated microscope or by looking at the position dependence of the transmissivity of the crystal.

The reference crystal was polished such that the main surface area of the faces are plane to 2μm. The transmissivity of the crystal is constant to 2% in the central area of the faces which has allowed to measure an attenuation coefficient of 0.126cm^{-1} at 405nm. The surface effects for this crystal could not be estimated, but given the measurements on crystals with a similar polish, it is expected that they may cause an error of up to $\sim$20% on the attenuation. For MC simulations of this crystal to be accurate, it will have to be

demonstrated that the simulated light yield is not strongly affected by this error. The measurements of the refractive index of $CaWO_4$ are not affected by the small curvature of the faces. Using light of 405nm, the ordinary refractive index of $CaWO_4$ was measured as n_o=1.99 and the extraordinary index as n_o=2.002. These values will be used as the input for MC simulations described in the next section.

Chapter 8

The Monte-Carlo Refractive Index Matching Technique

The main aim of MC simulations is to predict the amount of light that can be detected from an experiment. The measured light yield (LY) of a scintillator is determined by LY = $N_0.\eta$ where η is the light collection efficiency and N_0 is the intrinsic light yield (note: the quantum efficiency of the detector is not yet included). In general, η is dependent on a number of parameters such the geometry of the crystal and the setup, and the optical properties of the materials used in the experiment.

$$LY = N_0.\ \eta(optical\ properties, geometry) \tag{8.1}$$

Even for simple experiments it is hard to evaluate η by analytical calculations [70, 163, 164] and hence Monte-Carlo (MC) simulations are used. In order to produce simulations which can predict the LY of an experiment, it is necessary to possess all the information on the optical parameters of the materials which are to be simulated. In many cases, materials are well characterised in terms of their optical properties, as is the case of air, water and metals. Heavy inorganic scintillators (HIS) as a general rule are not. This chapter presents the Monte-Carlo refractive index matching (MCRIM) technique which was developed as an iterative process to extract the unknown parameters from a MC/experiment combination.

8.1 Input parameters which cannot be measured directly

Nearly all of the optical parameters of the MC have been measured by experiment, including the refractive index, the emission spectrum and the attenuation coefficient (α_{att}). However there are three crucial optical properties which cannot be determined directly: the intrinsic light yield of the scintillator N_0, the absorption coefficient α_{abs} and the scattering coefficient α_{scat}. By performing measurements of the transmissivity, one can calculate the attenuation coefficient but this is not sufficient to determine the scattering and absorption coefficients. Since these coefficients are interdependent ($\alpha_{att} = \alpha_{scat} + \alpha_{abs}$) the problem of measuring the values of scattering and absorption is reduced to measuring any one of the two. This means that in the MC simulations there is only one unknown parameter related to α_{abs} and α_{scat}. There is a certain freedom in choosing how to enter this parameter in the MC and in accord with previous works [72, 73], the variable used is the ratio of scattering to absorption coefficients B:

$$B = \frac{L_{abs}}{L_{scat}} = \frac{\alpha_{scat}}{\alpha_{abs}} \tag{8.2}$$

B represents the chance of scattering versus the chance of absorption, or in other words, the relative chance of photons to "survive" an attenuating interaction. A crystal with a higher value of B has higher scattering (for constant α_{att}). In this way α_{abs} and α_{scat} are fully defined in terms of B and α_{att}. In the previous chapter, it was shown that α_{att} can only be measured to an accuracy of $\sim$20%. In order to perform accurate simulations, it is necessary for the LY to be independent of uncertainty on α_{att} of this order. The effect of α_{att} on the LY for a setup where a $CaWO_4$ crystal is placed on the window of a PMT has been investigated in the range α_{att}=0.126$\pm$0.025cm^{-1} (the setup is described in more detail in section (8.2.1). Fig. 8.1 shows that the LY is hardly affected by changes in α_{att}. Changes in of 20% in α_{att} cause changes in the LY of the order of 1%. Studies over a

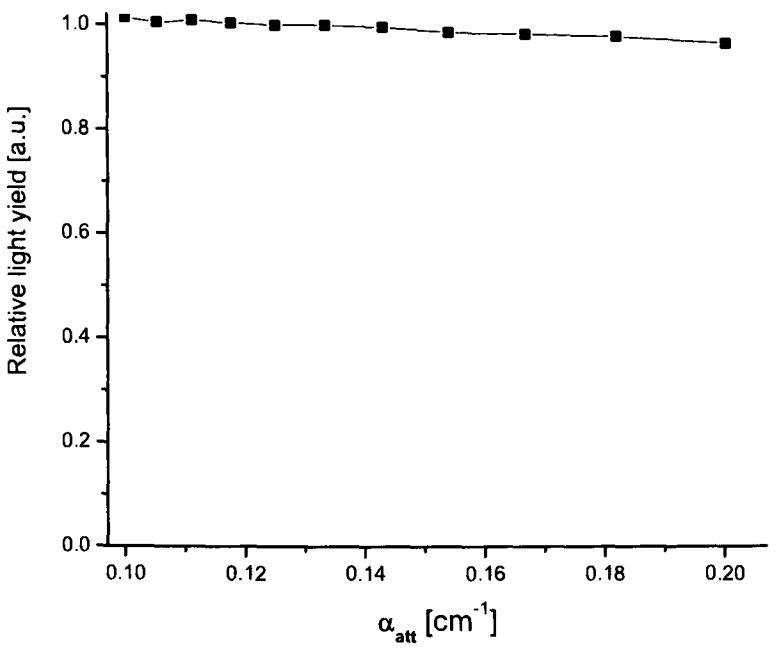

Figure 8.1: *In a standard setup for the measurement of the light yield of scintillators, the collection efficiency is shown to be practically independent of α_{att}. A 20% change in α_{att} produces a change of only 1% in the LY. A weak dependence was required for performing accurate simulations due to the uncertainty in determining α_{att} by experiment*

wider range of α_{att} and crystal size have shown that this holds as long as the typical size of the crystal is much smaller than α_{att}^{-1} (L_{att}). Qualitatively, this can be understood by considering that if the typical distance travelled by photons inside the crystal will be of the order of the size of the crystal. Therefore, if α_{att}^{-1} is much larger than the size of the crystal, relatively large changes in α_{att} will have a small effect on the measured light yield.

Since α_{att} has been shown to be measured sufficiently accurately, only B and N_0 are unknown quantities. Attempts at evaluating N_0 of $CaWO_4$ are frequently reported in the literature and can broadly be divided into two categories. Firstly there are relative measurements [165, 166] used to determine N_0 by comparing the LY with that of a scintillator of known properties such as NaI(Tl). These measurements will not be accurate for $CaWO_4$ unless the difference in refractive index of the reference the materials are taken into account. One also needs to correct for differences in B. However the order of magnitude of N_0 can be estimated in this way, and is reported as ~10000ph/MeV [167].

The second possibility is to perform absolute measurements and try to estimate the correct collection efficiency in order to obtain N_0 [71, 168, 169]. The best way to perform the corrections is by carrying out MC simulations. This means that it is necessary to determine B before determining N_0. Fig. 8.2 shows how the light collection efficiency varies with respect to B. The results indicate that the collection efficiency is affected by B therefore it is not possible to ignore the contributions of scattering. Fig. 8.2 is in itself

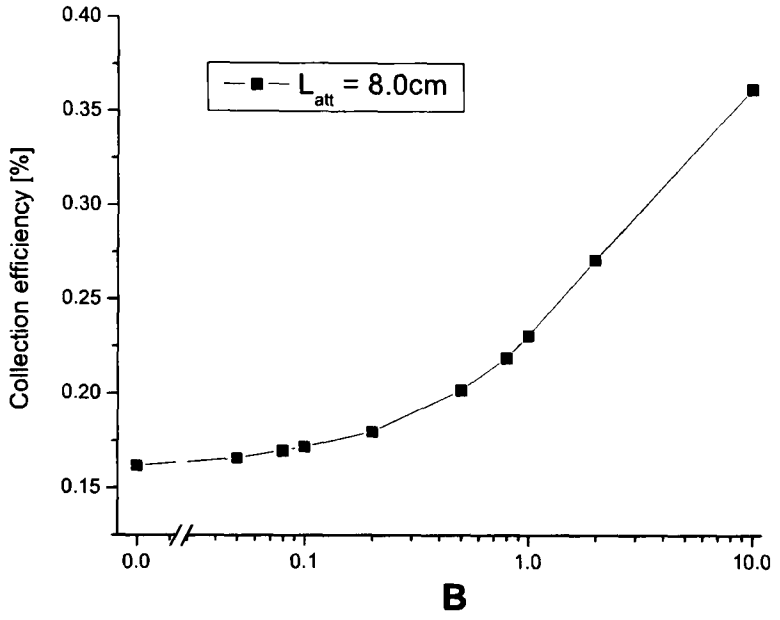

Figure 8.2: *MC calculation of the dependency of the collection efficiency (η) on the scattering to absorption ratio (B)*

a very interesting result which can be summarised as: an increase in the scattering to absorption ratio in crystals will lead to an increase in the light yield. Subsequent studies have shown that decreasing the absorption, or increasing the scattering independently both lead to an increase in LY. The increase in LY with scattering can be understood by considering the distribution in angle of incidence of photons hitting the inside of the crystal face which faces the PMT and leaving the crystal (Ω_S). In a scatter-less crystal (α_{scat}=0), Ω_S is fixed at the production of the photons. Photons which cannot escape toward the PMT in the first reflection will never reach the PMT. In fact some will never exit the crystal from any face and are referred to as "trapped". In a crystal with scat-

tering, a mechanism is present for the direction of the photon to be modified such that a photon which is originally trapped may become un-trapped due to the direction change imparted by the scattering. It follows from this that Ω_S is dependent on B. The next subsection describes how the relationship between B and Ω_S can be used to determine the scattering to absorption ratio.

8.2 Determining B and N_0 by an experiment/MC combination

Applying a liquid or gel in between the crystal and PMT changes the refractive index of the optical contact of the crystal face. This causes a change in the critical angle which affects Ω_S. As Ω_S is changed, the effect that B has on Ω_S is also changed. Hence introducing a material in between the crystal and the PMT provides a handle on estimating the magnitude of B. The ideal "B measuring" experiment will contain only one changing parameter which is the refractive index of the optical contact (n_{gap}). This quantity is easy to control experimentally as the refractive index of optical gels are well known. In terms of the MC simulation, adding a material in between the PMT window and the crystal is equivalent to having n_{gap} as the single variable between experiments. The light yield and collection efficiency are then simply related by $LY = N_0\eta(n_{gap})$. Two experiments a and b can be performed, measuring the LY of the setup with and without a gel. By taking the ratio of LY of these experiments one eliminates any dependency on N_0.

$$\frac{LY^a}{LY^b} = \frac{\eta(n_a, B)}{\eta(n_b, B)} \tag{8.3}$$

Since n_a and n_b are known, the MC collection efficiency and therefore the ratio of light yields depends solely on B. The value of B which makes the MC ratio match the experimental ratio of light yields is the true value of B. Once B is known, one can take any of the two experiments performed and work backward to determine N_0. This is the basic

principle behind the Monte-Carlo refractive index matching (MCRIM) technique. The optical properties of $CaWO_4$ can now be evaluated using this method.

8.2.1 Experimental and MC Setup

To make the MC simulations of the MCRIM setup as accurate as possible, all components which are difficult to simulate are eliminated, i.e. reflectors and unpolished surfaces. The aim is to have an experiment composed only of a source, a crystal and a detector as shown in Fig. 8.3(a). The experiment uses the photon counting electronics and software from the MPCC method. Since only one PMT can be used, the coincidence requirement is removed and spurious events are removed at the software stage. To minimise the effects

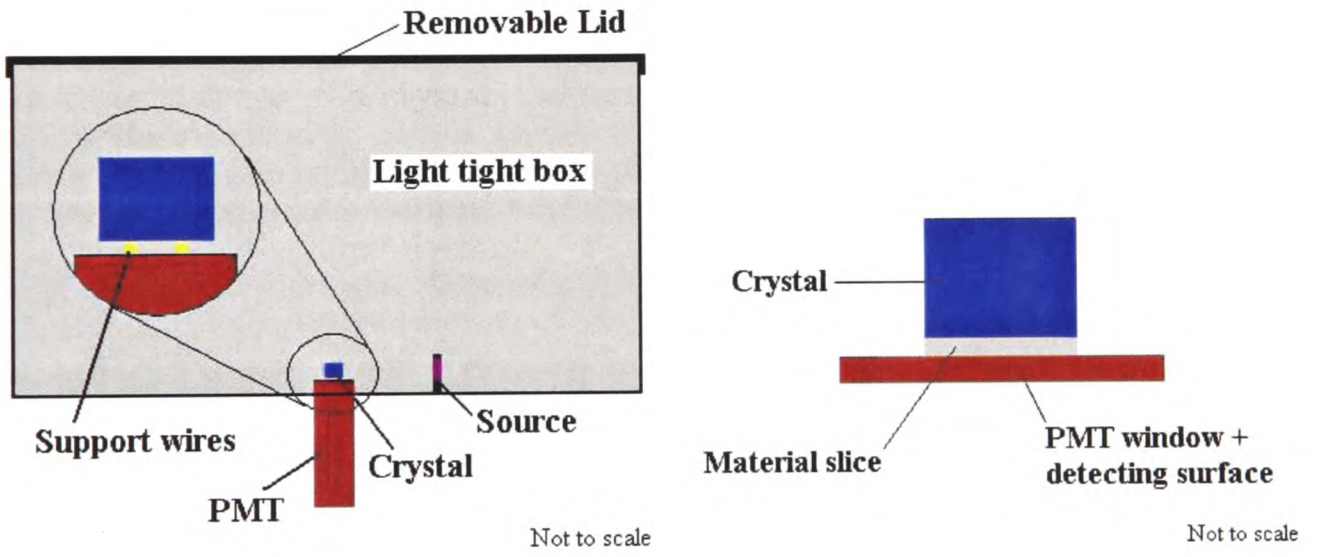

Figure 8.3: *(a) Components of the physical experiment. (b) Components of the MC setup. Photons which exit the crystal in a direction that does not lead to the PMT surface are lost.*

of components which are not optically necessary (PMT shielding, light tight box, source holder) all components are painted black. The light tight box in which the PMT and crystal are placed is made large compared to the size of the crystal. The top and sides of the box are approximately 20cm away from the crystal, making the chance of reflections

from these sides back to the PMT window very small. This means that photons which exit the crystal and are not travelling toward the PMT are not detected. This feature is reproduced by the MC by having totally absorbing surfaces around the setup shown in Fig. 8.3(b). It is worth noting that this setup is completely free of reflectors which increases the reliability of the MC.

In the physical experiment, two supporting wires of thickness 0.05mm are placed on the window of the PMT to serve as the crystal holder. Since these are very thin, it is considered that they do not interfere with the optical properties of the setup and these are not included in the simulations. The support wires were put in place to eliminate any uneven contacts between the crystal and the PMT. The resulting crystal-PMT gap is naturally filled by air, but other transparent materials can also be applied to the space. This provides a mechanism for introducing materials with different refractive indexes whilst controlling their thickness. When results of the MC or the physical experiment are presented, the gap material is indicated by the superscript, for example: LY^{mat}.

The crystal used is the re-polished crystal from chapter 7 of dimensions 10.3x10.0x8.2mm^3. The crystal is placed on the PMT such that the face with largest area is in contact with the PMT. The optical parameters of the crystal need to be entered in the MC. The emission spectrum used is a single Gaussian centred at 430nm with a width of 55nm to match data obtained from luminescence measurements. The values for the refractive index used are 1.98 and 2.00 for the two axes of the crystal.

The wavelength dependent quantum efficiency of the Electron Tubes 9125B PMT is reproduced in the MC. It should be noted that only the normal incident quantum efficiency were available for inclusion. However, as the angular dependence of typical photomultipliers is fairly flat over a large range of angles [170], it is thought that the results should

not be strongly affected by this. The thickness of the PMT window is entered as 1mm and is composed of borosilicate with a refractive index of 1.47. The details of signal amplification such as the gain of the PMT are not simulated. This results in the resolution of the MC PMT being better than that observed in experiments but does not affect the comparison of the average number of photons detected.

8.2.2 Experimental results

When applying gel to the crystal-PMT gap, care has to be taken not to add any in excess. Gel was added to the bottom face of the crystal in a quantity too small to cover the whole crystal-PMT contact. When the crystal is placed in the setup and pushed down, it is easy to estimate how much more is needed to cover the remaining area. The procedure is repeated until the minimum amount of gel needed to cover the surface is present. Fig. 8.4(a) shows a typical background spectrum recorded in the MCRIM setup. Fig. 8.4(b) and (c) shows the measured spectra recorded in photon counting and integrating mode when no additional material is present in the gap. From these results (and a series of other measurements made) the calibration constant of the experiment is determined: one unit as measured in the integrated mode corresponds to 4.47±0.03 photo-electrons. Fig. 8.4(d) shows the spectrum recorded when the gap is filled with Thorlabs G608N refractive index matching gel (n=1.46). The main radiation peak is accompanied by a noise pre-peak, as discussed in section 5.4. The intensity of the noise peak depends on the exact source position and varies between different light yield measurements in between which the source is removed and replaced. Fig. 8.4(d) is presented in integrated form as the number of photons detected would be too large for accurate counting. Henceforth results will be presented using the integrated signal value and then converted to photo-electrons if necessary. Table 8.1 shows a summary of the measurements. The LY due to the 59.5keV γ-rays in the setup with a thin slice of air in between the PMT and crystal is 51.5 photo-electrons. This translates to a light detection efficiency of 870 photo-

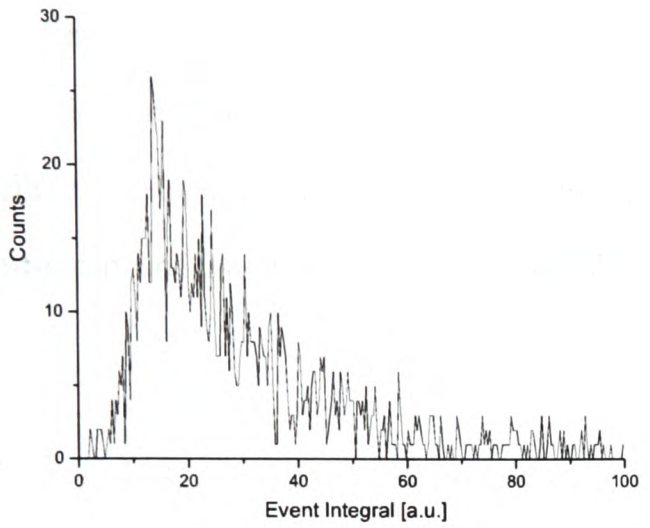

(a)

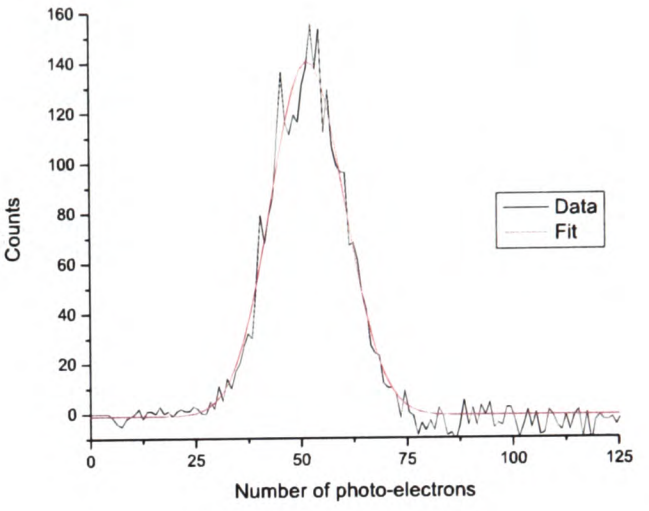

(b)

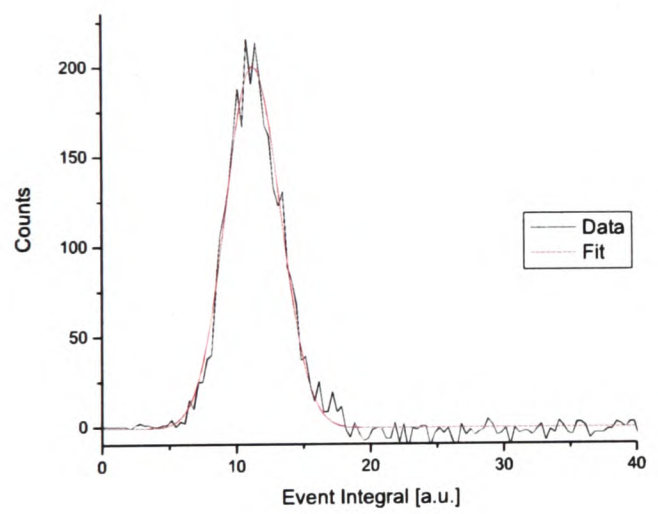

(c)

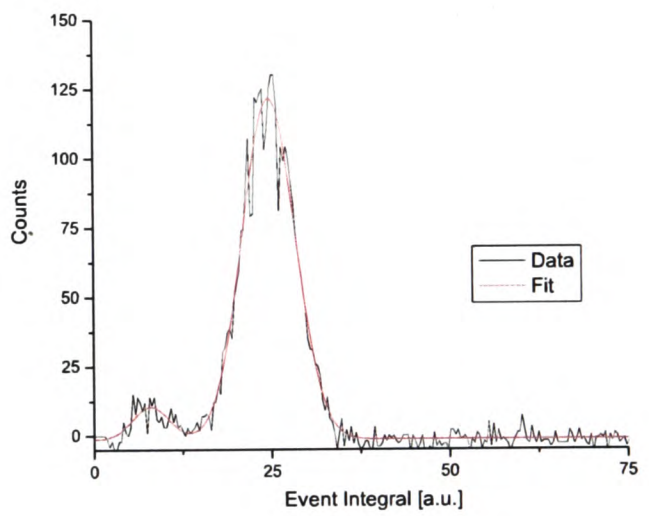

(d)

Figure 8.4: *Typical background corrected spectrum of the number of photo-electrons detected when irradiating $CaWO_4$ with 59.5keV γ-rays of ^{241}Am. (a) Background spectrum for LY^{Air} (b) Photon counting LY^{Air}; (c) Event integration LY^{Air} (d) Event integration LY^{Gel}*

Table 8.1: *Average LY for with the PMT-crystal gap filled by air or gel. The errors quoted are statistical errors obtained from three repetitions of the same measurement. (*) calculated using the calibration constant*

Experiment	LY (integral)	LY [n.p.e]
LY^{Air}	11.5 ± 0.16	51.5 ± 1
LY^{Gel}	24.5 ± 0.20	$110^{*} \pm 1$

electrons/MeV of deposited energy. The ratio between the LY of the experiments with gaps filled by air and gel is 46.9±0.7%. The relative error is of the order of 2% which is sufficiently precise to ensure thorough constraints on B and N_0. The main source of uncertainty is related to the crystal preparation. Whilst every care is taken to wash the crystal as thoroughly as possible repeating the same technique, small variations in the surface cleanliness are expected. Similarly when performing experiments with gel, the amount of gel applied is never exactly the same.

8.2.3 Determination of B and N_0 through MC matching

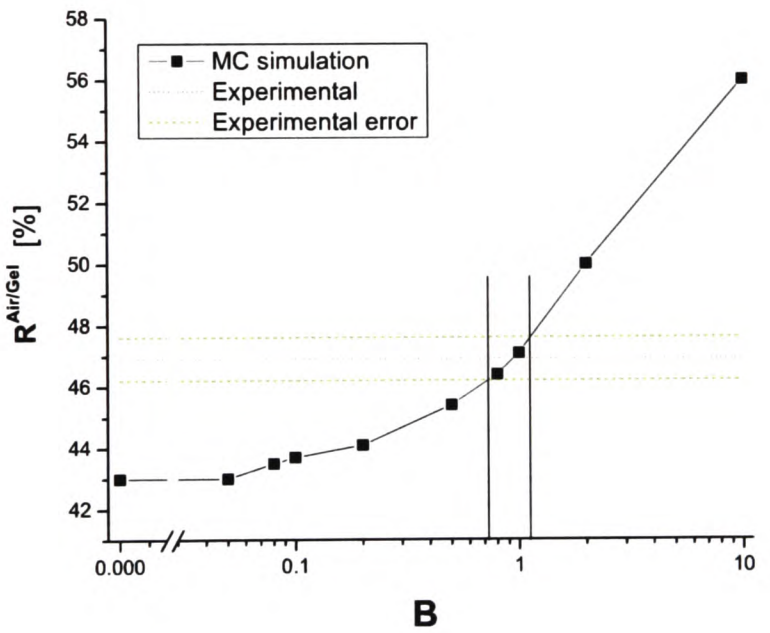

Figure 8.5: *$R^{Air/Gel}$ versus the ratio of scattering to absorption (B). The experimental values ($R^{Air/Gel}$=46.9±0.7%) correspond to a range of B from 0.73 to 1.13. The best value for B is 0.93±0.2*

The simulated ratio of LY ($R^{Air/Gel}$) versus B is plotted in Fig. 8.5. The dotted line shows the measured value (46.9%) and the dashed lines show the experimental errors. The errors correspond to a range of B from 0.73 to 1.13 as shown in the figure. The vertical lines correspond to the range of B bounded by the errors on $R^{Air/Gel}$. The best value for B is given by the mean between the two vertical lines corresponding to B=0.93±0.2.

Since L_{att}=8.0cm this corresponds to values of L_{scat}=16.6±1.6cm and L_{abs}=15.4±1.6cm.

Having determined B, all the parameters needed to calculate the collection efficiency of the setup are known. Knowing the experimental light yield and η, it is possible to deduce the N_0 using equation (8.4).

$$N_0 = \frac{LY^{expt}}{\eta} \tag{8.4}$$

Table 8.2 shows the value of N_0 estimated using LY^{Air}. The true value of N_0 is taken

Table 8.2: *Calculation of the intrinsic light yield of $CaWO_4$ based on the light collection efficiency calculated for LY^{Air}*

B	η	LY^{Air} (expt)	N_0
0.73	$2.16\text{x}10^{-3}$	51.5	23800
1.13	$2.38\text{x}10^{-3}$	51.5	21600

as the mean of the intrinsic light yield calculated using the estimated limits on B. This allows to evaluate the error on N_0. The calculated value of the intrinsic light yield is N_0 = 22700±1100 ph/MeV. It is worth noting that the error is an error on the actual mean intrinsic light yield and not an estimate of the width of the light yield peak.

8.3 Testing the prediction power of the MCRIM technique

8.3.1 Light yield of the setup with the gap filled with water

The hardest aim to achieve for a MC is to predict the LY of a different experiment correctly. For this reason it was decided to test the prediction power of this MC against a setup where the gap is filled with water (n=1.34). The experimental measurements with the gap filled with water are slightly harder to perform as water evaporated from

the gap, precluding long measurements. Excess water causes an increase in the light yield, whilst if the gap is not completely filled a decrease of light yield will ensue. The measurement time using water is reduced to 5 minutes to avoid evaporation. At first, extra water is added such that water covers a large area of the PMT window and some of the vertical sides of the crystal. Every 5 minutes, the status of the water level is checked and a new measurement is taken. Runs are taken until the water no longer completely fills the gap between the crystal and the PMT which can be easily assessed by visual inspection. This last measurement is discarded and the previous measurement is used as the one where the "correct" amount of water is present. Studies have demonstrated that a failure to consider the presence of excess water can lead to results with a LY 20% superior to that recorded using the method described above. The error estimated by repeating measurements three times ($\sim$ 1.5%, see below) remains comparable to those when the gap is filled with air or gel, hence demonstrating the robustness of this procedure. The MC simulations were run with the input parameters determined from the air and gel measurements. The predicted light yield in integrated units is 21.0 ± 0.05 to be compared with a measured value of 21.1 ± 0.3 (see Fig. 8.6). As can be seen from the figure, the predicted and measured peak position coincide within the errors of the experiment and the simulation. The resolution estimated by the MC is significantly better than that obtained in the experiment. The main contributions to the width of the peak are the light yield non-proportionality and the statistical fluctuations on the number of photons lost in each run. Other factors such as the Fano factor [171] play a comparatively small role and are not included. A factor which is not included which contributes to the broadening of the peak is the details of detection of the PMT. PMTs are known to cause a statistical broadening of the resolution due to the use of a dynode chain for the signal amplification (for a good example of this see [71]). As already discussed, Litrani does not contain routines for the detailed simulation of PMTs, so the effects could not be included. The exact match between the peak position prediction and the subsequent measurements confirms the validity of the input parameters determined as well as providing a confirmation of the

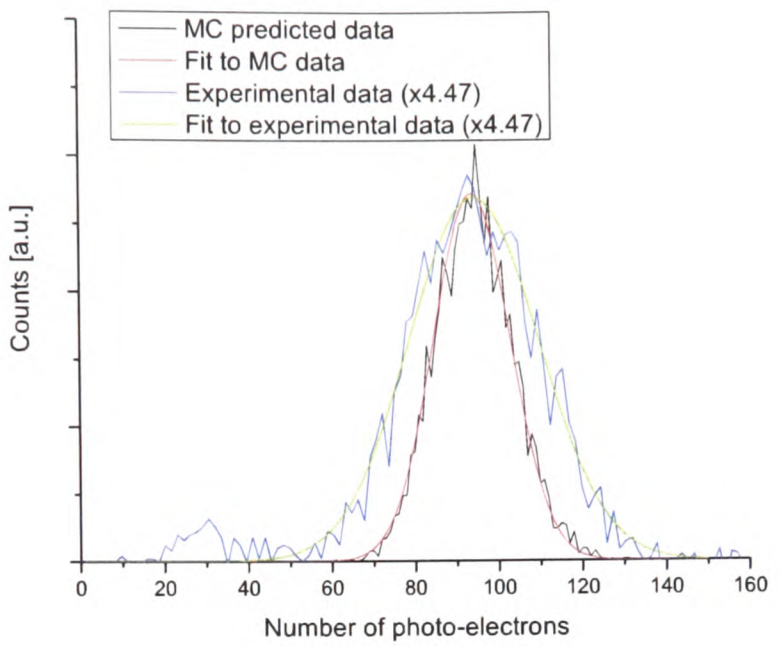

Figure 8.6: *Measured and predicted spectrum of $CaWO_4$ in the setup with the crystal-PMT gap filled with water. The MC data is converted from integrated spectrum to number of photo-electrons using the calculated conversion coefficient of 4.47*

validity of the MCRIM method.

8.3.2 Further tests of the MCRIM technique

To test the input parameters even more thoroughly, a comparison of simulation with a published experiment was performed. The experiment [172] was chosen as it used a crystal cut from the same ingot as the MCRIM reference crystal. The optical properties of the crystal are therefore assumed to be the same as the properties of the MCRIM cyrstal. The setup is comprised of a PMT of characteristics similar to those of XP2020Q and the crystal has dimensions 10x10x8mm^3. The crystal is less well polished than the MCRIM reference crystal as the latter had extra polishing work carried out on top of producer polish. The crystal in this second setup is wrapped in Teflon tape. As was previously mentioned, it is notoriously difficult to simulate the propagation of photons off reflectors. However a reasonable prediction of the light yield of a simple setup should be obtainable with approximated reflector properties. The Teflon tape was roughly simulated as be-

ing 99% reflective. The reflectivity was deliberately chosen as being high so that a low predicted light yield cannot be attributed to the choice of parameters for the reflector. Out of the reflected photons, 95% are reflected diffusely and 5% are reflected via specular reflections. Since the published experiment was performed using ^{137}Cs, the intrinsic light yield must be corrected for non-proportionality effects, and light yield for the MC is N_0=24000ph/MeV. The results of the experiment and predicted LY of the MC are shown in Table 8.3. The non-perfect polish of the crystal used in this experiment causes

Table 8.3: *Predicted values of the intrinsic light yield when comparing to NaI(Tl).*

	photo-electrons/MeV	N_0^{MC}	N_0^{rel}
Experiment	4400±200	n/a	14200
Prediction	3900	24000	12600

an increase in the light yield compared to what would be expected for a well polished crystal. The MC simulation predicts a measured light yield of 3900photo-electrons/MeV, which given the fact that the MC assumes perfect polish is in good agreement with the observed value. This indicates that the input parameters of the MC correspond to the properties of the crystal.

Having ensured the validity of the input parameters, it is possible to evaluate how well standard techniques used to obtain N_0 perform by comparing the "true" intrinsic light yield (N_0^{MC}) with the intrinsic light yield calculated by standard techniques (N_0^{rel}). A standard technique used to estimate the intrinsic light yield of a crystal placed in a experiment is to compare the measured light yield to that of an NaI(Tl) crystal in the same setup [165]. The relative measured light yield is used to calculate the relative instrinsic light yield (N_0^{rel}) under the assumption that the N_0 of NaI(Tl) is well known. For the $CaWO_4$ in [172], the comparative method is used to obtain N_0^{rel} = 14200±1400ph/MeV for radiation of 662keV. Using the same method for the predicted measured light yield leads to an estimate of the intrinsic light yield of N_0^{rel} = 12600, 40% lower than the input

value for the MC. This is thought to be a consequence of not fully taking into account the differences in the materials compared in terms of the refractive indexes which can only be done by MC. This confirms the utility of the MCRIM technique for the determination of input parameters for MC using HIS. The following sections presents a couple of studies aimed at understanding the properties and applicability of the MCRIM technique.

8.4 Conclusions

Simulating light collection in HIS has always been problematic due to the difficulty of obtaining good input parameters. In particular, evaluating the intrinsic light yield of HIS proves difficult due to their high refractive index. To complicate the matters further, the light collection efficiency is dependent on the sample quality and in particular on the scattering present in the crystal [173, 174]. It is shown in this paper that a higher scattering coefficient leads to a higher light collection efficiency. A consequence of this is that simulating light transport in scattering crystals requires to evaluate α_{scat}. A new method has been developed determine these parameters in HIS called the Monte-Carlo Refractive Index Matching technique (MCRIM). The MCRIM method uses a combination of MC simulations and experimental measurements to determine the ratio of scattering to absorption coefficients (B) and the intrinsic light yield (N_0). A minimalist experimental setup is used which was designed to eliminate uncertainties due to reflectors, uneven contacts and de-polished surfaces. A small, well polished and regular shaped crystal is placed on a PMT such that a small gap of controlled thickness is left between the bottom crystal face and the PMT window. Introducing transparent materials of different refractive index in the gap causes a change in the LY which can only be reproduced by simulations which have a unique set of B and N_0 as input parameters. The MCRIM technique was tested on a $CaWO_4$ crystal and the best estimate of its intrinsic light yield is N_0=22700$\pm$1100, and B=0.93$\pm$0.2 that translates into absorption coefficients of α_{scat}= 0.061$\pm$0.017cm^{-1} and α_{abs} = 0.065$\pm$0.018cm^{-1} respectively. In the MCRIM reference crystal, scattering

and absorption play approximately equal roles in attenuation processes. This highlights the importance of considering scattering processes when looking at the LY of HIS.

Using the input parameters obtained with the MCRIM technique; the light yield of two different experiments was successfully predicted. The fact that MC simulations can be used to predict the light yield of experiments indicates that the parameters calculated using the MCRIM technique are accurate. Furthermore, the ability to successfully calculate the LY of crystals submitted to radiation is a stringent test on the exactitude of a MC simulation. It has been demonstrated that the Litrani code fulfils the prediction requirement under the condition that reflectors and de-polished surfaces are not included.

It has also been shown that traditional methods of evaluating the intrinsic light yield of HIS result in an underestimation of N_0. The MCRIM technique is simple enough to be adapted to measure the scattering, absorption and intrinsic light yield for a range of crystal shapes and sizes, making it a promising tool for the optimisation of scintillation setups for a wide range of applications including medical and laser physics. Furthermore, the MCRIM technique increases the reliability of predictions for setups containing crystals of shapes and sizes that cannot easily be optimised by physical experiments due to time or cost constraints.

Chapter 9

MC simulations of light collection in CRESST crystals

The previous chapters have focused on obtaining realistic input parameters in order to have the tools to perform accurate MC simulations. This required dedicated studies, as for $CaWO_4$ (and HIS in general) the input parameters were poorly understood. For the first time, all the necessary optical and luminescence properties of a scintillator have been measured. Though the properties of each crystal are different, the studies determined realistic values for all input parameters necessary for simulations. MC simulations are a tool to optimise the collection efficiency and explore the light collection properties of CRESST crystals with particular focus on the homogeneity. Studies of how the geometry of the CRESST modules affects the light yield are presented. Finally, an estimation of the correlation between the phonon and light signals is presented.

9.1 MCRIM on the CRESST reference crystal Boris

The light yield test facility at MPI (Munich) has been used to measure the light yield of a number of CRESST crystals [38] relative to a reference crystal "Boris". The Munich setup is not a photon counting setup and hence the MCRIM technique cannot be used to determine the intrinsic light yield of crystals. However, only relative measurements are

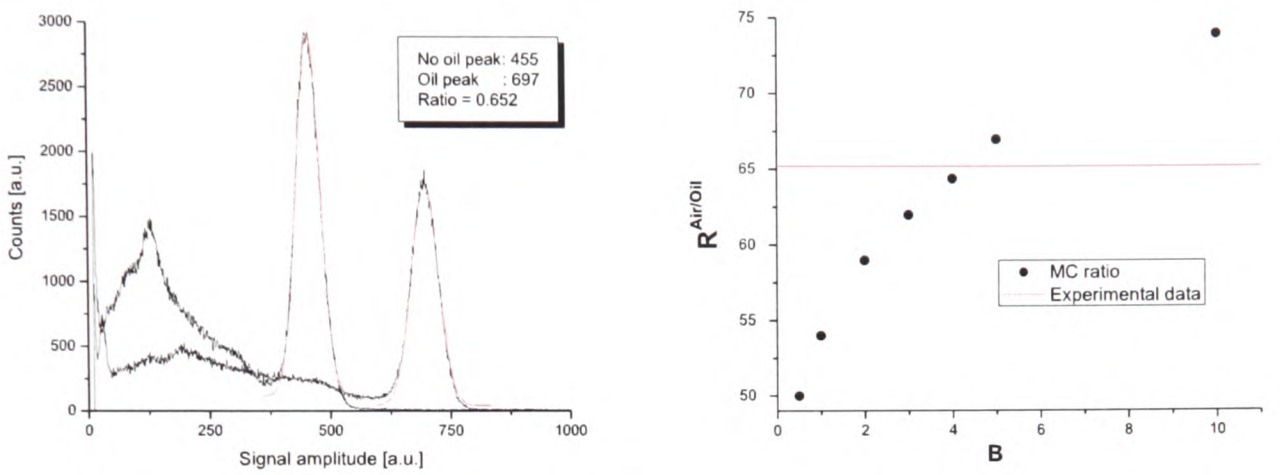

(a) (b)

Figure 9.1: *Light yield and MCRIM measurements performed on the CRESST reference crystal Boris using ^{137}Cs. (a) Experimental measurements with air and optical contact oil n=1.5 (b) Determination of scattering to absorption ratio B=4.3*

needed in order to evaluate the scattering to absorption coefficient ratio B. Fig. 9.1(a) shows the measured event amplitude for Boris irradiated by ^{137}Cs, with air and gel (n=1.5) filling the gap between the crystal and the PMT window (performed by Jelena Ninković). Fig. 9.1(b) shows the results of the simulations to determine B, which give a result of B=4.3. Boris is used as the CRESST reference crystal since the measured light yield of this crystal was the highest among the first batch of crystal tested for CRESST. The high value of scattering indicates that this relatively high light yield is at least partly due to a high scattering to absorption ratio. This measurement also serves to show the wide range of scattering to absorption that can be expected for CRESST scintillators. As a result of this, in the following sections where the light collection properties of low temperature CRESST modules are studied, results are presented for crystals with high and low values of B.

9.2 Low temperature MC studies of the CRESST setup

9.2.1 Elements of the MC

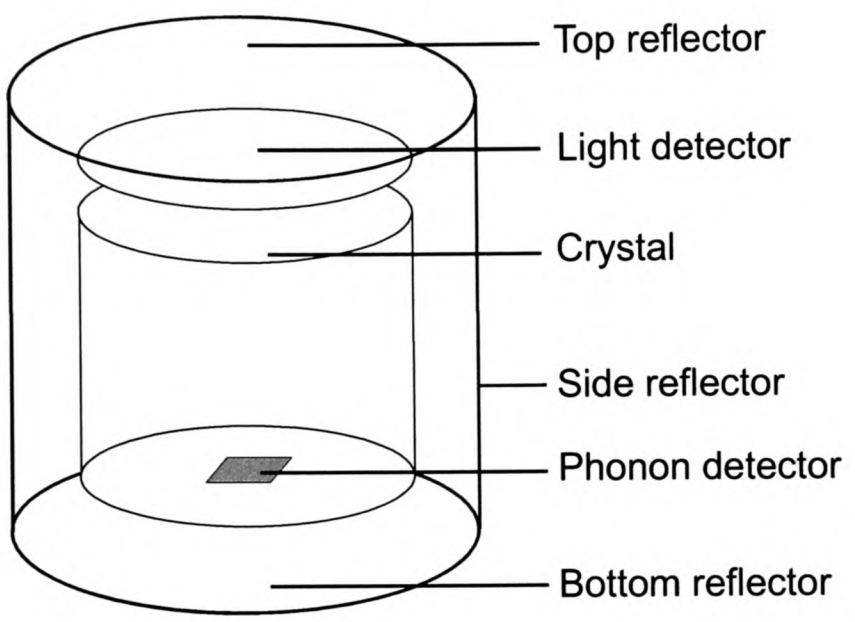

Figure 9.2: *Components of the CRESST setup simulated in the MC*

Fig. 9.2 shows the components of the CRESST setup which are simulated in the MC. The $CaWO_4$ crystal is given the optical properties of the MCRIM reference crystal: n_o = 1.98, n_e=2.0 and α_{att}=0.126cm^{-1}. The value of B is 1.0, unless specified otherwise. The room temperature light yield of 22700±1700ph/MeV at energies of 59.5keV is corrected for the increase in light yield observed at low temperatures. In chapter 6, it was measured that the light yield increases by a factor of approximately 1.5 and thus to simulate low temperatures N_0=34100ph/MeV is used. The emission spectrum of $CaWO_4$ is approximated to a single Gaussian centred at 430nm with a FWHM of 25nm. The crystal is cylindrical with dimensions ⌀40x40mm. The phonon detector (a thin film of tungsten) is placed in optical contact with the crystal and is a square with sides=3.0mm and thickness 200nm. The refractive index of the tungsten is entered as a wavelength dependent function with n=1.47 at the peak emission of $CaWO_4$ [175]. The wavelength dependent absorption length is taken from the same reference. The light detector is placed 4.5mm

above the crystal. It is constructed of pure silicon, with a wavelength refractive index which has a value of 2.2 at the peak emission of $CaWO_4$ [176]. The absorption length of silicon is taken from the same reference. The light detector used in the standard MC setup is a square with dimensions side=30mm, thickness=0.4mm (in the diagram this is shown as a circular ⌀40mm light detector, as this will be the future design for CRESST modules). The bottom reflector is placed 5.5mm from the crystal surface, the top reflector is placed 5.0mm from the light detector and the side reflector is 4.9mm from the curved crystal surface. The setup is such that no light can escape the volume bound by the reflectors. The reflectors are 98% reflective of which 98% is specularly reflected. This is a fairly close match to the multilayered polymer reflectors used for CRESST [177]. These parameters completely describe the standard MC setup and any variations to this will be indicated where necessary.

9.2.2 Collection homogeneity in the CRESST detectors

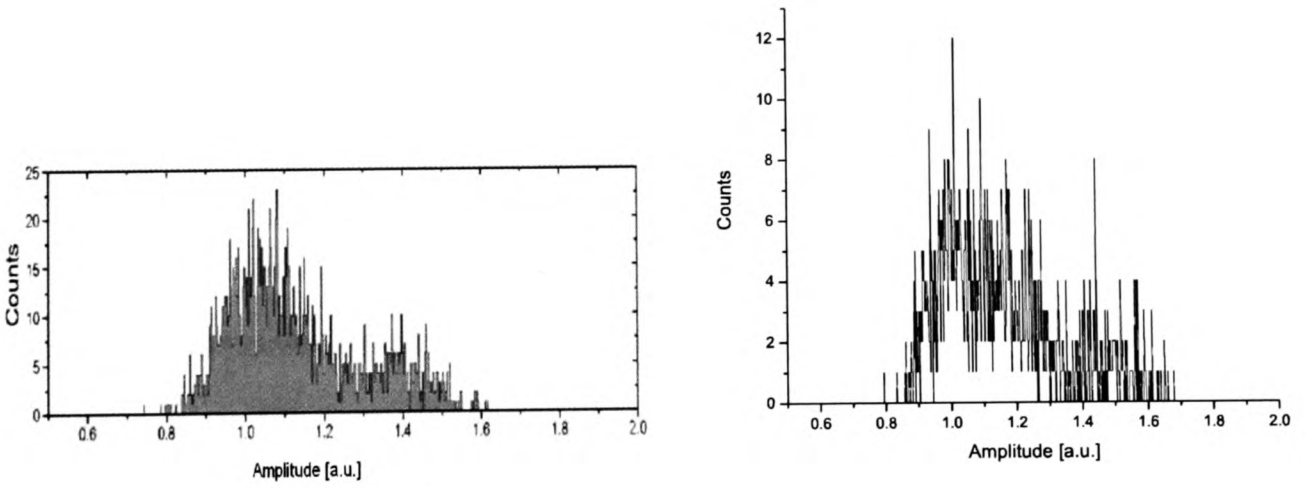

(a) (b)

Figure 9.3: *(a) 122 keV signal from a ^{57}Co spectrum in a polished CRESST crystal [178] (b) MC simulation of ^{57}Co spectrum which reproduces the observed double peak structure*

The first use for the MC will be to understand the light collection properties of the CRESST modules. At millikelvin temperatures, the light signal due to the 122keV line

of a ^{57}Co source in a polished CRESST $CaWO_4$ crystal is reported to be composed of two distinct bands [178] which is shown in Fig. 9.3(a). It is worth emphasising that the double structure is due to the 122keV line only (measured using the phonon channel) and is not a contribution from 136keV γ-rays. Fig. 9.3(b) shows how the Litrani MC reproduces this double peak structure. The double peak structure can be explained when

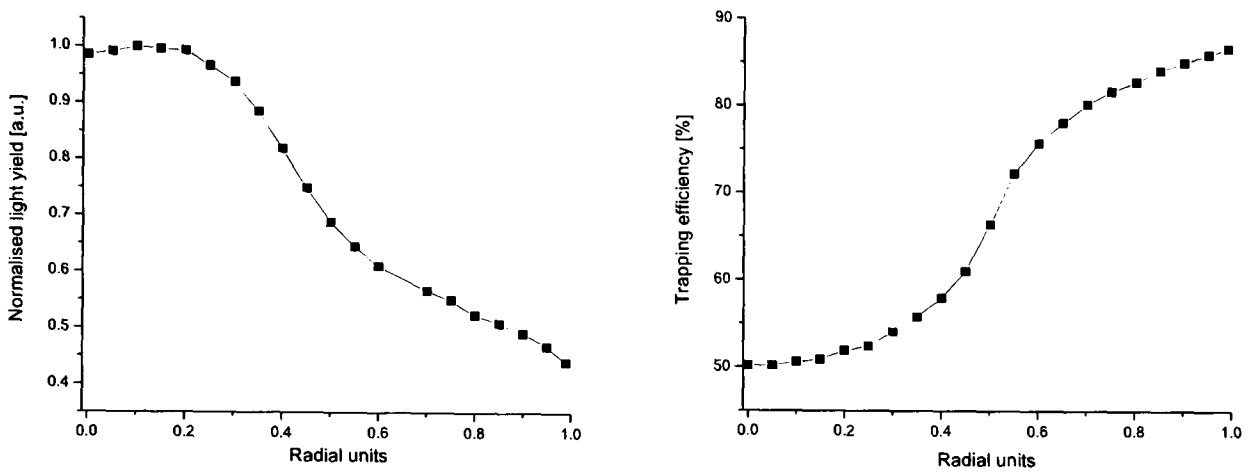

(a) (b)

Figure 9.4: *(a) Simulated collection efficiency versus radial position of energy deposition. (b) Trapping efficiency calculated using equation (9.1)*

one considers the non-homogeneity of the collection efficiency in the CRESST setup. In order to investigate the position dependence of the collection efficiency, light is generated at fixed points inside the crystal as opposed to being generated by the simulation of particle interactions. Fig. 9.4(a) shows how the light collection efficiency varies with the radial position of the crystal (ρ=0 is the crystal centre, ρ=1 is the crystal edge). The simulations were performed along the central vertical plane of the crystal. To ease the comparison with analytic calculations, the simulations were performed with B=0.01 (very low scattering). In the absence of scattering, a cylindrical crystal can be viewed as a large optical fibre. It can be shown that in 3D, photons are trapped if they fulfill the following

conditions [179, 180]:

$$sin(\beta) > sin(\phi)(1 - \rho^2 sin^2(\theta))^{1/2} \tag{9.1}$$

where β is the complement of the critical angle. The radial position at which the photon is generated is ρ, the polar angle is ϕ (measured against the length of the fibre) and θ is the azimuthal angle of the beam of photons being considered. Fig. 9.4(b) shows the proportion of light trapped as a function of radial position for an infinitely long fibre of material with a refractive index of 2.0. The optic-fibre model demonstrates that the light collection inhomogeneity in CRESST is caused by photon trapping by the curved faces. This implies that a significant proportion of light collected exits the crystal through the curved face. Otherwise, it would not be possible to explain why a decrease in the light yield is observed toward the curved edge of the crystal. The sharp transition in trapping efficiency between ρ=0.4 and ρ=0.6 explains why the ^{57}Co spectrum is composed of two peaks as opposed to one broad band. This double peak effect is also observed for crystals with higher values of B, though the position dependence becomes less pronounced as the scattering eliminates trapped modes. Fig. 9.5 shows the light collection inhomogeneity

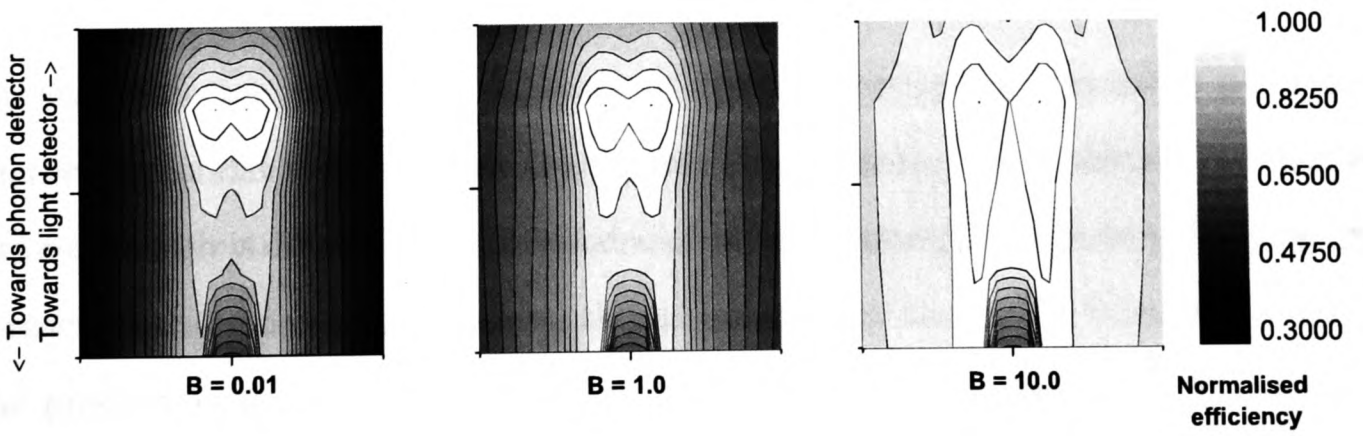

Figure 9.5: *L_{att}=8.0 The figures are normalised to the maximum number of photons collected for each value of B.*

in CRESST crystals with different scattering to absorption ratios. Looking first at the

crystal with B=0.01 one can see that the radial position dependence is present throughout the whole crystal. Apart from the now understood horizontal inhomogeneity, the light yield collection varies with the vertical position of the origin of the photons. Two main features are observed. The phonon detector is also a good photon absorber and as it is in contact with the bottom of the crystals (see Fig. 9.2) it will also absorb some of the light. The phonon detector represents a larger solid angle for photons which are generated at the centre and bottom of the crystal, causing a loss of light collection efficiency for light produced in that zone.

The second feature is a reduction in the collection efficiency for photons produced close

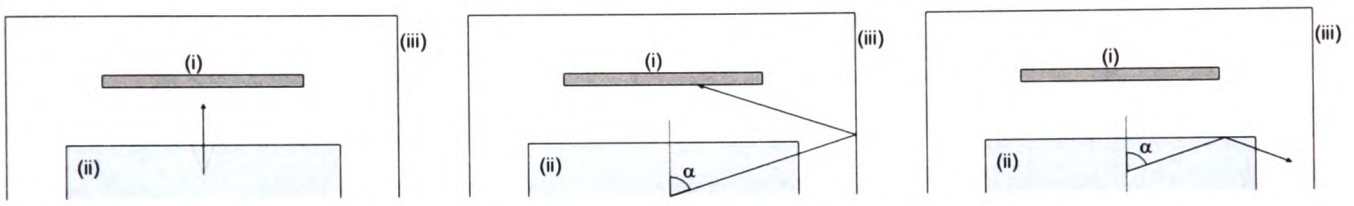

Figure 9.6: *Labels: (i) Light detector; (ii) Crystal; (iii) Standard reflector; Figures: (a) Non-trapped light cone delimited by the critical angle for total internal reflections; (b) Light ray exiting from side of crystal; (c) Light ray reflected by top face. α is greater than the critical angle.*

to the light detector. If a photon is produced with a direction that lies inside the escape cone, then it can exit the crystal via the top face (Fig. 9.6(a)). 13% of photons are emitted in the cone which is defined by the critical angle of the crystal/air boundary. Photons can also reach the light detector by exiting the crystal through the curved faces (Fig. 9.6(b)). If the production point of the photons is too close to the top face of the crystal, then photons produced in the same direction as in Fig. 9.6(b) will be reflected away from the detector and hence are much less likely to be detected (Fig. 9.6(c)). This explains the decrease in the light collection efficiency observed at the top of the crystal. The same trends are observed in medium (B=1.0) and high (B=10.0) scattering crystals, albeit less clearly. In general the higher the scattering to absorption ratio of the crystal, the more

homogeneous the collection efficiency of the crystal.

9.2.3 Effect of the optical axis orientation on the light yield

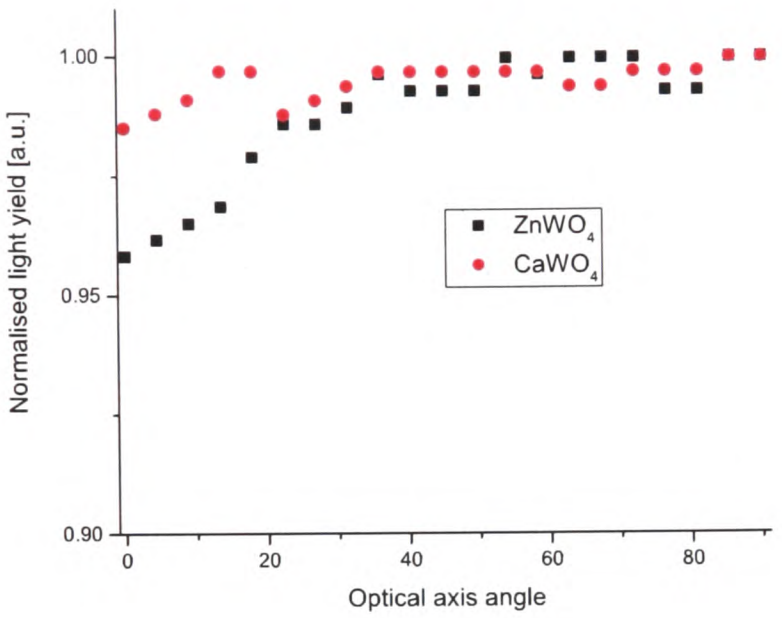

Figure 9.7: *Influence of the orientation of the optical axis on the light collection efficiency of setups comprising $CaWO_4$ and $ZnWO_4$ like crystals. The optical axis angle is measured with respect to the vertical axis of the setup.*

MC simulations are particularly useful to simulate experiments that would be time consuming, costly and difficult to perform. For example, experiments to determine how the light yield depends on the orientation of the principle optical axis would require the production of numerous crystals. This is a costly exercise but can be readily simulated using Litrani. Fig. 9.7 shows how the collection efficiency of the CRESST setup is modified according to the direction of the optical axis of the crystal. The optical axis angle θ is measured against the vertical axis of the crystal. Currently, CRESST $CaWO_4$ crystals are grown with θ=0 or θ=17°. MC simulations offer the opportunity to test the effect of varying the optical inclination for a variety of crystals. Two crystals are considered, a weakly birefringent crystal with the properties of $CaWO_4$ (Δn=0.02), and another with high birefringence based on the refractive index of $ZnWO_4$ (Δn=0.17 [181]). In the case

of $CaWO_4$, the orientation of the optical axis produces little difference on the collection efficiency. However in the case of $ZnWO_4$, inclining the optical axis by 45^o or more leads to an increase in detected light of the order of 5%. Optimising the crystal properties is not the only way to increase the light yield. The geometry of the setup, and in particular the placement of the reflectors and detectors can also be optimised.

9.2.4 Effect of the position and reflectivity of the side reflector on the light collection efficiency.

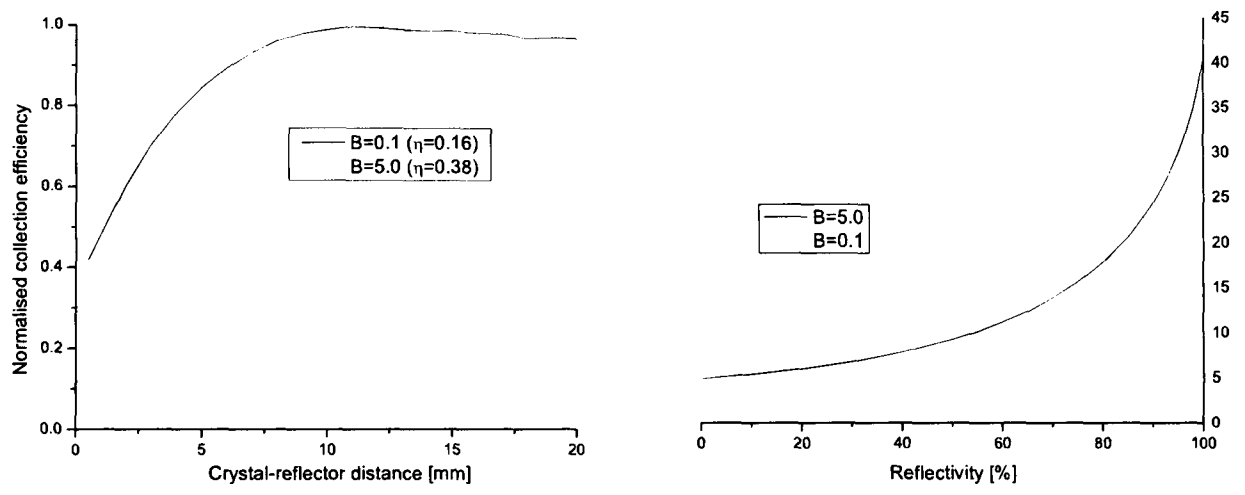

(a) (b)

Figure 9.8: *Effect of the side reflector properties on the LY. (a) Position of the side reflector. (b) Reflection properties of the side reflector.*

The results on the collection homogeneity indicate that a significant proportion of light detected leaves the crystal from the curved faces. To reach the light detector, photons which exit the curved face of a crystal must be redirected toward the detector by a reflector. The properties of the reflector will be one of the main factors affecting the light collection efficiency. The position of the reflector will determine what proportion of side escaping light re-enters the crystal and how much is reflected toward the detector. Fig. 9.8(a) shows how the position of the side reflector affects the light collection efficiency for crys-

tals with high and low scattering. As can be seen, a gain in the detected light of between 10-20% can be obtained by moving the side reflector out from 5.0mm (standard setup) to 10mm. By moving out the reflectors, one decreases the chance of "side" escaping light re-entering the crystal. Due to the high refractive index of $CaWO_4$, light produced at an angle such that it can escape by the cylindrical side face is necessarily totally internally reflected by the flat faces. Therefore re-entering light would be reflected away from the detector by the flat face leading to an increased probability of it being lost. This is why moving the reflectors out increases the amount of light detected in the standard setup.

Fig. 9.8(b) shows how the light collection efficiency is affected by the average reflectivity of the reflector. A typical reflector is approximately 90-99% reflective, depending among others on the wavelength of the incident light. In this range, a small increase in reflectivity leads to a large increase in the amount of light collected by the CRESST modules. Apart from highlighting the importance of implementing high quality reflectors, this result also has implications for the choice of CPSD scintillators. In general, reflectors perform better for lower energy photons (red to green) than for the higher energy range of visible light (blue). Since a small decrease in the reflectivity causes a large decrease in the collection efficiency, scintillators with a lower average emission energy will be better suited for use in a CPSD setup with "classical" reflectors. This offers further support for the implementation of $ZnWO_4$ (green emission) as it is a better matched for reflectors than the blue emission of $CaWO_4$. Apart from the reflectivity of the reflector, another factor that influences the light yield is the "type" of reflection light undergoes. There are basically two possible reflections, specular (mirror like) and diffuse (paint like). Studies were performed with all the reflectors transformed from specular reflectors (as in the standard setup) to partially diffuse reflectors. It was found that the light collection efficiency did not depend strongly on the reflector type, with a maximal 5% increase in light yield obtained for 30% diffusive reflectors. The reflection properties are not the only way of improving the light yield.

9.2.5 Effect of the shape and size of the light detector on the photon collection efficiency

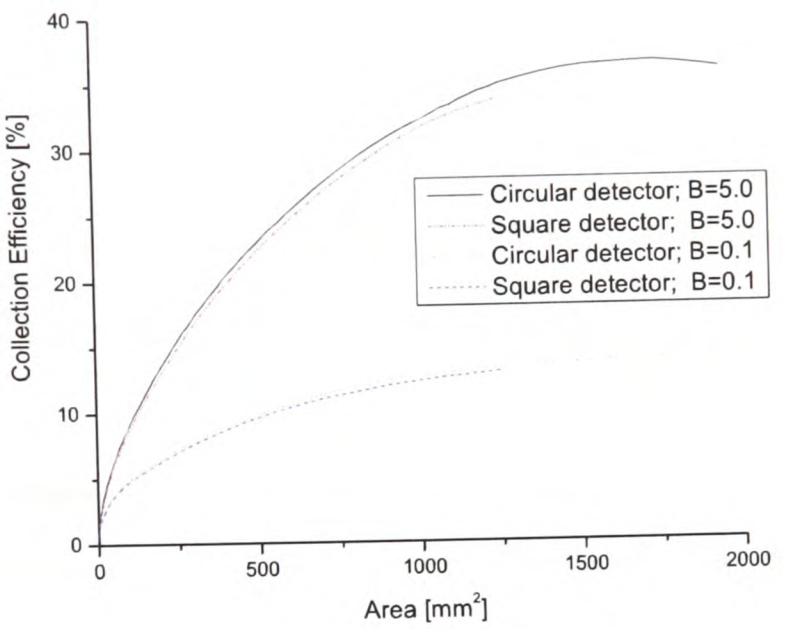

Figure 9.9: *Correlation between the area of the detector and the light yield detected. Results are presented for square and circular detector shapes for crystals with B=0.1 and B=5.0*

Two shapes of light detectors have been proposed for CRESST; square and circular. Having a square shape presents an advantage in terms of ease of holding the light detector whilst a circular detector matches the symmetry of the setup more closely. Investigations were carried out to look at how the light collection efficiency is affected by the shape and size of the detector. Fig. 9.9 shows that the light yield is hardly affected by the shape of detector used. The general trend is that the larger the area, the more light collected. The MC predicts that the light yield for an 800mm^2 detector will be between 0.8 and 0.9 of the light yield observed for a detector of 1800mm^2 depending on the scattering to absorption ratio. This agrees very well with results measured by the CRESST group [124] which reports a measured relative light yield of 0.88

Increasing the surface area of the detector past 1800mm^2 can be seen to cause a reduction of light yield. This is due to photons exiting from the side of the crystal being reflected away rather than being detected by the extra surface area of the detector. The MC only

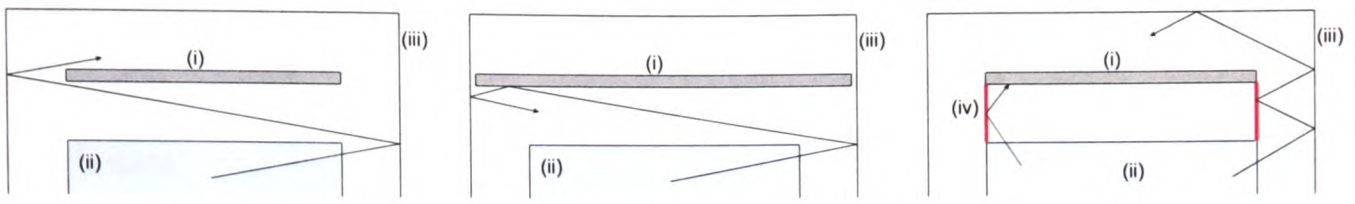

(a) (b) (c)

Figure 9.10: *Labels: (i) Light detector; (ii) Crystal; (iii) Standard reflector; (iv) Additional reflector. (a) Detector of normal size allowing light to pass to the back of the detector; (b) The same ray as in "a" being reflected by the detector surface; (c) A modified setup with an extra reflector guiding light to the back of the detector.*

allows for polished surface to be considered, which means that the high refractive index (n$\sim$2.0) of silicon causes it to have a very high reflectivity. The light which is hitting the extra surface area of the detector would have normally continued to the back of the detector (Fig. 9.10(a)). Once at the back, it is difficult for the light to escape and it will undergo many reflections, among others on the back side of the detector, increasing its probability of being detected. Instead of this, the increased surface area causes a high proportion of these photons to be reflected back into the crystal, reducing their chance of eventually being detected (Fig. 9.10(b)). Given this, a modified setup is proposed for a setup with a circular detector. A reflector is introduced to separate the light that exits from the side from the light that exits from the top of the crystal. The reflector has a circumference the same as that of the crystal and the light detector ($\oslash$40mm) and stretches the length of the gap between the crystal and the detector (4.5mm). To decrease the number of reflections undergone by the light with the top reflector, this reflector is made from a 98% diffusing reflector (Teflon for example). The setup was investigated for two crystals of scattering B=0.1 and B=5.0, resulting in an increase in the light collection efficiency of 17% and 9% respectively. The above example illustrates the power for investigating ways of increasing the light collection efficiency in HIS modules. By regrouping the individual studies, the light collection efficiency of CRESST modules could be increased by close to 30%. This result will be particularly important when considering

the future design of rare event search modules. The MC simulations presented can also help to understand the correlation between the phonon and light signals observed in the CRESST data.

9.3 Prediction of the light and phonon signal correlation

The aim of this section is to use MC simulations to investigate how energy is detected in the CRESST modules. The energy deposited in a scintillator by a particle (E_{dep}) is either converted to light (E_L) or to phonons (E_P). There are no other mechanisms which take place which means that by conservation of energy:

$$E_{dep} = E_L + E_P \tag{9.2}$$

The proportion of energy converted to light depends on the intrinsic light yield, and on the average photon energy of the emitted light ν_0. The intrinsic light yield is also a function of the deposited energy due and hence $E_L = N_0(E_{dep})\nu_0$. There are four solutions to the fate of each photons produced.(a) the photon is absorbed in the phonon detector, (b) the photon is re-absorbed in the crystal, (c) the photon is absorbed in external components such as reflectors or holders; (d) the photon is detected in the light detector. Therefore the energy detected in the light detector is given by:

$$D_L = E_L(1 - a - b - c) = dE_L \tag{9.3}$$

where a is the proportion of photons detected in the phonon detector, b is the proportion of photons reabsorbed in the crystal, c is the proportion externally absorbed and d is the proportions detected in the light detector.

Energy produced as phonons is not completely detected in the phonon detector either. There are competing processes where a proportion ϵ thermalise in the phonon detector and (1-ϵ) thermalise in the crystal. The value of ϵ is different for each phonon detector but is limited to the range 0.5 to 0.8 [182]. The energy detected in the phonon calorimeter D_P is then given by $D_P = \epsilon E_P$. The photons that are reabsorbed in the crystal produce phonons which also thermalise in the phonon detector with probability ϵ. A final contribution comes from photons which are absorbed directly in the phonon detectors. The energy due to these photons is detected completely by the phonon detector and hence the total expression for the energy deposited in the phonon channel is:

$$D_P = \epsilon(E_{dep} - E_L) + \epsilon b E_L + a E_L \tag{9.4}$$

CRESST II and future CPSD experiments will use the ratio of the light signal to phonon signal to reject electron recoil pulses. The expression for the ratio of the light to phonon signals is shown below (assuming the signals are proportional to the energy deposited):

$$\frac{D_L}{D_P} = \frac{dE_L}{\epsilon(E_{dep} - (1-b)E_L) + aE_L} \tag{9.5}$$

Using MC simulations, the factors, a, b, c and d can be evaluated. Fig. 9.11 shows the typical fate of photons in the standard CRESST MC setup with a ⌀40mm light detector when irradiated with a ^{57}Co source. One can immediately recognise the double peak structure due to the light collection inhomogeneity with respect to the radial position of photon generation (curve (1)). As could be expected, the same double structure is observed in the amount of light lost in the reflectors (curve (4)). Apart from horizontal inhomogeneities, the effect of having photons produced close to the phonon detector is clearly visible in curves (2)' and (3)'. Fig. 9.11 indicates that approximately 18% of the photons are detected in the light detector, 2% are detected in the phonon detector, 5% are lost in the reflector and 75% are lost in the crystal. Overall, 82% of the produced photons are lost either in the crystal or in the reflector. This leaves a clear scope for

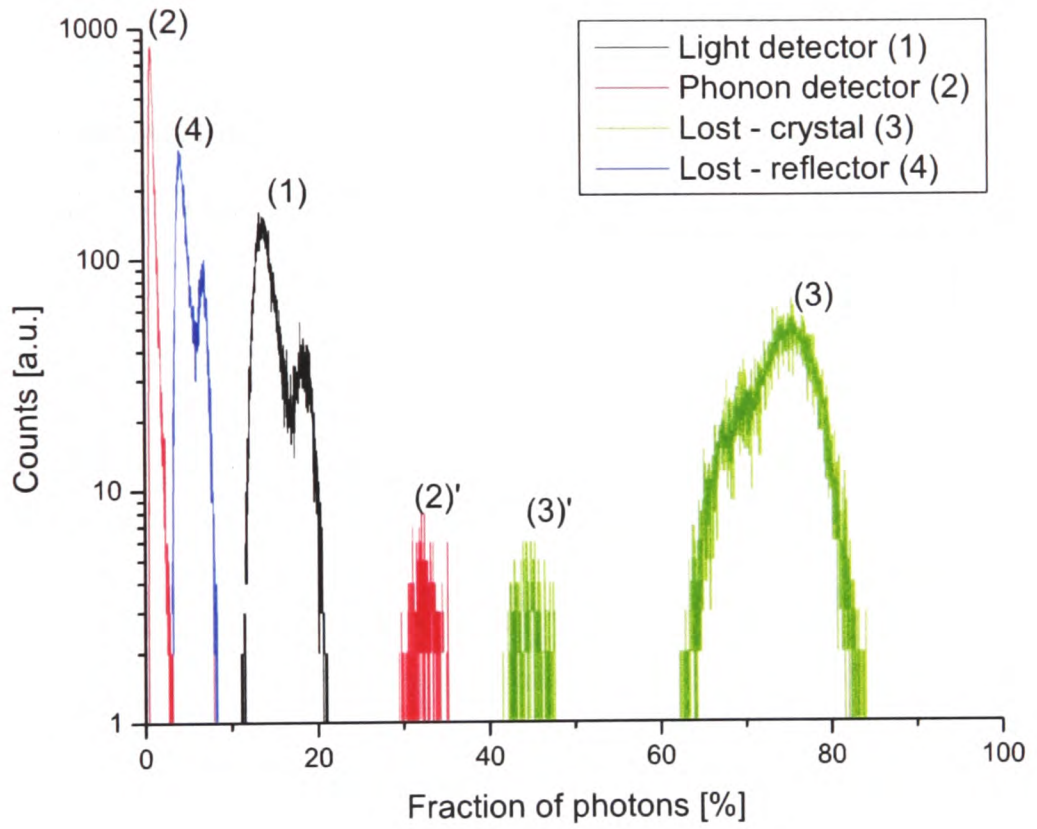

Figure 9.11: *Histogram of the fate of the photons in the CRESST setup: (1) Detected in light channel; (2) Detected in phonon channel, (2)' Produced close to phonon detector, detected in phonon channel; (3) Absorbed in the crystal, (3)' Produced close to phonon detector, absorbed in crystal; (4) Absorbed by the reflector.*

further improvement of the light collection properties, especially in order to reduce the number of photons absorbed in the crystal. This suggests that efforts could be directed toward investigating crystal growth methods for reducing α_{abs} and reducing trapping by increasing α_{scat}.

Along with the phonon collection efficiency ϵ, the re-absorption factor b is the main factor which determines the light to phonon energy deposition ratio. Using $N_0\gamma(E_{dep})$=34000ph/MeV, ν_0=2.9eV, E_{dep}=0.122keV and ϵ=70% yields a light to phonon deposited energy ratio of 2.5%. This is the first prediction of the light to phonon deposited energy made for the CRESST modules.

9.4 Conclusions

In this chapter, MC studies of the light collection properties of CRESST modules have been presented. The first result obtained was a clear explanation of the double-peak structure that was observed in low temperature CRESST runs. It was demonstrated that the double structure is due to light collection inhomogeneities within the $CaWO_4$ crystals. After studying the homogeneity of the detectors, methods of improving the light collection were examined. It is found that the orientation of the optical axis does not affect the light yield of $CaWO_4$ significantly. However, in $ZnWO_4$ like crystals, the light yield can be improved by approximately 5% if the right axis orientation is chosen. Other ways of optimising the light yield include moving out the reflector. It is also shown that a small decrease in reflectivity causes a much larger decrease in the light yield emphasising the importance of optimising the reflector properties. A proposal was made for a modified setup containing a second internal reflector. Simulations have shown that this reflector could increase the light yield by close to 20% in crystals with low scattering. Finally, the relative energy deposited in the light and phonon absorbers is evaluated at 2.5% using

the predictions of the MC.

Conclusions

Dark matter search experiments are entering an exciting new phase where their sensitivity will enable the test of many supersymmetric WIMP models. With a further narrowing of cross-section/mass phase space coming from the LHC, there is a very good perspective for the discovery of supersymmetric dark matter in the not too distant future. One of the most promising approaches for the direct detection of WIMP recoils is the cryogenic phonon-scintillation detection (CPSD) technique pioneered by CRESST. The detection of phonons preserves the high sensitivity of cryogenic calorimeters whilst the collection of scintillation light allows the active rejection of background events. The discrimination threshold of CRESST is $\sim$12keVee and is limited by the statistical broadening of the light signal. Lowering the discrimination threshold therefore requires detecting more light. This is one of the main priorities of CRESST and was the focus of the current work.

The problem of maximising the light yield of scintillators is one found across a range of physics branches as for example in medical physics. One approach is to study the spectroscopic properties of the materials to gain an understanding of the mechanisms of production of scintillation light. In the future, CPSD rare event searches will use a variety of scintillating crystals. As part of this thesis, the spectroscopic properties of $CaWO_4$ and potential CPSD materials were investigated. Potential CPSD materials include $ZnWO_4$, $CaMoO_4$, $CdMoO_4$, $MgMoO_4$, CaF_2, MgF_2 and Al_2O_3. As a result of these studies, $ZnWO_4$ is now being tested for implementation in future phases of CRESST. Except for

MgF_2, all of the crystals proved to have sufficient light yield to be considered as potential CPSD and the optimisation of the properties of $CaMoO_4$ are being actively pursued. The examination of the spectroscopic properties of the crystals led to the development and testing of the multi-photon counting technique (MPCC). The MPCC technique can be used to examine the decay time properties and luminescence intensity under particle excitation in the temperature range 0-300K. Of particular interest is the ability of the MPCC to eliminate contributions from multiple events when evaluating the decay time constants.

Another approach to increasing the light yield of crystals in CPSD modules is to optimise the light collection efficiency using a MC program. The accurate simulation of light collection is complicated by the difficulty in measuring some of the optical parameters. The intrinsic light yield, the scattering coefficient and the absorption coefficient cannot be measured directly and require alternative methods of determination. This thesis has demonstrated the importance of understanding the surface properties of HIS crystals that are to be reproduced by MC simulations. In particular, it was demonstrated that small deviations from surface planarity can lead to lensing effects which change the way light propagates at the crystal surfaces.

To determine the unknown input parameters, a MC-experiment combination was developed called the Monte-Carlo refractive index matching (MCRIM) technique. Using this method, the scattering to absorption coefficient ratio of a reference $CaWO_4$ crystal was measured as 0.93 ± 0.2. This result indicates that scattering plays a fundamental role in determining the light yield of a setup, a process often overlooked in the simulation of HIS. The MCRIM technique also resulted in the calculation of an intrinsic light yield 40% superior to that obtained using the standard comparative method. This result is particularly important in the context of simulating the light yield of setups with a similar material but with crystals of different size and geometry. In summary, the MCRIM technique has

been developed as an easy way to obtain the intrinsic light yield, the scattering coefficient and the absorption coefficient of HIS.

The parameters obtained using the MCRIM technique on $CaWO_4$ have been successfully implemented to produce simulations of CRESST modules at low temperatures. The simulated light collection inhomogeneity was used to explain the scintillation double peak structure seen in low temperature runs. The MC simulations were also used to optimise the light yield of the CRESST modules by varying the position of the reflectors. As an example, moving the side reflector to a distance of 1cm from the curved crystal side is shown to produce an increase in light yield of between 10-20%.

Starting from the spectroscopic characterisation of scintillators, this thesis has provided a comprehensive method for the optimisation of the light yield in heavy inorganic scintillators. The development of the MPCC and MCRIM techniques has facilitated the characterisation of the scintillation and optical properties of CPSD materials. Using the methods established in this work, it is possible to envisage the evaluation of the performance of HIS before they are implemented in a cryostat. Using MC simulations, efforts can be saved on R&D for future CPSD modules and the light yield can be optimised before their construction. The simulations will also allow to estimate the possible limits that can be achieved on the discrimination threshold in CRESST and future dark matter experiments such as EURECA. The techniques of characterisation and optimisation of light yield in HIS are not only a good tool for the future of dark matter, but have applications in a broad range of physics applications from medical imagery to radio-protection.

Publications

D. Wahl, V.B. Mikhailik and H. Kraus, The Monte-Carlo refractive index matching technique for simulating the light collection efficiency in heavy inorganic scintillators, International conference on inorganic scintillators and their industrial applications, SCINT 2005, Sept 19-23, http://isma.kharkov.ua/SCINT2005/

H. Kraus, V.B. Mikhailik and D. Wahl, Multiple photon counting coincidence (MPCC) technique for scintillator characterisation and its application to studies of $CaWO_4$ and $ZnWO_4$ scintillators, Nucl. Inst. Meth. A, In Print

V.B. Mikhailik, D. Wahl et al., Low-temperature spectroscopic and scintillation characterisation of Ti-doped Al_2O_3, Nucl. Inst. Meth. A, 546 (2005) 523-534

V.B. Mikhailik, D. Wahl et al., Luminescence of $CaWO_4$, $CaMoO_4$, and $ZnWO_4$ scintillating crystals under different excitations, J. App. Phys., 97 (2005) 083523

V.B. Mikhailik, D. Wahl et al., Studies of electronic excitations in $MgMoO_4$, $CaMoO_4$ and $CdMoO_4$ crystals using VUV synchrotron radiation, Phys. Stat. Sol. B, 242 (2005) R17-R19

V.B. Mikhailik, D. Wahl et al., Luminescence studies of Ti-doped Al_2O_3 using vacuum ultraviolet synchrotron radiation, App. Phys. Lett., 86 (2005) 101909

V.B. Mikhailik, D. Wahl et al., One- and two-photon excited luminescence and band gap assignment in $CaWO_4$, Phys. Rev. B, 69 (2004) 205110

V.B.Mikhailik, D. Wahl et al., Studies of the luminescence properties of Ti-doped Al_2O_3 under VUV excitation, Hasylab Annual Reports, Part I (2004) 387-388

V.B. Mikhailik, D. Wahl et al., Low-temperature luminescence characterisation of molybdate crystals, Hasylab Annual Reports, Part I (2004) 289-290

Bibliography

[1] K. Hagiwara et al. "Review of particle physics". *Phys. Rev. D*, **1** (2002) 1–974.

[2] L. Bergström. "Non-baryonic dark matter: observational evidence and detection methods". *Rep. Prog. Phys.*, **2000** (63) 793–841.

[3] C.L. Bennett et al. "First year Wilkinson microwave anisotropy probe (WMAP) observations: preliminary maps and basic results". *Astrophys. J. Suppl.*, **148** (2003) 1–27.

[4] F. Bernardeau. "The large-scale structures of the Universe". *Nucl. Phys. B Proc. Suppl.*, **87** (2000) 13–20.

[5] J.P. Ostriker & P. Steinhardt. "New light on dark matter". *Science*, **300** (2003) 1909–1913.

[6] F. Zwicky. "On the masses of nebulae and clusters of nebulae". *Astrophys. J.*, **86**, 3 (1937) 217–246.

[7] Y. Sofue & V. Rubin. "Rotation curves of spiral galaxies". *Ann. Rev. Astron. Astrophys.*, **39** (2001) 137–174.

[8] P.C.V. Kruit & R.J. Allen. "The kinematics of spiral and irregular galaxies". *Ann. Rev. Astron. Astrophys.*, **16** (1978) 103–139.

[9] C. Alcock et al. "The MACHO project: microlensing results from 5.7 years of large magellenic cloud observations". *Astrophys. J.*, **542** (2000) 281–307.

[10] I.S. Altarev et al. "New measurement of the electric dipole moment of the neutron". *Phys. Lett. B*, **276** (1992) 242–246.

[11] R.D. Peccei & H.R. Quinn. "CP conservation in the presence of pseudo-particles". *Phys. Rev. Lett.*, **38** (1977) 1439–1443.

[12] D. Kinion, I.G. Irastorza & K. van Bibber. "Searches for astrophysical and dark matter axions". *Nucl. Phys. B (Proc. Suppl.)*, **143** (2005) 417–422.

[13] P. Sikivie. "Experimental tests of the invisible axion". *Physical Review Letters*, **51** (1983) 1415–1417.

[14] M. Milgrom. "MOND - theoretical aspects". *New Astron. Rev.*, **46** (2002) 741–753.

[15] M. Milgrom. "On stability of galactic disks in the modified dynamics and the distribution of their mean surface brightness". *Astrophys. J.*, **338** (1989) 121–127.

[16] SNO Collaboration. "Direct evidence for neutrino flavor transformation from neutral-current interactions in the Sudbury Neutrino Observatory". *Phys. Rev. Lett.*, **89** (2002) 011301.

[17] KamLAND Collaboration. "First results from KamLAND: evidence for reactor antineutrino disappearance". *Phys. Rev. Lett.*, **90** (2003) 021802.

[18] S. Eidelman et al. "Review of particle physics". *Phys. Lett. B*, **592** (2004) 1+. `http://pdg.lbl.gov`

[19] G. Jungman, M. Kamionkowski & K. Griest. "Supersymmetric dark matter". *Physics Reports*, **267** (1996) 195–373.

[20] J.D. Lewin & P.F. Smith. "Review of mathematics, numerical factors, and corrections for dark matter experiments based on elastic nuclear recoil". *Astroparticle Phys.*, **6** (1996) 87.

[21] J. Ellis, A. Ferstl & K. Olive. "Exploration of elastic scattering rates for supersymmetric dark matter". *Phys. Rev. D*, **63** (2001) 065016.

[22] V.A. Bednyakov, H.V. Klapdor-Kleingrothaus & S.G. Kovalenko. "Direct detection of supersymmetric dark matter and the role of the target nuclear spin". *Phys. Rev. D*, **50** (1994) 7128–7143.

[23] L. Baudis et al. "New Limits on Dark Matter WIMP from the Heidelberg-Moscow Experiment". *Phys. Rev. D*, **59** (1999) 022001.

[24] C. Spiering. "High energy neutrino telescopes". *Nucl. Phys. B Proc. Suppl.*, **125** (2003) 1–10.

[25] L. Wai. "Searches for WIMP annihilation with GLAST". *New Astron. Rev.*, **49** (2005) 307–310.

[26] R. Bernabei et al. "Dark Matter search". *La Rivista del Nuovo Cimento*, **26** (2003) 1–73.

[27] Y. Ramachers. "Modulation analysis methods for WIMP direct detection: merits and restrictions". *Astroparticle Phys.*, **19** (2003) 419–439.

[28] H. Kraus. "Direct WIMP detection with cryogenic detectors". *Phil. Trans. R. Soc. London Ser. A*, **361** (2003) 2581–2590.

[29] CDMS Collaboration. "First results from the cryogenic dark matter search at Soudan". *Nucl Phys. B Proc. Suppl.*, **143** (2005) 429–431.

[30] V. Sanglard et al. "Final results of the EDELWEISS-I dark matter search with cryogenic heat-and-ionization Ge detectors". *Phys. Rev. D*, **71** (2005) 122002.

[31] UK Dark Matter Collaboration. "First limits on nuclear recoil events from the ZEPLIN I galactic dark matter detector". *Astroparticle Phys.*, **23** (2005) 444–462.

[32] G.J. Alner et al. "Status of the ZEPLIN II experiment". *New Astron. Rev.*, **49** (2005) 259–263.

[33] D.B. Cline et al. "An Xe detector for WIMP search". *IEEE Trans. Nuc. Sci.*, **49** (2000) 1238–1242.

[34] G. Angloher et al. "Limits on WIMP dark matter using scintillating $CaWO_4$ cryogenic detectors with active background suppression". *Astroparticle Phys.*, **23** (2005) 329–335.

[35] A. Bottino et al. "Light Neutralinos and WIMP direct searches". *Nucl. Phys. B Proc. Suppl.*, **113** (2002) 50–59.

[36] S. Henry. "The 66-channel readout for the CRESST dark-matter search". Ph.D. thesis, University of Oxford (2003).

[37] F. Pröbst, M. Frank & S. Cooper et al. "Model for cryogenic particle detectors with superconducting phase transition thermometers". *J. Low temp. Phys.*, **100** (1995) 69–104.

[38] J. Ninković. "Investigation of $CaWO_4$ Crystals for Simultaneous Phonon-Light Detection in the CRESST Dark Matter Search". Ph.D. thesis, Technische Universität München (2005).

[39] G. Angloher et al. "Limits on WIMP dark matter using sapphire cryogenic detectors". *Astroparticle Phys.*, **18** (2002) 43–55.

[40] CRESST Collaboration. "Limits on WIMP dark matter using scintillating $CaWO_4$ cryogenic detectors with active background suppression". *Astroparticle Phys.*, **23** (2005) 325–339.

[41] C. Arpesella. "Background measurements at Gran Sasso Laboratories". *Nucl. Phys. B Proc. Suppl.*, **28A** (1992) 420.

[42] H. Wulandari et al. "Neutron Flux at the Gran Sasso Underground Laboratory Revisited". *Astroparticle Phys.*, **22** (2004) 313–322.

[43] F. Petricca et al. "Light detector development for CRESST II". *Nucl. Instr. Meth. Phys. Res. A*, **520** (2004) 193–196.

[44] R. Schnee. "Current status of search for WIMP dark matter". In "INT Underground Science Workshop", (2005). `http://www.int.washington.edu/talks/WorkShops/int_05_2a`

[45] O. Martineau. "Dark matter search with a 320g ionisation/heat bolometer in the Edelweiss experiment". In "Dark Matter", (2002). `http://www.physics.ucla.edu/hep/DarkMatter/dm2002.html`

[46] Y. Ramachers. "WIMP direct detection overview". *Nucl. Phys. B Proc. Suppl.*, **118** (2003) 341–350.

[47] H. Kraus et al. "Feasibility study of a $ZnWO_4$ scintillator for exploiting materials signature in cryogenic WIMP dark matter searches". *Phys. Lett. B*, **610** (2005) 37–44.

[48] H. Kraus. "EURECA: the European Future of Cryogenic Dark Matter Searches". In "TAUP", (2005).

[49] K. Zuber. "On the physics of massive neutrinos". *Phys. Rep.*, **305** (1998) 295–364.

[50] H.V. Klapdor-Kleingrothaus, J. Hellmig & M. Hirsch. "Future perspectives of double beta decay and dark matter search - GENIUS". *J. Phys. G*, **24** (1998) 483–516.

[51] F.T. Avignone. "Strategies for next generation neutrinoless double-beta decay experiments". *Nucl. Phys. B Proc. Suppl.*, **143** (2005) 233–239.

[52] Yu.G. Zdesenko et al. "CARVEL experiment with $^{48}CaWO_4$ crystal scintillators for the double β decays tudy of ^{48}Ca". *Astroparticle Phys.*, **23** (2005) 249–263.

[53] C. Cozzini et al. "Detection of the natural alpha decay of tungsten". *Phys. Rev. C*, **70** (2004) 064606.

[54] A.A. Annenkov, M.V. Korzhik & P. Lecoq. "Lead tungstate scintillation material". *Nucl. Instr. Meth. Phys. Res. A*, **490** (2002) 30–50.

[55] CMS Collaboration. "CMS Technical Proposal". *CERN/LHCC*, **97-33**.

[56] F. X. Gentit. "Litrani: A general purpose Monte-Carlo program simulating light propagation in isotropic or anisotropic media". *Nucl. Instr. Meth. Phys. Res. A*, **486** (2002) 35–39.

[57] F. Cayouette, C. Moisan & D. Laurendeau. "DETECT2000: An improved Monte-Carlo simulator for the computer aided design of photon sensing devices". In "Proc. SPIE Photonic North", Quebec, Canada (2002).

[58] S. Agostinelli et al. "GEANT 4- a Simulation Toolkit". *Nucl. Instr. Meth. Phys. Res. A*, **506** (2003) 250–303.

[59] Carlo Fiorini. "A Monte-Carlo optical code for the study of gamma cameras based on a scintillator read out by a silicon photodetector array". *IEEE Trans. Nuc. Sci.*, **47**, 6 (2000) 1911–1917.

[60] C.D. Zerby, A. Meyer & R.B. Murray. "Intrinsic line broadening in NaI(Tl) gamma-ray spectrometers". *Nuc. Instr. Meth. Phys. Res. A*, **12** (1961) 115–123.

[61] P.Dorenbos, J.T.M Haas & C.W.E. van Eijk. "Non-proportionality in the scintillation response and the energy resolution obtainable with scintillation crystals". *IEEE Trans Nuc Sci*, **42**, 6 (1995) 2190–2202.

[62] T.D. Taulbee et al. "The measured electron response nonproportionalities of CaF_2, BGO and LSO". *IEEE Trans Nuc Sci*, **44**, 3 (1997) 489–493.

[63] M. Moszyński et al. "$CdWO_4$ crystal in gamma-ray spectroscopy". *IEEE*.

[64] G.F. Knoll & T.M. Henderson. "Light collection in scintillation detector composites for neutron detection". *IEEE Trans. Nucl. Sci.*, **35**, 1.

[65] A. Levin & C. Moisan. "A more physical approach to model the surface treatment of scintillation counters and its implementation into DETECT". *IEEE Nucl. Sci. Conf. R.*, pages 702–706.

[66] J. Bea et al. "Simulation of Light Collection in Scintillators with Rough Surfaces". *Nucl. Instr. Meth. Phys. Res. A*, **350** (1994) 184–191.

[67] C. Carrier & R. Lecomte. "Effect of geometrical modifications and crystal defects on light collection in ideal rectangular parallelepipedic BGO scintillators". *Nucl. Instr. Meth. Phys. Res. A*, **294** (1990) 355–364.

[68] C. Moisan, A. Levin & H. Laman. "Testing scintillation transport models with photoelectron yields measured under different surface finishes". *IEEE Nucl. Sci. Symp.*, **1** (1997) 824–828.

[69] A. Wirrwar et al. "Influence of crystal geometry and wall reflectivity on scintillation photon yield and energy resolution". *IEEE Nucl. Sci. Conf. R.*, **3** (1999) 1443–1445.

[70] M. Globus & B. Grinyov. "Operation characteristics of ionizing radiation detectors based on inorganic and plastic scintillators for nuclear physics and medical instrumentation". *IEEE Nucl. Sci. Conf. R.*, **1-3** (1995) 771–775.

[71] H. Tawara et al. "Monte-Carlo method for determinimg absolute scintillation-photon yields and energy resolution of scintillators for gamma rays." In "Proceedings of the Second International Workshop on EGS, KEK Proceedings 200-20", pages 152–160 (2000).

[72] Ya.A. Berdnikov et al. "Special features of light collection processes in heavy-crystal-based scintillation detectors". *Instr. and Exp. Techniques*, **44**, 4 (2001) 466–471.

[73] H. Rothfuss et al. "Monte-Carlo simulation study of LSO crystals". *IEEE Trans. Nucl. Sci.*, **3**, 51 (2004) 770–774.

[74] A.G. Wright. "A Monte-Carlo simulation of photomultiplier resolution". *IEEE Trans. Nucl. Sci.*, **34**, 1 (1987) 414–417.

[75] F. Cayouette et al. "Monte-Carlo modeling of scintillator crystal performance for stratified PET detectors with DETECT2000". *IEEE Trans. Nuc. Sci.*, **49** (2002) 624–628.

[76] F. Cayouette, Nan Zhang & C. J. Thompson. "Monte-Carlo simulation using DETECT2000 of a multilayered scintillation block and fit to experimental data". *IEEE Trans. Nuc. Sci.*, **50** (2003) 339–343.

[77] A.P. Dhanasopon et al. "Scintillation crystal design features for a miniature gamma ray camera". *IEEE Nucl. Sci. Conf. R*, pages 1967–1971.

[78] T.T. Monajemi et al. "Modeling scintillator-photodiodes as detectors for megavoltage CT". *Medical Physics*, **5**, 31 (2004) 1225–1234.

[79] R. Chipaux & F. X. Gentit. "Simulation of Light Collection in the CMS Lead Tungstate Crystals with the Program Litrani: Coating and Surface Effects". *Nucl. Instr. Meth. Phys. Res. A*, **486** (2002) 48–54.

[80] K. Ogawa & S. Maeda. "A Monte-Carlo method using octree structure in photon and electron transport". *IEEE Trans. Nucl. Sci.*, **42**, 6 (1995) 2322–2326.

[81] M.J. Berger & J.H. Hubbell. "NIST x-ray and gamma-ray attenuation coefficients and cross-sections database". *NIST Standard Reference Database 8*, page http://physics.nist.gov/PhysRefData/Xcom/Text.

[82] H. Messel & D.F. Crawford. "Electron photon shower distribution function table for lead cooper and air absorbers". Pergamon (1970).

[83] F. Arqueros & G.D. Montesinos. "A simple algorithm for the transport of gamma rays in a medium". *Am. J. Phys.*, **38**, 1.

[84] M. Moszyński et al. "Characterization of $CaWO_4$ scintillator at room and liquid nitrogen temperatures". *Nucl. Inst. Meth. Phys. Res A*, **In Print.**

[85] C. Kittel. "Introduction to solid state physics". John Wiley & Sons, 7^{th} edition edition (1996).

[86] F. Bloch. *Zeitschrift für Physik*, **52** (1928) 555.

[87] G. Blasse & B.C. Grabmaier. "Luminescent materials". Springer-Verlag (1994).

[88] R. Visser. "Energy transfer in fluoride scintillators". Ph.D. thesis, Delft University (1993).

[89] V. Denks, T. Savikhina & V. Nagirnyi. "Dependence of luminescence processes and transmission in vacuum-ultraviolet region on surface condition in CaF_2 single crystals". *App. Surf. Sci.*, **158** (2000) 301–309.

[90] G.W. Rubloff. "Far-ultraviolet reflectance spectra and the electronic structure of ionic crystals". *Phys. Rev. B*, **5**, 2 (1972) 662–684.

[91] T. Tomiki et al. "Anisotropic optical spectra of α-Al_2O_3 single crystals in the vacuum untraviolet region. I. Spectra of absorption tail and reflectivity". *J. Phys. Soc. Jap.*, **62**, 2 (1993) 573–584.

[92] M. Itoh & T. Sakurai. "Composite nature of the self-trapped exciton luminescence of $PbWO_4$". *Phys. Stat. Sol. B*, **242** (2005) R52–R54.

[93] G. Blasse & G. Bokkers. "Low-temperature decay-time measurements on the luminescence of calcium tungstate ($CaWO_4$)". *J. Sol. St. Chem.*, **49** (1983) 126.

[94] G.B. Beard, W.H. Kelly & M.L. Mallory. "Temperature Dependent Luminescence of $CaWO_4$ and $CdWO_4$". *J. App. Phys.*, **33**, 1 (1962) 144.

[95] N.F. Mott. "On the Absorption of Light by Crystals". *Proc. Roy. Soc. London A*, **167** (1938) 384.

[96] R. Keeling. "Studies of scintillators for the CRESST dark matter search". Ph.D. thesis, University of Oxford (2002).

[97] D. Curie & B. Di Bartolo. "Absorption and emission spectra, in: optical properties of ions in solids". Plenum Press (1974).

[98] H.M. Rosenberg. "The Solid State". Oxford University Press, 3rd edition edition (1995).

[99] G. Zimmerer. "Status report on luminescence investigations with synchrotron radiation at HASYLAB". *Nucl. Instr. Meth. Phys. Res. A*, **308** (1991) 178.

[100] F. Quinn et al. "The mobile luminescence end-station". *J. Synchrotron Rad.*, **10** (2003) 461–466.

[101] G. van der Laan & H.A. Padmore. "A chromatic premirror system for a double-crystal monochromator". *Nucl. Instr. Meth. Phys. Res. A*, **291** (1990) 225–227.

[102] H. Kraus, V.B. Mikhailik & D. Wahl. "Multiple photon counting coincidence (MPCC) technique for scintillator characterisation and its application to studies of $CaWO_4$ and $ZnWO_4$ scintillators". *Nucl. Instr. Meth. Phys. Res. A*, **Submitted**.

[103] L.M. Bollinger & G. E. Thomas. "Measurement of the Time Dependence of Scintillation Intensity by a Delayed-Coincidence Method". *Rev. Sci. Instr.*, **32** (1961) 1044.

[104] M. Moszyński & B. Bengtson. "Light-pulse shapes from plastic scintillators". *Nucl. Inst. Meth. in Phys. Res. A*, **142**, 3 (1977) 417–434.

[105] W. Zhaomin et al. "The influence of average photon number on the measured fluorescence decay time of scintillator". *Nucl. Instr. Meth. Phys. Res. A*, **419** (1998) 154.

[106] W.W. Moses. "A method to increase optical timing spectra measurement rates using a multi-hit TDC". *Nucl. Instr. Meth. Phys. Res. A*, **336** (1993) 253.

[107] R. Brun & F. Rademakers. "ROOT - An object oriented data analysis framework". *Nucl. Inst. Meth. Phys. Res. A*, **389** (1997) 81–86.

[108] S.S. Shapiro & M.B. Wilk. "An analysis of variance test for normality (complete samples)". *Biometrika*, **52** (1965) 591–611.

[109] M. Ochi. "Applied probability and stochastic processes in engineering and physical sciences". Wiley Interscience (1990).

[110] S. Ross. "Simulation". Academic Press, 3rd edition (2002).

[111] Kelvin & Edison. *Nature*, **59**, 1377 (1896) 170.

[112] V.B. Mikhailik, D. Wahl et al. "One- and two-photon excited luminescence and band gap assignment in $CaWO_4$". *Phys. Rev. B*, **69**, 205110.

[113] A. Lushchik, M. Kirm & C. Lushchik. "Multiplication of anion and cation electronic excitations in luminescent wide-gap ionic-crystals". *Radiat. Meas.*, **24** (1995) 365–369.

[114] M. J. Treadaway & R.C. Powell. *J. Chem. Phys.*, **61** (1974) 4003.

[115] G. Blasse. "Structure and Bonding". **42** (1980) 1.

[116] R. Grasser, A. Sharmann & K.R. Strack. "On the intrinsic nature of the blue luminescence in $CaWO_4$". *J.Lumin.*, **27** (1982) 263–272.

[117] E.V. Sokolenko et al. "Luminescence properties of oxygen disordered sheelite structure tungstates: I. Steady-state luminescence". *Inorg. Mater.*, **34** (1998) 611–615.

[118] J.A. Groenink, C. Hakfoort & G. Blasse. "Effects of annealing on calcium tungstate crystals". *Rad. Meas.*, **38**, 4-6 (2004) 403–406.

[119] R. Fletcher. *Comp. Jour.*, **13** (1970) 317.

[120] S. Teukolsky, W. Vetterling & B. Flannery. "Numerical Recipes in C". Cambridge University Press, 2^{nd} edition edition (2002).

[121] M. Gluyas, F.D. Hughes & B.W. James. "The elastic constants of calcium tungstate, 4.2-300 K". *J. Phys. D*, **6** (1973) 2025–2037.

[122] D. Christofilos, S. Ves & G.A. Kourouklis. "Pressure induced phase transitions in alkaline earth tungstates". *Phys. Stat. Sol. B*, **198** (1996) 539–544.

[123] Yu.G. Zdesenko et al. "Scintillation properties and radioactive contamination of $CaWO_4$ crystal scintillators". *Nucl. Instr. Meth. Phys. Res. A*, **538**, 657-667.

[124] P.C.F. Di Stefano et al. "Textured silicon calorimetric light detector". *J. Appl. Phys.*, **94** (2003) 6887–6891.

[125] Y.B. Abraham, N.A.W. Holzwarth & R.T. Williams. "Electronic structure and optical properties of $CdMoO_4$ and $CdWO_4$". *Phys. Rev. B*, **62** (2000) 1733–1741.

[126] V.B. Mikhailik, D. Wahl et al. "Luminescence of $CaWO_4$, $CaMoO_4$, and $ZnWO_4$ scintillating crystals under different excitations". *J. Appl. Phys.*, **97** (2005) 083523.

[127] A.E. Ovechkin et al. "Luminescence of $ZnWO_4$ and $CdWO_4$ crystals". *Phys. Stat. Sol. A*, **103** (1987) 285–290.

[128] H. Wang et al. "The line shape and zero-phonon line of the luminescence spectrum from zinc tungstate single crystals". *J. Phys.: Condens. Matter*, **6** (1994) 5373–5386.

[129] V. Babin et al. "Decay kinetics of the green emission in tungstates and molybdates". *Radiat. Meas.*, **38** (2004) 533–537.

[130] V.B. Mikhailik, D. Wahl et al. "Studies of electronic excitations in $MgMoO_4$, $CaMoO_4$ and $CdMoO_4$ crystals using VUV synchrotron radiation". *Phys. Stat. Sol. B*, **242**, 2 (2005) R17–R19.

[131] J.A. Groenink, C. Hakfoort & G. Blasse. "Luminescence of calcium molybdate". *Phys. Stat. Sol. A*, **54**, 1 (1979) 329–336.

[132] S.B. Mikhrin et al. "X-ray excited luminescence of some molybdates". *Nucl. Instr. Meth. Phys. Res. A*, **486** (2002) 295–297.

[133] H.J. Zhang et al. "Luminescence of the cadmium oxyfluoromolybdate, $CdMoO_3F_2$". *Sol. Stat. Com.*, **85**, 12 (1993) 1031–1034.

[134] A. Alessandrello et al. "Preliminary results on double beta decay of Te-130 with an array of twenty cryogenic detectors". *Physics Letters B*, **420** (1998) 109–113.

[135] T. Tsujibayashi et al. "Two-photon excitation spectra of exciton luminescence in CaF_2 obtained by using synchrotron radiation and laser". *J. Lumin.*, **87-89** (2000) 254–256.

[136] V. Denks, A Maaroos & V. Nagirnyi et al. "Excitonic processes in pure and doped CaF_2". *J. Phys. Condens. Mat.*, **11**, 15 (1999) 3115–3125.

[137] U. Caldiño G, A. Muñoz F & J. Rubio O. "Luminescence and energy transfer in CaF_2 slightly doped with europium and manganaese". *J. Phys.: Cond. Mat.*, **2** (1990) 6071–6078.

[138] U. Caldiño G. "Energy transfer in CaF_2 doped with Ce^{3+}, Eu^{2+} and Mn^{2+} ions". *J. Phys.: Cond. Mat.*, **15** (2003) 7127–7137.

[139] P.J. Alonso & R. Alcalá. "Excitation spectra and fluorescent lifetime measurements of Mn^{2+} in CaF_2 and CdF_2". *J. Lumin.*, **22** (1981) 321–333.

[140] Yu.M. Aleksandrov et al. "Luminescence of MgF_2 irradiated crystals under synchrotron excitation". *Opt Spektrosk*, **61** (1986) 888–889.

[141] N.G. Zakharov, T.I. Nikitinskaya & P.A. Rodnyi. "Properties of self-localised excitons in MgF_2". *Sov. Phys. Sol. Stat.*, **24** (1982) 709–710.

[142] M. Bravin et al. "The CRESST Dark Matter Search". *Astroparticle Phys.*, **12**, 107.

[143] V.B. Mikhailik, D. Wahl et al. "Luminescence studies of Ti-doped Al_2O_3 using vacuum ultraviolet synchrotron radiation". *App. Phys. Lett.*, **2005** (86) 101909.

[144] V.B. Mikhailik, D. Wahl et al. "Low-temperature spectroscopic and scintillation characterisation of Ti-doped Al_2O_3". *Nucl. Instr. Meth. Phys. Res. A*, **546** (2005) 523–534.

[145] G. Blasse et al. "$Ba_2WO_3F_4$, a new fluorotungstate with high luminescence efficiency". *J. Lumin.*, **29** (1984) 497–499.

[146] Z.H. Jie et al. "Luminescence of alkali oxyfluoromolybdates and oxyfluorotungstates". *Eur. J. Sol. Stat. Inor.*, **7-8** (1993) 773–787.

[147] J.P. Chaminade et al. "$Cd_2WO_3F_4$, a new fluorotungstate". *Mat. Sci. Eng. B*, **6** (1990) 5–7.

[148] E. Auffray et al. "Cross-calibration of two automatic quality control systems for the CMS ECAL crystals". *Nucl. Inst. Meth. Phys. Res A*, **523** (2004) 355–364.

[149] G.F. Bakhshieva & A.M. Morozov. *Optico-mekhanicheskaya promyshlennost (in Russian)*, **9** (1997) 31–33.

[150] W.L. Bond. "Measurement of the Refractive Indices of Several Crystals". *J. App. Phys.*, **36** (1965) 1674–1677.

[151] A.J. Criddle & C.J. Stanley. "Quantitative data file for ore minerals". Chapman & Hall, 3^{rd} edition edition (1993).

[152] V. Marinova & M. Veleva. "Refractive index measurements and transmission spectra of $Bi_2(MoO_4)_3$ single crystals". *Optical Materials*, **19** (2002) 329–333.

[153] S. Baccaro et al. "Ordinary and extraordinary complex refractive index of the lead tungstate $PbWO_4$ crystal". *Nucl. Inst. Meth*, **385** (1997) 209–214.

[154] M. Kremers & H. Meekes. "Application of the high-accuracy universal polarimeter to magnetic and absorbing crystals". *J Phys D: Appl. Phys*, **28** (1995) 1212–1224.

[155] T. Frank. "Development of scintillating calorimeters for the discrimination of nuclear recoils and fully ionising events". Ph.D. thesis, Technische Universität München (2002).

[156] Lord Rayleigh. *Philos. Mag*, **47** (1899) 375.

[157] D.J. Keast & B.E. Storey. "A possible contribution to light loss in calcium tungstate and yttrium aluminium garnet laser crystals by scattering". *J. Phys. D*, **1**, 4 (1968) 524–527.

[158] G.W. Fynn & W.J.A. Powell. "The cutting and polishing of electro-optic materials". Adam Hilger Ltd. (1979).

[159] "Rudolph AutoEL III MS Manual" (1996).

[160] O.S. Kusnir. "Effect of multiple reflections of light on the optical characteristics of crystals". *J. Opt. A: Pure Appl. Opt*, **5** (2003) 478–488.

[161] C.H. Huang et al. "Calculation of the absorption coefficients of optical materials by measuring the transmissivities and refractive indices". *Optical and Laser Tecnology*, **34** (2002) 209–211.

[162] Wolfram Research Inc. "Mathematica". *Wolfram Research Inc.*, **5.1**.

[163] M. Globus. "Calculation of spectrometrics characteristics for new scintillators". *Izmeritelnaya tehnika*, **5** (1990) 53–55.

[164] M. Globus. "Spectrometric Characteristics of Ionizing Radiation Detectors Based on BGO and CWO". *Nucl. Tracks. Radiat. Meas.*, **21**, 1 (1993) 131–133.

[165] E. Sysoeva, V. Tarasov & O. Zelenskaya. "Comparison of the methods for determination of scintillation light yield". *Nucl. Inst. Meth. Phy. Res. A*, **486** (2002) 67–73.

[166] G. Onyshchenko et al. "Comparative light yield measurements of oxide and alkali halide scintillators". *Nucl. Inst. Meth. Phy. Res. A*, **537** (2005) 394–396.

[167] L.V. Viktorov, V.M. Skorikov & V.M. Zhukov. "Inorganic scintillating materials". *Izvestiya Akademii Nauk SSSR, Neorganicheskie Materialy*, **27**, 10 (1991) 2005–2006.

[168] I. Holl, E. Lorenz & G. Margeras. "A measurement of the light yield of common inorganic scintillators". *IEEE Trans. Nuc. Sci.*, **35**, 1 (1988) 105–109.

[169] M. Globus & B. Grinyov. "Operation characteristics of ionizing radiation detectors based on inorganic and plastic scintillators for nuclear physics and medical instrumentation". *IEEE Trans. Nuc. Sci.*, **43**, 2 (1996) 1287–1294.

[170] "Hamamatsu photomultiplier tube handbook" (2005).

[171] U. Fano. "Ionization yields of radiations. II. The fluctuation of the number of ions". *Physical Review*, **72** (1947) 26–29.

[172] M. Moszyński & M. Balcerzyk. Private communication (2005).

[173] S. Baccaro et al. "Investigation of lead tungstate ($PbWO_4$) crystal properties". *Nucl. Phys. B Proc. Suppl.*, **61 3** (1997) 66–70.

[174] R. Chipaux & M. Géléloc. "Optical anisotropy effects in lead tungstate crystals". *DAPNIA/SED-1998 Preprints*, **02**.

[175] D. Davazoglou et al. "Structure and optical properties of tungsten thin films deposited by pyrolysis of $W(CO)_6$ at various temperatures". *J. Appl. Phys.*, **77** (1995) 6070–6072.

[176] The Thin Film Center. "The Essential McLeod", 8.9.55(ie) edition (2004).

[177] M.F. Weber et al. "Giant birefringent optics in multilayer polymer mirrors". *Science*, **287** (2000) 2451–2456.

[178] J. Ninković et al. "$CaWO_4$ crystals as scintillators for cryogenic dark matter search". *Nucl. Instr. Meth. Phys. Res. A*, **537** (2005) 339–343.

[179] K. Johnson. "Achieving the theoretical maximum light yield in scintillating fibers through non-uniform doping". *Nucl. Instr. Meth. Phys. Res. A*, **344** (1994) 432–434.

[180] C.M. Hawkes et al. "Decay time and light yield measurements for plastic scintillating fibers". *Nucl. Instr. Meth. Phys. Res. A*, **292** (1990) 329–336.

[181] C.J. Spengler & S. O'Hara. "Zinc tungstate - some optical properties". *Applied Optics*, **3**, 9 (1964) 1084–1085.

[182] M. Sisti. "CRESST - a Cryogenic Experiment for Dark Matter Searches". Ph.D. thesis, Technische Universität München (1999).